

9/8/83

Indian J Pure & Appl Phys, Vol 21 No 4 pp 197-260

April 1983

CODEN: IJOPAU ISSN: 0019-5596

21(4) 197-260 (1983)

INDIAN JOURNAL OF PURE & APPLIED PHYSICS



Published by
PUBLICATIONS & INFORMATION DIRECTORATE, CSIR
NEW DELHI

in association with
THE INDIAN NATIONAL SCIENCE ACADEMY, NEW DELHI



SHRAMA EVA JAYATE

Leadership, discipline and hard work made the 9th Asian Games a dazzling success which brought world-wide tributes to India's capacity for organisation and rapid execution of ambitious projects.

The stadia were built in record time. Colour television brought the games live into millions of homes all over the country and abroad. Computers, electronic exchanges, micro-wave and satellite links were smoothly and efficiently utilised in a mammoth network of services.

Keep the Torch Burning



Let us extend the Asiad spirit to the larger arena of national endeavour.

Our economy is on the move. It is in our hands to maintain the improvement to lighten the burdens of our millions. This endeavour is for each one of us.

**LET US ALL JOIN HANDS
TO BUILD A STRONG NATION**

Indian Journal of Pure & Applied Physics

EDITORIAL BOARD

Prof. D Basu Indian Association for the Cultivation of Science Calcutta	Prof. Probir Roy Tata Institute of Fundamental Research Bombay
Prof. B Buti Physical Research Laboratory Ahmedabad	Prof. E S Raja Gopal Indian Institute of Science Bangalore
Prof. S C Dutta Roy Indian Institute of Technology New Delhi	Prof. G Rajasekaran Madras University Madras
Dr R Hradaynath Instruments Research & Development Establishment Dehra Dun	Dr A P B Sinha National Chemical Laboratory Pune
Prof. D Premaswarup Nagarjuna University Nagarjuna Nagar	Prof. C V Vishveshwara Raman Research Institute Bangalore
Prof. A N Mitra Indian National Science Academy New Delhi/University of Delhi Delhi	Prof. M S Sodha Indian National Science Academy New Delhi/Indian Institute of Technology New Delhi

Shri Y R Chadha, *Ex-officio* Secretary & Chief Editor

EDITORIAL STAFF

Editors

D S Sastry, K S Rangarajan & R P Goel

Assistant Editors

G N Sarma, J B Dhawan & Tarun Banerjee

Scientific Assistant

(Mrs) Poonam Bhatt

Published by the Publications & Information Directorate, CSIR, Hillside Road, New Delhi 110012

Chief Editor: Y R Chadha

The Indian Journal of Pure & Applied Physics is issued monthly. The Directorate assumes no responsibility for the statements and opinions advanced by contributors. The editorial staff in its work of examining papers received for publication is assisted, in an honorary capacity, by a large number of distinguished scientists, working in various parts of India.

Communications regarding contributions for publication in the journal should be addressed to the Editor, Indian Journal of Pure & Applied Physics, Publications & Information Directorate, Hillside Road, New Delhi 110012.

Correspondence regarding subscriptions and advertisements should be addressed to the Sales & Distribution Officer, Publications & Information Directorate, New Delhi 110012.

Annual Subscription

Rs. 120.00 £20.00 \$45.00

Single Copy

Rs. 12.00 £2.00 \$4.50

50% Discount is admissible to research workers and students and 25% discount to non-research individuals, on annual subscription. Payments in respect of subscriptions and advertisements may be sent by cheque, bank draft, money order or postal order marked payable *only* to **Publications & Information Directorate, New Delhi 110012**. Claims for missing numbers of the journal will be allowed only if received within 3 months of the date of issue of the journal plus the time normally required for postal delivery of the journal and the claim.

CONTENTS

Dielectric Relaxation Studies of Chloro-Substituted Phenoxyacetic Acids in <i>p</i> -Dioxane Solutions	249
S C Srivastava* & M S Sinha														
Design & Fabrication of a 250 l Liquid Nitrogen Storage Vessel	251
M M Krishna & R G Sharma*														
Preamplifiers for Charged-Particle Detectors in High Resolution Spectroscopy	253
M B Chatterjee & R Bhattacharya*														
Electron-Electron Interaction in X-ray Emission Spectra of Rare-Earth Elements & Their Oxides	256
K S Srivastava*, A K Srivastava, Kirti Sinha, H Husain & Shiv Singh														
Electronic & Vibrational Spectra of 2,5-Dimethyl Pyrazine	258
S L Srivastava, Rohitashava* & A N Pandey														

The author to whom all correspondence is to be addressed is indicated by the () mark.

Structural, Electrical and Optical Properties of Tin-Indium Oxide Films Prepared by Spray Pyrolysis†

H S SONI*, S D SATHAYE & A P B SINHA

National Chemical Laboratory, Pune 411 008

Received 1 July 1982; revised received 24 September 1982

Thin films of Sn-In oxides were prepared on glass substrates by pyrolytic decomposition of alcoholic solutions containing anhydrous SnCl_4 and $\text{InCl}_3 \cdot 3\text{H}_2\text{O}$ in various proportions. The oxide films obtained from solutions within the range, $100 > [\text{SnCl}_4] > 73 \text{ mol\%}$, were isomorphous with the SnO_2 structure, whereas those from solutions in the range, $66 > [\text{SnCl}_4] > 56 \text{ mol\%}$, were non-crystalline (The term non-crystalline was designated to those films which did not show sharp X-ray peaks). Films with lower tin content had the In_2O_3 structure. Low resistivity films ($\rho = 10^{-2} \cdot 10^{-3} \text{ ohm-cm}$) were obtained from the starting mixtures: (a) $100 > [\text{SnCl}_4] > 99.4$, and (b) $56 > [\text{SnCl}_4] > 18 \text{ mol\%}$. These films were *n*-type. The results of the variations in the optical band gap with composition have been correlated with the structural and conductivity results.

1 Introduction

Crystallographic properties of SnO_2 layers have been studied by various workers¹⁻⁴. Structural studies on pure indium oxide as well as on a limited range of indium-tin oxide (ITO), i.e. $\text{In}_2\text{O}_3\text{-SnO}_2$, films have also been reported⁵⁻¹¹, but only a few studies have covered the entire range of $\text{In}_2\text{O}_3\text{-SnO}_2$ system^{12,13}. The conductivity of SnO_2 films has also been studied widely¹⁴⁻²⁵ and various methods for getting these films with better electrical and optical properties have been evolved to meet the requirements in connection with various applications, such as transparent electrode, solar energy conversion and display devices²⁶⁻²⁸. ITO films have been developed with resistivity as low as 10^{-4} ohm-cm and with transparency higher than 90 per cent²⁹⁻³¹. All these papers mainly describe the techniques for getting coatings with higher conductivity and higher transparency although some measurements on pure films have also been carried out. However, a systematic study of the conductivity, structure and optical absorption characteristics of films from the entire range of $\text{SnO}_2\text{-In}_2\text{O}_3$ composition prepared by the spray-technique has been lacking, and the present study attempts to fill that gap.

2 Experimental Techniques

Films of SnO_2 , In_2O_3 and their binary systems were prepared by the pyrolytic decomposition of appropriate mixtures of stannic chloride (fuming anhydrous SnCl_4) and indium trichloride ($\text{InCl}_3 \cdot 3\text{H}_2\text{O}$) in a specially designed furnace. This furnace was made by winding 20 gauge Kanthal wire on a 4 in wide

and 8 in long quartz tube with a suitable outer cover. The whole assembly was placed vertically over a 6 in thick layer of refractory bricks. A 4 in long fire-brick, which could just pass through the quartz tube, was placed in the furnace tube. The advantage of the introduction of this brick piece is that it helps in maintaining the temperature constant during the spray blast because of its large thermal inertia. A chromel-alumel thermocouple was used to measure the temperature. The substrates used were silicate glass slides, pellets of sodium chloride and alumina plates. A conventional-type, all-glass atomizer was used to blow the solution onto the substrates maintained at the required temperature ($410 \pm 10^\circ\text{C}$ or $580 \pm 10^\circ\text{C}$). A distance of 25 cm was maintained between the sprayer and the substrates. Each spraying period of 2-3 sec was followed by a waiting period of 2 min to prevent any excessive cooling of the substrates. By taking various mole percentages of SnCl_4 and InCl_3 in ethyl alcohol, films of various Sn:In oxide compositions were prepared. It was presumed that the ratio of the two metals in the oxide films was practically identical to that in the starting solution¹². Thickness measurements for the films were carried out using Tolansky's method of multiple reflection. The film-thickness obtained was in the range 600-800 Å.

Phase identification was carried out by X-ray powder diffraction using a Philips X-ray diffractometer.

Scanning electron microscopy (SEM) and the electron probe microanalysis were carried out for a few samples using a Cambridge SEM instrument, model Stereo-scan-150.

From the measurements of the current-voltage characteristics for a number of samples, it was established that vacuum evaporated silver and air

†NCL Communication No.3051

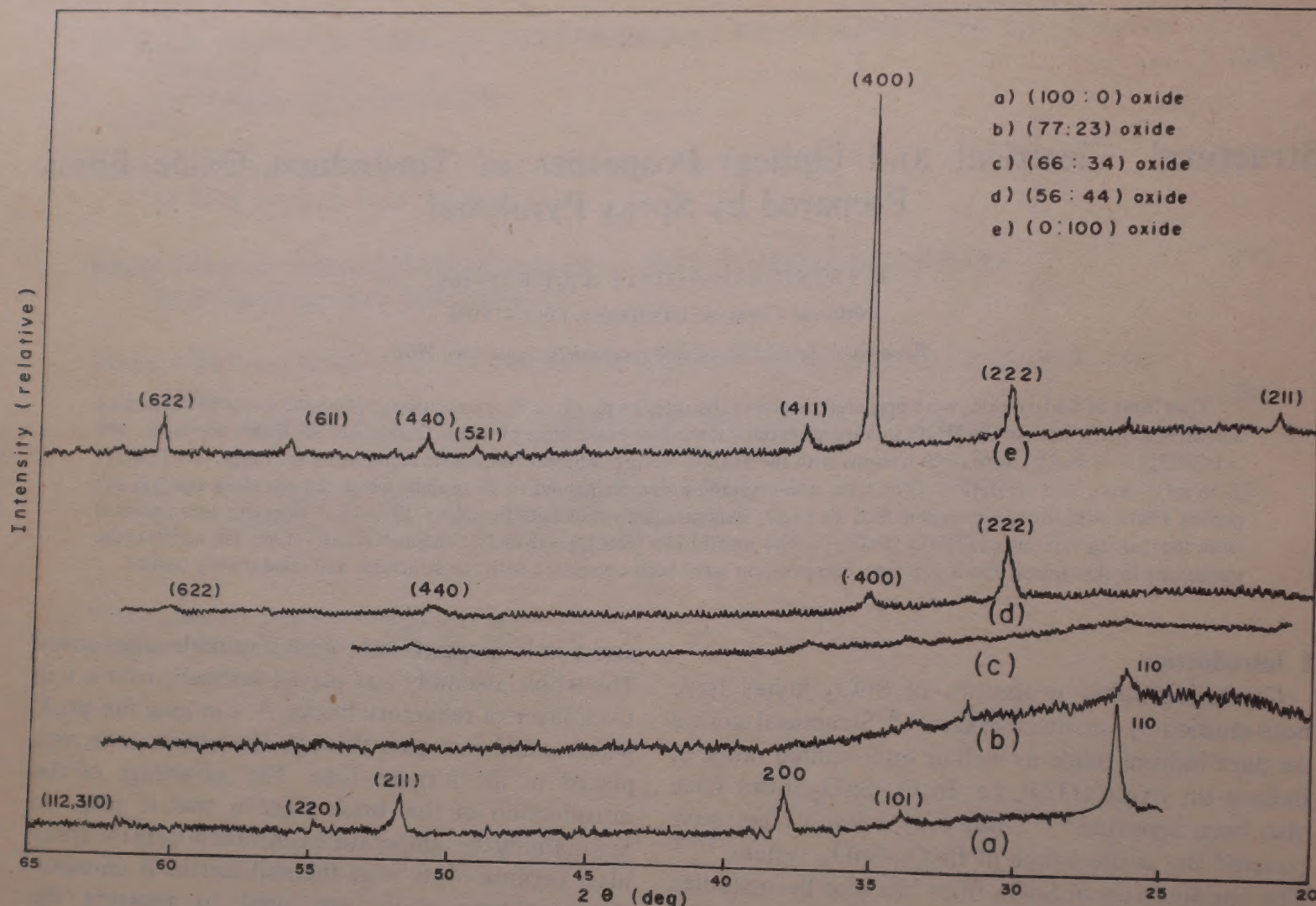


Fig. 1—X-ray diffraction patterns for the Sn:In films of various compositions deposited on glass substrate at 410°C

drying silver paste formed ohmic contacts with the films. Conductivity measurements were carried out using the four point probe technique for samples having resistivities lower than 10^3 ohm-cm. When resistivities were above 10^3 ohm-cm, the two-probe technique was used. All the measurements were carried out as a function of temperature under a continuous vacuum of the order of 10^{-4} Torr in an all-metal cryostat.

In order to evaluate the type of optical transition, the optical absorption spectrum of the films was scanned in the range 200-700 nm on a Specord UV-Vis Spectrometer made by Carl-Zeiss, Jena, and the absorption coefficient α at different photon energies ($h\nu$) was calculated. The value of optical band gap was obtained by plotting α^2 and $(\alpha h\nu)^2$ versus the photon energy. The intercept of the straight line on photon energy axis then determined the optical band gap.

3 Results and Discussion

3.1 Structural Properties

It is observed that the structure of the film is a function of the composition of the spray mixture, nature of the

substrate and the temperature of deposition. Table 1 summarizes the film-structures obtained from different mixtures. The films were deposited on glass substrate at $410 \pm 10^\circ\text{C}$.

The salient features of the results are:

i) For (100:0) oxide*, the observed X-ray peaks are sharp and intense. These peaks broaden with increasing indium concentration in the films. This indicates that the size of the crystallites decreases with the increase in the indium concentration in the films. Ultimately the crystallite size has decreased to such an extent that films of (66:34) oxide have become non-crystalline (Fig. 1; a,b,c).

ii) Although the degree of crystallization decreases with indium addition, no reflections for In_2O_3 are detected up to (77:23) oxide. (Fig. 1; a,b)

iii) From (56:44) to (0:100) oxide, the films have the bixbyite-type In_2O_3 structure (Fig. 1; d,e).

iv) SEM results indicate that the surface of the undoped SnO_2 is very smooth without any grain

*All compositions have been designated by giving the mole percentages in the starting mixtures, the first figure denoting the mole % of SnCl_4 and the second that of InCl_3 .

Table 1—Structure of Films Deposited on Glass at $410 \pm 10^\circ\text{C}$

Starting composition in the alcoholic mixture mol % $\text{SnCl}_4 : \text{InCl}_3$	Structure of the film
100:0	SnO_2
89:11	SnO_2
77:23	SnO_2
66:34	Non-crystalline
66:34 heat treatment at 580°C for 8 hr	Non-crystalline
56:44	In_2O_3
46:54	In_2O_3
36:64	In_2O_3
18:82	In_2O_3
0:100	In_2O_3

boundaries (Fig. 2a). For the films of (89:11) oxide the textured grains are formed having particle size of about $2\text{--}4\ \mu\text{m}$ (Fig. 2b). The particle size is observed to decrease with increasing indium concentration along with the decrease in the crystal size as mentioned above. The particle size for (66:34) oxide film, which does not show sharp X-ray diffraction peaks, is seen to be of the order of $0.2\text{--}1.0\ \mu\text{m}$ (Fig. 2c). On the whole, each of these films has spherically-shaped particles on the surface. The composition as observed by electron probe microanalysis is qualitatively the same over all the grains within the limits of the resolution ($70\ \text{\AA}$) of our SEM unit but these results do not totally preclude phase segregation.

As no X-ray line corresponding to In_2O_3 is observed in the Sn:In oxide films up to 77:23 composition, it is possible that in this range we have single-phase films. However, a possibility that a separate phase of In_2O_3 is formed which is amorphous, and hence not detected by X-ray diffraction, cannot be ruled out.

It is seen that increasing concentration of indium progressively reduces the particle size and inhibits the crystal grain growth and ultimately renders the films of (66:34) oxide non-crystalline. Such an observation of reduced grain size for SnO_2 films was reported by Tohda *et al.*³² when Eu concentration in the film was increased.

Carroll and Slack³³ reported that SnO_2 films were amorphous when they contained 20 mol % of Sb. This was attributed to the glass forming nature of antimony. It was further found that the films became crystalline on heating at temperatures above 580°C . Contrary to this result, crystal growth did not take place for our (66:34) oxide film on baking up to 580°C for 8 hr. Crystal growth has been inhibited possibly because SnO_2 forms strong bonds of the type > (Si-O-

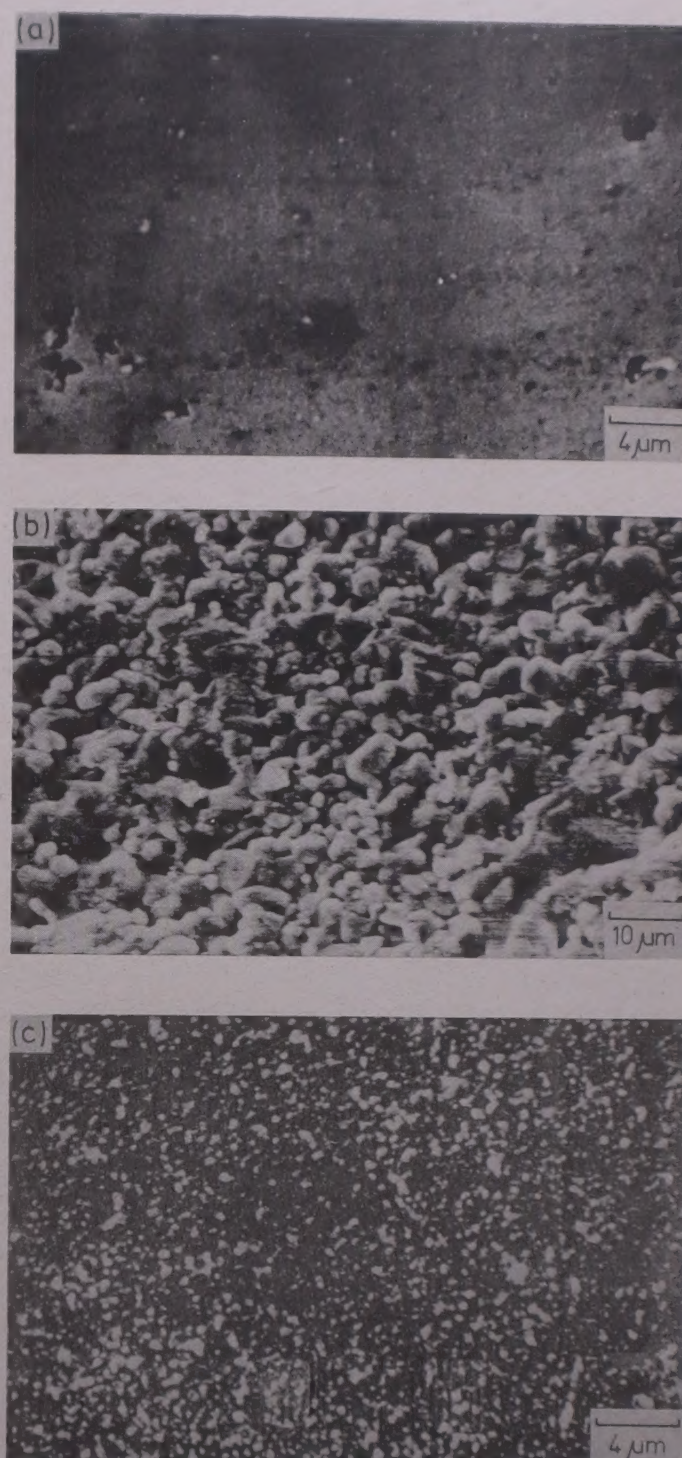


Fig. 2—Scanning electron micrographs for the Sn:In films of various compositions deposited on glass substrate at $410^\circ\text{C} \pm 10^\circ\text{C}$ [(a), (100:0) oxide; (b), (89:11) oxide; and (c), (66:34) oxide]

$\text{SN)} \leftarrow (\text{Ref.34})$ with glass and the mobility of the nuclei is expected to be low.

Since (66:34) oxide film is at the boundary of the stable SnO_2 cassiterite phase in the phase diagram, a detailed study was carried out for films of this composition and for some other film compositions by depositing these films on glass, alumina and sodium chloride substrates at 410 and $580 \pm 10^\circ\text{C}$. The results obtained are given in Table 2.

It may be seen that (66:34) oxide films are non-crystalline when deposited on amorphous substrate

Table 2—Structures of Various Sn:In Oxide Films Deposited at 410°C and 580°C on Glass, Alumina and Sodium Chloride Substrates

Starting composition	Substrate					
	Glass slides		Alumina plates		Sodium chloride pellets	
Sn:In	410°C	580°C	410°C	580°C	410°C	580°C
66:34	NC	I + S	I	I + S	I	NC
56:44	I	I + S	I	I + S	I	NC
46:54	I	I				

Abbreviations: NC, non-crystalline; I, In_2O_3 phase; S, SnO_2 phase; and I + S, ($\text{In}_2\text{O}_3 + \text{SnO}_2$) phases

(glass) at 410°C. If the films from the same composition are deposited on crystalline alumina and sodium chloride substrate at the same temperature then the films formed are crystalline and isomorphous with the bixbyite-type In_2O_3 structure (Table 2).

In order to check whether SnO_2 is present as solid solution in the bixbyite phase or as a separate non-crystalline phase, the deposition was carried out for this composition at 580°C and it is observed that two separate phases, In_2O_3 and SnO_2 appeared in the crystalline form on Al_2O_3 substrate (Table 2). It is also seen from Table 2 that the same results are obtained on amorphous glass. Thus these films are essentially mixtures of two phases, both non-crystalline, when deposited at 410°C on amorphous substrate like glass; one crystalline (In_2O_3) and one non-crystalline (SnO_2) when deposited at 410°C on crystalline Al_2O_3 and sodium chloride substrates; and both crystalline when deposited at 580°C on either crystalline (Al_2O_3) or amorphous (glass) substrate.

SEM pictures show that the particle size which was 0.2-1.0 μm for the non-crystalline films (Fig. 2c) increases to about 0.3-2 μm when the films of the same composition are deposited on a crystalline substrate.

Fig. 3a is for the film deposited on Al_2O_3 substrate and Fig. 3b shows the picture of the film deposited on NaCl substrate. The bigger particles are due to substrate. In the (66:34) oxide film deposited on glass at 580°C, which consists of two crystalline phases, namely, the SnO_2 and In_2O_3 , two types of particles are seen (Fig. 3c).

In the case of the films of (56:44) oxide, lower temperature of deposition (410°C) produces films with crystalline In_2O_3 on crystalline substrates (Al_2O_3 , NaCl) as well as on amorphous glass substrates. On depositing these films at 580°C on glass and alumina plates, both the phases (In_2O_3 and SnO_2) appear as crystalline. These results show that once the concentration of InCl_3 increases beyond 44 mol %, the

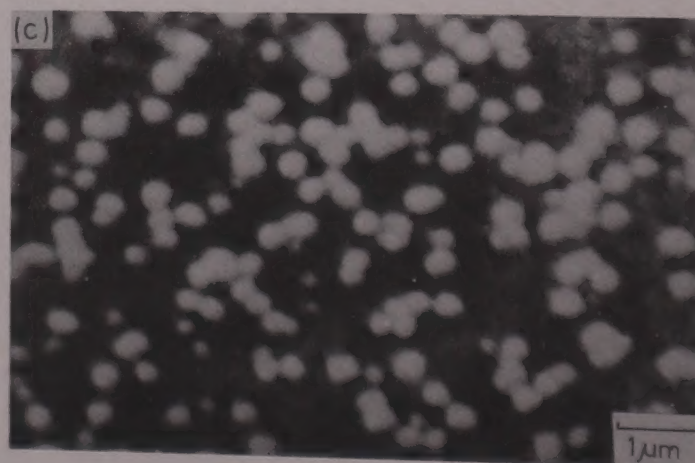
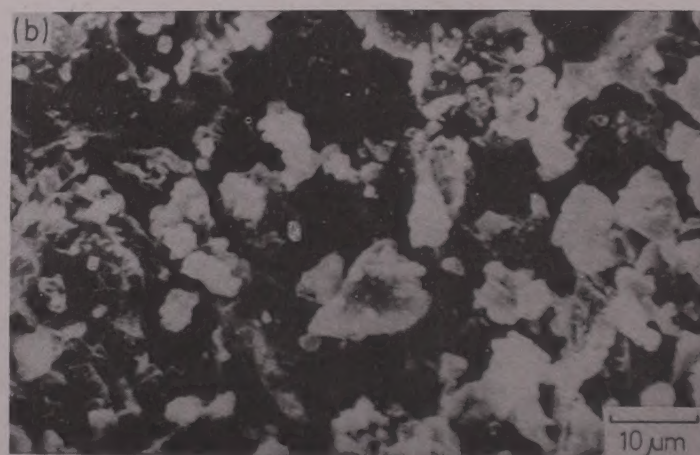
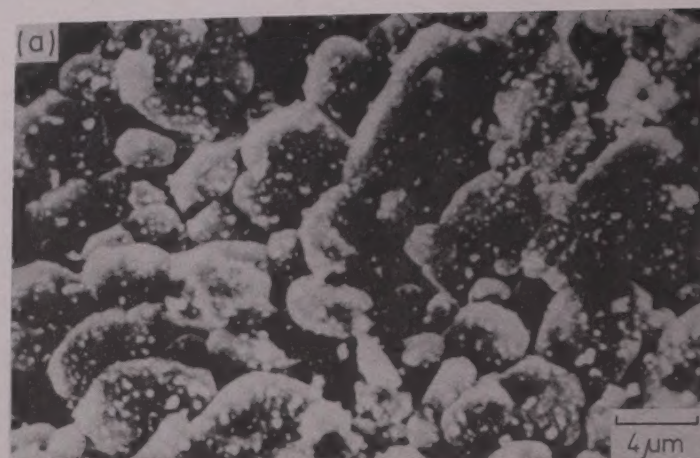


Fig. 3—Scanning electron micrographs for Sn:In (66:34) oxide films [(a), on Al_2O_3 plate (deposited at 410 °C); (b), on NaCl pellet (deposited at 410 °C); and (c), on glass substrate (deposited at 580 °C)]

substrate need not be crystalline to get a crystalline deposit. In_2O_3 can be crystallized even on amorphous substrate at 410°C. However, SnO_2 still remains in the non-crystalline form which crystallizes only by depositing the films at higher temperatures (580 °C).

When the In content in the films is increased further, e.g. (46:54) oxide, a separate crystalline phase of SnO_2 does not appear even for deposition at 580 °C. However, the crystalline In_2O_3 structure is seen at both the temperatures of the deposition. This possibly

indicates that these films are single-phase solid solution where SnO_2 goes into the In_2O_3 structure.

It is interesting to note that non-crystalline films resulted when the deposition was carried out at 580°C for (66:34) oxide and (56:44) oxide on crystalline sodium chloride pellets (Table 2). Tigane³⁵ reported that sodium and potassium ions of the glasses react chemically with the SnO_2 layers and affect the structure. Diffusion of alkali ions in the films was reported by Kane *et al.*³⁶ and Mizuhashi³⁷. In the present case, the substrate material itself is sodium chloride and deposition at higher temperatures favours the highly mobile sodium ions to diffuse through the films and affect the structure in presence of moisture.

3.2 Electrical Properties

All resistivity (ρ) measurements were carried out for the films which were deposited at 410°C . The variation of resistivity with composition at room temperature is shown in Fig. 4.

A sharp increase in resistivity from 10^{-3} ohm-cm to 10^5 ohm-cm is observed on going from (100:0) to (99.4:0.6) oxide, followed by a slower increase up to (94:6) oxide composition. Resistivity then decreases up to (56:44) oxide composition. There is then a region of nearly constant resistivity up to (18:82) oxide films. Finally resistivity rises and is of the order of 10 ohm-cm for pure In_2O_3 films.

Pure SnO_2 films have a resistivity of 10^{-3} ohm-cm which is mainly due to the oxygen deficiency since these films are not doped intentionally. The sharp increase in the resistivity with an addition of 0.6 mol % of indium is attributed to the fact that In^{3+} is substituting Sn^{4+} in the covalently-bonded SnO_2 structure and thereby reducing the free electron concentration. Further addition of indium traps more and more electrons and increases the resistivity which is observed up to (94:6) oxide films.

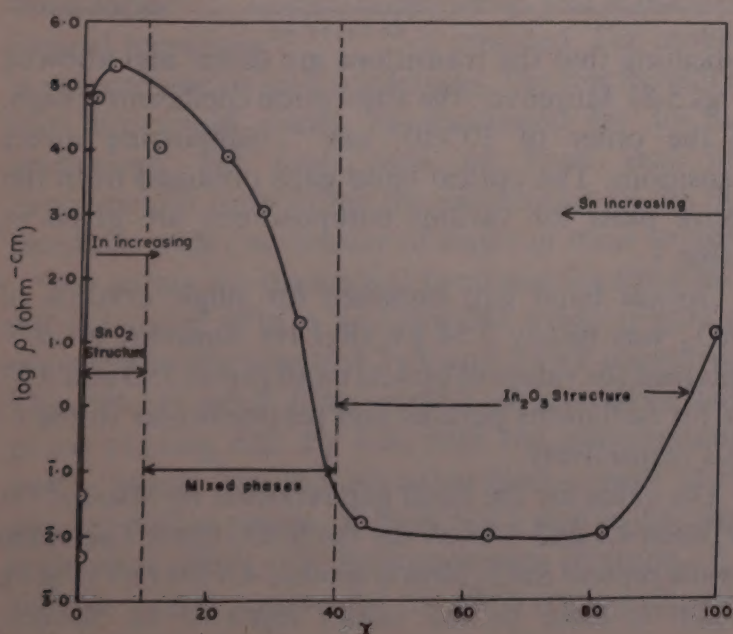


Fig. 4—Log ρ as a function of $[\text{Sn}_{(100-x)}:\text{In}_x]$ oxide composition

However, on increasing the indium concentration still further, the resistivity starts falling and this cannot be explained by the fact that In^{3+} is acting as an acceptor ion. As observed earlier that the films from (100:0) oxide to (77:23) oxide are isomorphous with the SnO_2 phase, excess indium which cannot substitute Sn^{4+} may be forming a separate In_2O_3 phase which is non-crystalline. This non-crystalline In_2O_3 is probably contributing to the conductivity and a fall in resistivity is observed for these compositions.

The resistivity then continues to decrease. The film compositions in this range are identified to be the mixture containing SnO_2 and In_2O_3 (both non-crystalline) and none of these phases crystallizes out on heating the films at 580°C for 8 hr; that means the crystallite size is too small to form the crystalline pattern (with the available thermal energy) which X-rays can detect. Such small crystallites seem to have good contact amongst themselves and low resistivity is attributed to this good contact of the crystallites. Similar interpretation has been given by Mizuhashi³⁸ for the films with lower degree of crystallinity and having low resistivity when formed at lower substrate temperature.

The films in the range (56:44) to (0:100) oxide are isomorphous with In_2O_3 phase and the conductivity behaviour for these films can be explained by considering these films to be In_2O_3 with Sn as an impurity.

The present method of pyrolytic decomposition of InCl_3 to form In_2O_3 suggests that the resulting In_2O_3 film is non-stoichiometric, having oxygen deficiency. The degree of oxygen deficiency depends on the temperature of deposition, the atmosphere in which the film is formed and the post-deposition treatment to the film. Our freshly prepared samples of In_2O_3 were formed under atmospheric conditions where a large number of oxygen deficiencies are unlikely to get formed. The film resistivity obtained was therefore high, nearly 10 ohm-cm, which on post-deposition annealing in vacuum fell to 10^{-2} to 10^{-3} ohm-cm. When the films of In_2O_3 were incorporated with 18 mol % Sn, a fall in resistivity was observed. Since the films of these compositions were not heat-treated in vacuum, the lowering of the resistivity or creation of donors has its origin in a source other than oxygen deficiency created by vacuum annealing.

It is reported in literature that addition of tin up to 4-6 wt % produces ITO films with resistivities as low as 10^{-4} ohm-cm (Ref.39), and it is shown that Sn^{4+} which replaces In^{3+} is responsible for generating the carriers. Fan and Bachner⁴⁰ observed that the lattice parameters for In_2O_3 films increase with tin incorporation and interpreted that In^{3+} ions are not replaced by Sn^{4+} ions which are smaller and would

contract the lattice. The observed expansion is consistent with the replacement of In^{3+} ions by large Sn^{2+} ions and also with the incorporation of Sn ions in the interstitial positions which are responsible for the source of carriers. The lattice constant for the present In_2O_3 films is approximately 10.05 Å; with 18 mol % Sn, the lattice parameter increases to 10.14 Å. Thus the present results are similar to those observed by Fan and Bachner⁴⁰, and hence are interpreted on similar grounds. However, with 18 mol % tin, the resistivity of In_2O_3 films obtained is 10^{-3} ohm-cm, which is higher than that obtained in film with lower tin content. This could be due to the fact that a large amount of tin might be causing disorders in the In_2O_3 lattice and is not so effective in generating carriers. However, films with 18 mol % tin show a degenerate-type behaviour as the resistivity, Hall mobility and the carrier concentration remain nearly the same over the temperature range 87-300 K. Further addition of tin (more than 18 mol %) has no effect in changing the resistivity. This is represented by the flat portion in the curve and this could be due to the compensation of carriers generated by interstitial Sn by substituted Sn^{2+} ions.

3.3 Optical Absorption

Plots of α^2 and $(\alpha h\nu)^2$ versus photon energy ($h\nu$) for films under study give fairly good straight lines,

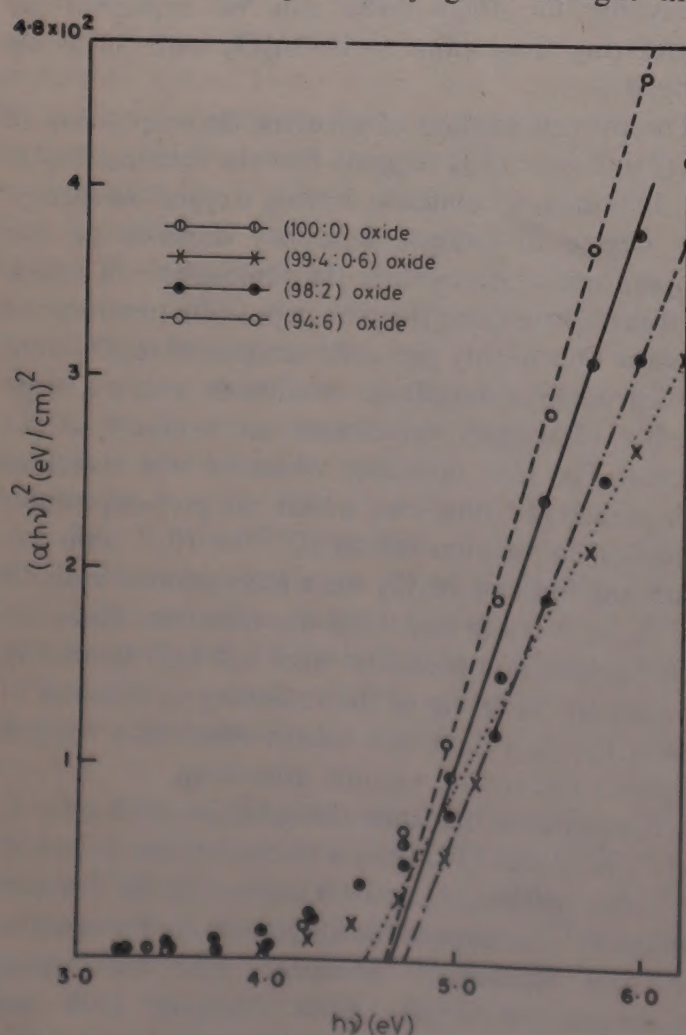


Fig. 5—Variation of $(\alpha h\nu)^2$ with photon energy ($h\nu$) for various Sn:In compositions

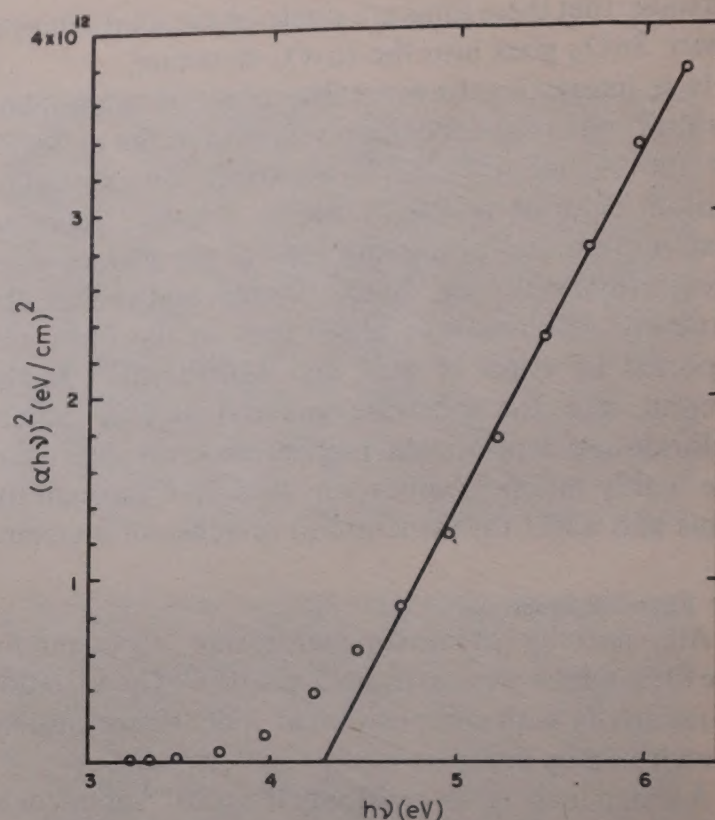


Fig. 6—Variation of $(\alpha h\nu)^2$ with photon energy ($h\nu$) for Sn:In (89:11) oxide

Table 3—Optical Band Gap of Various Compositions of Sn:In Oxide Films

Composition		Optical band gap (in eV) from		Structure
		α^2 vs $h\nu$	$(\alpha h\nu)^2$ vs $h\nu$	
Sn:In oxide				
100	0	4.5	4.64	SnO_2
99.4	0.6	—	4.46	SnO_2
98	2	—	4.74	SnO_2
94	6	—	4.60	SnO_2
89	11	—	4.3	SnO_2
66	34	3.8	—	Non-crystalline
36	64	3.7	—	In_2O_3
0	100	—	3.5	In_2O_3

indicating that the transitions are direct and allowed (Figs 5-8). Moreover, the absorption coefficient is high, of the order of 10^4 - 10^5 cm^{-1} , supporting direct transitions. The optical band gaps obtained from the above plots for various compositions are given in Table 3.

Optical band gap obtained for single crystals of SnO_2 was nearly 3.54 eV (Ref.41). Summitt *et al.*⁴² obtained the values of optical band gap as 3.93 and 3.57 eV for radiations parallel and perpendicular to the c -axis respectively.

The value for the band gap reported by Spence⁴³ is between 4.1 and 4.45 eV for the SnO_2 films. The value for the present SnO_2 films is around 4.6 ± 0.1 eV (Fig.5), which is close to the values reported by Spence. However, this value is higher than those obtained for

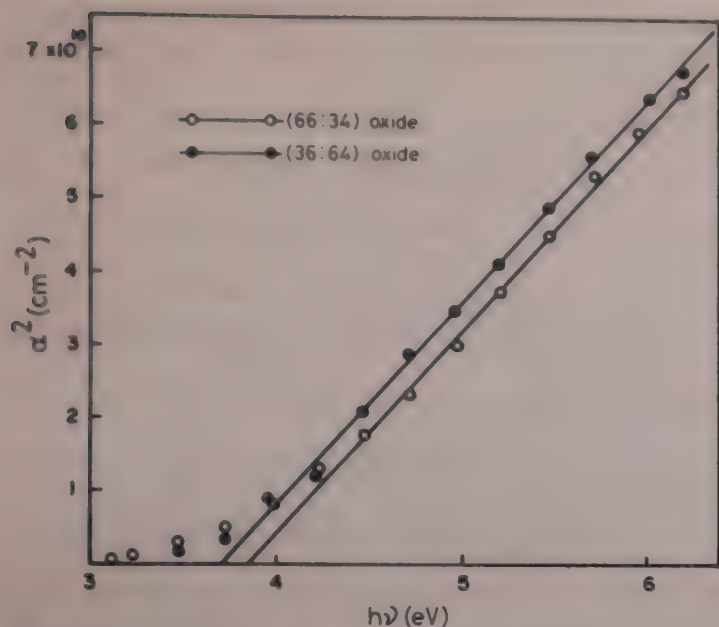


Fig. 7—Variation of α^2 with photon energy ($h\nu$) for various Sn:In compositions

the single crystals. Spence also observed that for any pair of SnO_2 films from the same deposition run, the absorption edge for the low resistivity film was about 0.1 eV higher than that for the high resistivity films. Arai⁴⁴ also observed similar effects. This was explained by assuming that the allowed states near the bottom of the conduction band were occupied and that the allowed transitions from the valence band would have correspondingly higher energies than the forbidden gap.

On adding In to SnO_2 , the resistivity of the films increases by about seven orders of magnitude even though the band gap for these films remains the same [compositions (99.4:0.6), (98:2) and (94:6) oxides] (Fig.5). These results cannot be explained on lines suggested earlier. Mobility in our films is relatively low, of the order of $3\text{--}15 \text{ cm}^2 \text{ V}^{-1} \text{ sec}^{-1}$. All these results contradict the existence of deep bands. However, for the films of SnO_2 and In_2O_3 , scattering due to grain boundaries^{45,46}, neutral impurities as well as due to the ionized impurities^{16,31,47,48} is reported. The mobility is reduced due to such scatterings. The low mobility of our film could partly be accounted for by such scatterings; but even then we have very little experimental support for the assumption of the deep parabola with low density of states in these samples.

The values for the optical band gap for the films of (89:11) oxide (Fig.6) and (66:34) oxide (Fig.7) are observed to decrease to 4.3 eV and 3.8 eV respectively. The (89:11) oxide films consist of crystalline SnO_2 phase existing side by side with the non-crystalline In_2O_3 phase. The (66:34) oxide films consist of two non-crystalline phases, namely, SnO_2 and In_2O_3 . Since both these films are heterogeneous mixtures, it is difficult to give reasons for the observed values of the optical band gap.

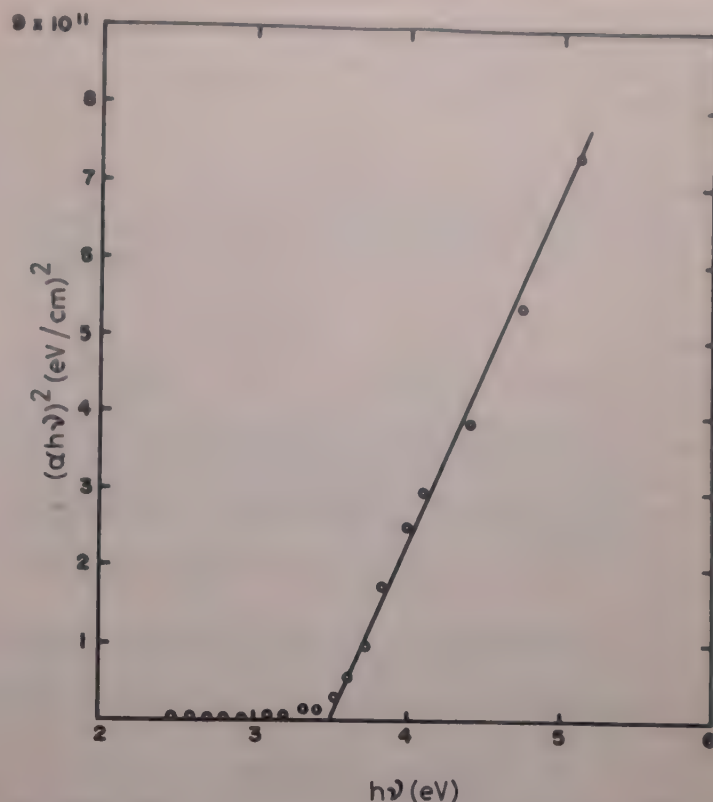


Fig. 8—Variation of $(\alpha h\nu)^2$ with photon energy ($h\nu$) for Sn:In(0:100) oxide

The (36:64) and (0:100) oxide films are identified as films having a single phase of crystalline In_2O_3 . The optical band gap obtained for In_2O_3 films is 3.5 eV as shown in Table 3 and Fig. 8. Raja *et al.*⁴⁹ found this value to be 3.55 eV. On adding Sn to the In_2O_3 films, the band gap increases to 3.7 eV for (36:64) oxide films (Fig.7). When this is seen in conjunction with the result that the resistivity of this film composition is lower than that of In_2O_3 film, the earlier explanation as given by Spence⁴³ and Arai⁴⁴ can account for the apparent increase in the band gap for this film as due to the filling up of the lower states in the conduction band. However, as stated earlier there is no direct experimental support for this.

4 Conclusion

When films of $\text{SnO}_2\text{--In}_2\text{O}_3$ are prepared using spray pyrolytic technique the crystallographic properties of the films are sensitive to composition of the film, temperature of deposition and underlying substrate. Indium addition progressively reduces the crystallite size of the SnO_2 films and decreases the degree of crystallization. At 34 mol % concentration, indium renders the film amorphous. Crystallization for SnO_2 depends on temperature of deposition while that for In_2O_3 depends upon the nature of the substrate material. Diffusion of alkali metal ions affects the films chemically and destroys the structure of the films.

Electrical properties vary with the composition of the films. Indium acts as an acceptor ion up to a certain

limit and then it forms a separate amorphous In_2O_3 phase side by side. This also changes the optical properties of the films.

Acknowledgement

The helpful discussions with Dr C A Menezes during the course of this work are gratefully acknowledged.

References

- 1 Dogil B, Froissart F & Horodecki A J, *J Phys D (GB)*, **12** (1979) 919.
- 2 Sundaram K B & Bhagwat G K, *Thin Solid Films (Switzerland)*, **78** (1981) 35.
- 3 Muranoi T & Furukoshi M, *Thin Solid Films (Switzerland)*, **48** (1978) 309.
- 4 Patel A R & Mysorewala D V, *Mater Res Bull (USA)*, **5** (1970) 1031.
- 5 Nath P & Bunshah R F, *Thin Solid Films (Switzerland)*, **69** (1980) 63.
- 6 Kawamata E & Ohshima K, *Jpn J Appl Phys (Japan)*, **18** (1979) 205.
- 7 Vossen J L, *RCA Rev (USA)*, **32** (1971) 289.
- 8 Bosnell J R & Waghorne R, *Thin Solid Films (Switzerland)*, **15** (1973) 141.
- 9 Hecq M, Dubois A & Van Cakenberghe J, *Thin Solid Films (Switzerland)*, **18** (1973) 117.
- 10 Thornton J A & Hedgcock V L, *J Vac Sci & Technol (USA)*, **13** (1976) 117.
- 11 Vainshtein V M, Fistul V I & Nikoleeva N, *Izv Akad Nauk SSSR Neorg Mater*, **7** (1971) 338.
- 12 Kostlin H, Jost R & Lems W, *J Electrochem Soc (USA)*, **123** (1976) 1889.
- 13 Lehmann H W & Widmer R, *Thin Solid Films (Switzerland)*, **27** (1975) 359.
- 14 Aitchison R E, *Aust J Appl Sci (Australia)*, **5** (1954) 10.
- 15 Miloslavskii V K, *Opt & Spectrosc (USA)*, **7** (1959) 154.
- 16 Ishiguro K, Sasaki T, Arai T & Imai I, *J Phys Soc Jpn (Japan)*, **13** (1958) 296.
- 17 Bartholomew R F & Garfinkel H M, *J Electrochem Soc (USA)*, **116** (1969) 1205.
- 18 Vincent C A, *J Electrochem Soc (USA)*, **119** (1972) 515.
- 19 Aboaf J A, Marcotte V C & Chou N J, *J Electrochem Soc (USA)*, **120** (1973) 701.
- 20 Sabnis A G & Feisel L D, *J Vac Sci & Technol (USA)*, **14** (1977) 685.
- 21 Kim H & Laitinen H A, *J Am Ceram Soc (USA)*, **58** (1975) 23.
- 22 Rohatgi A, Viverito T R & Slack L H, *J Am Ceram Soc (USA)*, **57** (1974) 278.
- 23 Ramanujam M A & Ghare D B, *J Indian Inst Sci*, **58** (1976) 254.
- 24 Manificier J C, Demurcia M & Fillard J P, *Thin Solid Films (Switzerland)*, **41** (1977) 127.
- 25 Shanthi E, Dutta V, Banerjee A & Chopra K L, *J Appl Phys (USA)*, **51** (1980) 6243.
- 26 Carison D E, *J Electrochem Soc (USA)*, **122** (1975) 1334.
- 27 Kane J, Schweizer H P & Kern W, *J Electrochem Soc (USA)*, **122** (1975) 1144.
- 28 Baliga B J & Ghandhi S K, *J Electrochem Soc (USA)*, **123** (1976) 941.
- 29 Fraser D B & Cook H D, *J Electrochem Soc (USA)*, **119** (1972) 1368.
- 30 Fan J C C, Bachner Frank J & Foley George H, *Appl Phys Lett (USA)*, **31** (1977) 773.
- 31 Muller H K, *Phys Status Solidi (Germany)*, **27** (1968) 723.
- 32 Tohda T, Wasa K & Hayakawa S, *J Electrochem Soc (USA)*, **123** (1976) 1719.
- 33 Carroll A F & Slack L H, *J Electrochem Soc (USA)*, **123** (1976) 1889.
- 34 Kuznetsow A Ya, *Sov Phys Solid-State (USA)*, **2** (1960) 30.
- 35 Tigane I F, *Sov Phys Solid-State (USA)*, **7** (1975) 212.
- 36 Kane J, Schweizer H P & Werner K, *J Electrochem Soc (USA)*, **123** (1976) 270.
- 37 Mizuhashi M, *J Non-Cryst Solids (Netherlands)*, **38** and **39** (1980) 329.
- 38 Mizuhashi M, *Thin Solid Films (Switzerland)*, **76** (1981) 97.
- 39 Mizuhashi M, *Thin Solid Films (Switzerland)*, **70** (1980) 91.
- 40 Fan J C C & Bachner F J, *J Electrochem Soc (USA)*, **122** (1975) 1719.
- 41 Kohnke E E, *J Phys & Chem Solids (GB)*, **23** (1962) 1557.
- 42 Summitt R, Marley J A & Borrelli M F, *J Phys & Chem Solids (GB)*, **25** (1964) 1465.
- 43 Spence W, *J Appl Phys (USA)*, **38** (1967) 3767.
- 44 Arai I, *J Phys Soc Jpn (Japan)*, **15** (1960) 916.
- 45 Ryujiro M & Shigemasha F, *Oyo Butsuri (Japan)*, **41** (1972) 134.
- 46 Groth R, *Phys Status Solidi (Germany)*, **14** (1966) 69.
- 47 Lyshenko S P & Miloslavskii V P, *Opt Spectrosc (USA)*, **8** (1960) 455.
- 48 Claret R, *Appl Phys (Germany)*, **2** (1973) 247.
- 49 Raja A, Agnihotri O P & Gupta B A, *J Phys D (GB)*, **10** (1977) 1871.

On Degradation of Sintered CdS-Cu₂S Solar Cell

S BANERJEE & H SAHA *

Department of Physics, University of Kalyani, Kalyani 741 235

Received 20 May 1982; revised received 6 September 1982

The degradation of sintered CdS-Cu₂S solar cell caused by the grain boundary diffusion of Cu⁺ ions has been investigated. Some methods suggested to control the rate of this degradation include incorporation of suitable impurities like indium, zinc and hydrogen gas in CdS layer; vacuum annealing and sintering at reduced pressure before cell fabrication. Incorporation of these impurities establishes a retarding built-in-field along the grain boundary to check Cu⁺ ion diffusion and consequently reduces degradation of cells. Hydrogen has proved to be the most beneficial of these doped impurities.

1 Introduction

Solar cells based on the CdS-Cu₂S heterojunction have been the subject of extensive research. Sintered polycrystalline CdS-Cu₂S solar cells are one of the most promising devices as photovoltaic convertor in view of their low cost, comparatively easier fabrication technology and energy payback consideration¹. But a critical concern of the CdS-based solar cells has been the problem of device degradation. This is particularly true with the devices which use Cu₂S as the photo-absorber. It has been observed that Cu₂S can degenerate to lower stoichiometry phases as a result of oxidation in room ambients, field assisted out-diffusion of copper and electro-chemical decomposition under normal operations². The lower stoichiometry Cu_xS phases may have much lower optical absorbance³ and poorer carrier transport properties⁴. Thus in sintered CdS-Cu₂S solar cells having a large number of randomly oriented grain boundaries, apart from degradation caused by atmospheric oxygen, an additional degradation mechanism resulting from Cu⁺ ion diffusion phenomena down the grain boundary plays an important role.

Degradation of polycrystalline CdS-Cu₂S solar cell is generally attributed to diffusion of Cu through its grain boundaries. Palz *et al.*⁵ have reported on how to partially eliminate this degradation through suitable doping and hence diffusion through CdS, although no explanation has been forwarded by them. In polycrystalline materials, the dominant diffusion mechanism at temperatures lower than that about half of the melting point of the solid is the diffusion through the grain boundaries of the material. It has already been reported⁶ that the direction of an electric field, whether a built-in field incorporated through a deliberate introduction of concentration gradient of suitable impurities across the polycrystalline material or an external field applied across the sample, plays a significant role in accelerating or retarding the grain

boundary diffusion. Such acceleration or retardation of grain boundary diffusion by a suitable built-in field by impurity doping has a remarkable effect in the long term degradation of polycrystalline solar cells. An attempt was, therefore, made by us to investigate in some detail the effect of impurities like indium, zinc and hydrogen gas incorporated in CdS layer, on the initial performance and degradation of sintered cells. In, Zn and H have been chosen as they are the most common impurities which can be easily doped and are likely to be present in different stages of fabrication of CdS-Cu₂S solar cells. All these impurities diffuse rather rapidly through the large grain boundaries of sintered CdS layer and act as shallow donors contributing thermally ionized electrons to the CdS. The cases of vacuum annealing and sintering at reduced pressure have also been investigated to determine the effect of removal of trapped oxygen impurity from the grain boundaries and creation of sulphur vacancies within CdS layer⁷. The present paper reports the role of these impurities and other methods applied, viz. vacuum annealing and sintering at reduced pressure on the long term degradation performance of polycrystalline solar cells.

2 Experimental Details

The sintered CdS-Cu₂S solar cells were fabricated in the same way as reported earlier⁸. The sintered CdS pellets of about 15 mm diameter and 1 mm thickness were formed by pressing (about 50 tons/sq in) suprapure grade CdS powder. They were sintered in inert atmosphere at 800°C for 3 hr and conventional cells were fabricated. To get better cell performance, different CdS layer treatments such as vacuum annealing, low pressure sintering or impurity doping were carried out, prior to cell fabrication. For vacuum annealing, the sintered (800°C, 3 hr) CdS pellets were annealed in vacuum (10⁻⁵ torr) at 200°C for 4 hr. Sintering at reduced pressure (0.5 torr) was carried out

at 600°C for 1½ hr in inert atmosphere. Indium was doped in CdS layer by vacuum plating pure metallic In on the back surface of CdS pellet and heated in air at 200°C for 4 hr (Ref. 9). In sintered CdS layer, Zn was doped from vapour phase at 400°C for 1 hr using standard evacuated glass ampoules. In sintered CdS pellet, hydrogen treatment was carried out at 400°C for 1 hr in closed atmosphere containing 9:1 nitrogen and hydrogen mixture.

After cell fabrication, all the cells, viz. impurity doped, vacuum annealed, low pressure and untreated conventional cells were encapsulated in a transparent glass fixture and kept continuously in argon ambient to avoid oxidation by open atmosphere. For studying the degradation of performance of these cells, short circuit current (J_{sc}), open circuit voltage (V_{oc}) were measured carefully at room temperature at the same intensity of illumination at a definite interval of time. A tungsten filament at 2800 K colour temperature fitted with a water filter was used as a source, dark $C-V$ measurements of the fresh and degraded cells were made in a capacitance bridge (Radart & Co., India) at 10 kHz frequency to investigate the junction behaviour of these cells.

3 Results and Discussion

Figs 1 and 2 show the variation of J_{sc} and V_{oc} with time for all the cells at room temperature. One notes that there is hardly any degradation of cells undergoing hydrogen treatment, vacuum annealing and low pressure sintering. For In and Zn doped cells, there is an initial degradation for the first 25 days until saturation is reached after which no further degradation takes place. For untreated, i.e. conventional cells, there is a rapid initial degradation for

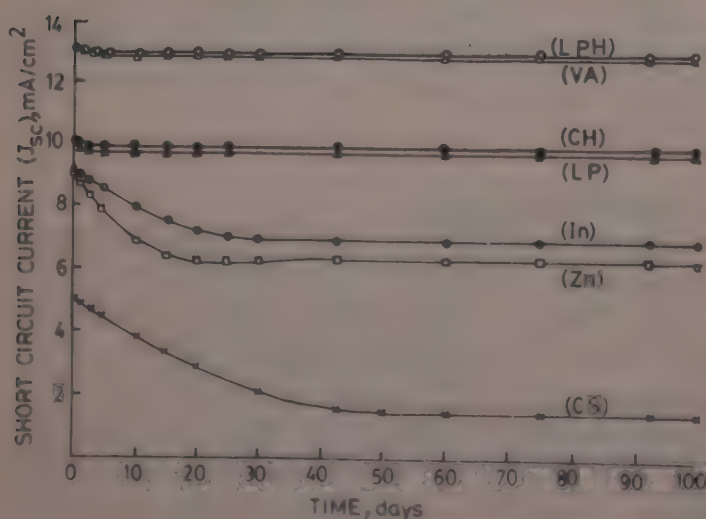


Fig. 1—Degradation of J_{sc} with time for different cells undergoing various CdS layer treatments [LPH, low pressure sintered and then hydrogen doped; VA, Vacuum annealed; CH, conventionally sintered with hydrogen doping; LP, low pressure sintered; In, In doped; Zn, Zinc doped; and CS, conventionally sintered (800°C, 3 hr) cells]

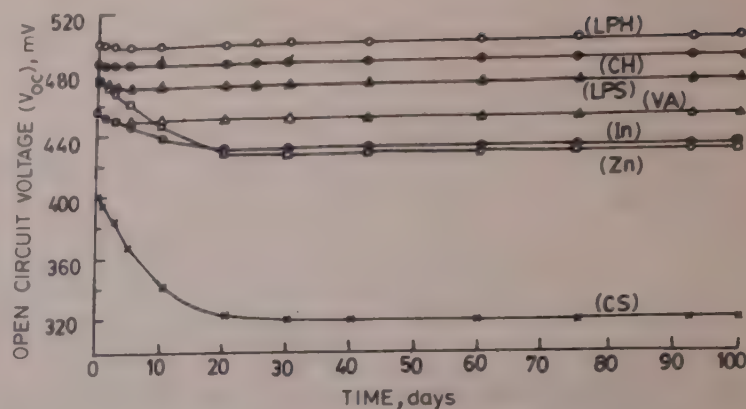


Fig. 2—Degradation of V_{oc} with time for different cells undergoing various CdS layer treatments

Table 1—Parameters of CdS-Cu₂S Solar Cell Undergoing Different Heat Treatments of the CdS Layer

Treatment on CdS layer	A-factor	V_{oc} mV	J_{sc} mA/cm ²	Fill factor	J_0 mA/cm ²
600°C, 1½ hr, H-doped, Low pressure	2.73	540	15.0	0.603	0.004
800°C, 3 hr, H-doped	3.5	500	13.0	0.538	0.024
800°C, 3 hr, In-doped	5.6	465	12.5	0.52	0.22
800°C, 3 hr, Zn-doped	5.5	490	12.0	0.49	0.19
Vacuum annealed	3.2	465	15.0	0.50	0.04
600°C, 1½ hr, Low pressure	5.21	490	13.5	0.443	0.14
800°C, 3 hr, Conventional cell	9.0	410	7.8	0.366	1.31

first 30 days and then slow degradation takes place for further 15 days after which saturation sets in.

3.1 Mechanism of Cell Degradation

The mechanism of degradation performance of polycrystalline CdS-Cu₂S solar cell may be explained as follows:

(a) The net effective positive space charge density (N_{Deff}) at the interface is increased because of the presence of diffused Cu⁺ ions down the grain boundaries. An accompanying effect on the cell is the increase in the value of the diode exponential factor (A) which is in fact dependent upon N_{Deff} at the depletion region, by the relation¹⁰

$$A = \frac{\hbar}{2kT} \left(\frac{qN_{Deff}}{m^* \epsilon \epsilon_0} \right)^{1/2} \quad \dots (1)$$

where $\hbar = (h/2\pi)$, h being the Planck's constant, k is the Boltzmann's constant, T the temperature of the device, q the electronic charge, m^* the effective mass of the electron, ϵ and ϵ_0 are respectively the permittivities of the medium and the free space. A , in its turn, has been reported¹¹ to be chiefly responsible for the large variation of saturation current density (J_0) of the cell (can be seen from Table 1) as is clear from the relation

$$J_0 = q N_c S_1 \exp\left(\frac{E_i - \phi_b}{AkT}\right) \quad \dots(2)$$

where N_c is the charge density in the CdS conduction band, S_1 the surface recombination velocity, E_i the ionization energy of the deep levels in the depletion region, and ϕ_b the potential barrier in the grain boundary region.

However, the single largest factor contributing to the decrease in V_{oc} of the cell is the large increase in J_0 values of the cells since V_{oc} of a polycrystalline solar cell is given by¹²:

$$V_{oc} = \frac{AkT}{q} \ln \left[\frac{J_{L0}}{(A_J/A_1) J_0} + 1 \right] \quad \dots(3)$$

where J_{L0} is the light generated current density with unity collection efficiency, A_J , the CdS-Cu₂S actual junction area, and A_1 the perpendicular area of the cell.

The degradation in V_{oc} values of the cells is thus seen to be due to the presence of diffused Cu⁺ ions down the grain boundaries.

On the other hand, increase in the positive spacecharge density at the interface increase ϕ_b and decreases the mobility of the CdS layer (μ) as is clear from the equation⁹

$$\langle \mu \rangle = \frac{q \langle V_{th} \rangle}{4 N_G k T} \exp(-q\phi_b/kT) \quad \dots(4)$$

where V_{th} is the thermal velocity of the carriers and N_G the number of grains per unit length. Using Rothwarf's expression for the light generated current density (J_L) (Ref. 12),

$$J_L = J_{L0} \left(\frac{1}{1 + S_1/\mu F} \right) \quad \dots(5)$$

where F is the field in CdS at the junction; it may be expected that the degradation in J_{sc} of the cell with time is through an increase in the factor $S_1/\mu F$ due to reduction in the value of electron mobility (μ) and junction field (F) in CdS layer. Vacuum annealing, low pressure sintering and doping of impurities like In, Zn and H minimize degradation. Released thermal electrons from the doped impurities tend to passivate the large number of deep levels in the grain boundaries, thereby reducing N_{Deff} in the depletion region and also the interface recombination velocity S_1 . N_{Deff} is also reduced in the cases of vacuum annealing and low pressure sintering by the removal of trapped oxygen from the grain boundaries. Reduction in N_{Deff} values leads to lower J_0 and higher V_{oc} values of the sintered cells. At the same time the increase in the electron concentration due to released thermal electrons in the CdS layer tends to increase μ and conductivity σ_0 of the CdS layer, thus increasing the J_{sc} values of the cells.

(b) Deficit of copper in the top Cu₂S layer may result in Cu_{2-x}S. Departure from ideal stoichiometry

significantly affects the electronic properties of Cu₂S, with both minority carrier transport and majority carrier conductivity, being controlled by the copper deficiency. The thickness of top Cu₂S layer (absorber layer) decreases with decrease in stoichiometry of Cu₂S. Since J_{sc} also depends on the carrier density and thickness of Cu₂S layer through the ratio of diffusion length (L) to the Cu₂S thickness (d) i.e. on d/L , the reduction of copper sulphide stoichiometry leads to reduction in J_{sc} (Ref. 13).

(c) In the Clevite model of the cell and most other models it is recognized that during the heat treatments usually given to a cell a compensated layer is formed in the CdS near the junction, i.e. *i*-CdS layer, the compensating center is probably copper which diffuses into the CdS from the Cu₂S layer. The compensation reduces the net donor density in this region to the order of 10¹⁴ cm⁻³ from the uncompensated density of about 10¹⁷ cm⁻³. Increase in the thickness of this copper compensated *i*-CdS layer in turn reduces J_{sc} and V_{oc} of the cell¹⁴.

The nature of degradation of J_{sc} and V_{oc} with time suggests diffusion mechanism associated with the degradation of the sintered cells. We propose that Cu⁺ ions diffuse through the grain boundaries resulting into deviation of stoichiometry from Cu₂S to Cu_{2-x}S. These Cu⁺ ions reach the accumulation surface⁶ developing a Cu-compensated *i*-CdS layer, thus reducing gradually J_{sc} and V_{oc} of the cells. That a Cu-compensated *i*-CdS layer is present even in our freshly prepared ceramic cells is manifested from the $C-V$ characteristics (Fig. 3), which are similar to those of MOS structure devices¹⁵. Except for hydrogen-treated cells where capacitance decreases with reverse bias, all other cells show an increase or no change in capacitance with reverse bias.

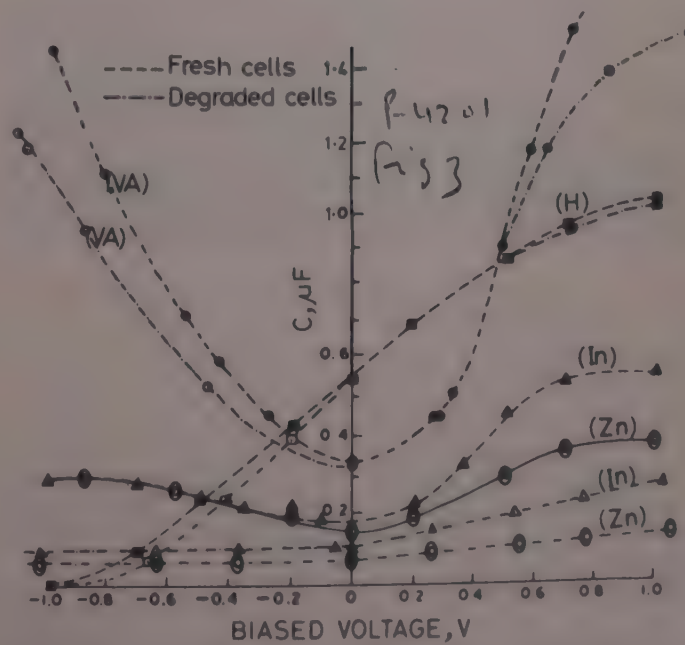


Fig. 3—Variation of (barrier) dark capacitance of different cells before and after degradation with both forward and reverse bias

The presence of oxygen impurity in the grain boundaries enhances the rate of Cu^+ ion diffusion. Removal of trapped oxygen by vacuum annealing and low pressure sintering retards the rate of Cu^+ ion diffusion along the grain boundary and consequently check cell degradation. The role of impurities like In, Zn and H in reducing cell degradation rate is probably different. All these impurities acting as shallow donors contribute thermally ionized electrons and diffuse rapidly through the grain boundaries. A general theoretical analysis about the role of the built-in field and its direction on the diffusion of Cu^+ ions has been carried out with the help of a single grain-structure model⁶.

3.2 Role of Built-in Field on Cu^+ Diffusion

Theoretical Analysis

Fig. 4 shows the array of parallel grain boundaries lying perpendicular to the accumulation surface. Accumulation surface has been assumed to have a finite capacity and finite diffusion coefficient (D_s) with effective thickness (W_s). The grain boundaries are represented by thin rectangular slab of uniform thickness (W_b) having a constant diffusion coefficient (D_b) and mobility μ_b . Assuming an electric field (E) being present along the grain boundaries as shown in Fig. 4, the diffusion equation for a positively charged diffusing species in the grain boundaries⁶ is

$$\frac{\partial C_b(y, t)}{\partial t} = D_b \frac{\partial^2 C_b(y, t)}{\partial y^2} + \mu_b E \frac{\partial C_b(y, t)}{\partial y} \quad \text{for } -l < y < 0 \quad \dots(6)$$

where C_b is the concentration of the diffusing species in the grain boundary and l the distance of separation between diffusion source and the accumulation surface; and in the accumulation surface is

$$\frac{\partial C_s(x, t)}{\partial t} = D_s \frac{\partial^2 C_s(x, t)}{\partial x^2} \quad \text{for } 0 < x < b \quad \dots(7)$$

where C_s is the concentration of the diffusing species in the accumulation surface.

The concentration on the accumulation surface averaged over x , that is \bar{C}_s , is obtained as

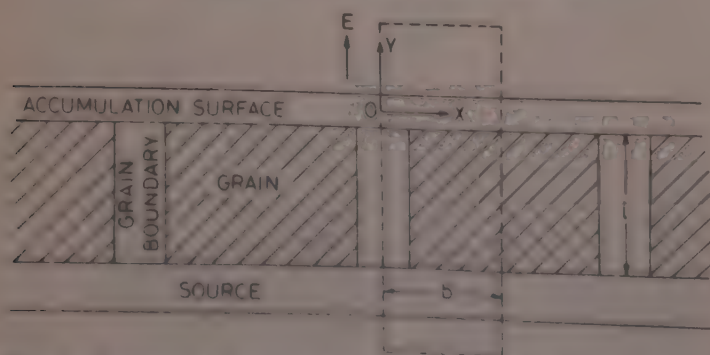


Fig. 4 Schematic diagram showing the geometry of the idealized surface accumulation grain boundary diffusion in the presence of an electric field

$$\begin{aligned} \bar{C}_s = \exp\left(-\frac{\mu_b El}{D_b}\right) - \sum_{m=1}^{\infty} \left\{ \frac{\theta_m W_b}{2D_b W_b b \beta_m^3} \sin(k\beta_m b) \right. \\ \times \exp\left[-\frac{\mu_b El}{2D_b}\right] \exp[-D_b \beta_m^2 t] \\ \left. \left[A_{1m} \cos(\beta_m l \theta_m) \cdot \cos(k\beta_m b) \right. \right. \\ + A_{2m} \sin(\beta_m l \theta_m) \cos(k\beta_m b) \\ + A_{3m} \cos(\beta_m l \theta_m) \sin(k\beta_m b) \\ \left. \left. + A_{4m} \sin(\beta_m l \theta_m) \sin(k\beta_m b) \right] \right\} \quad \dots(8) \end{aligned}$$

where $R = \frac{1}{2} W_b D_b$

$$S = W_s D_s$$

$$\theta_m = [1 - \mu_b^2 E^2 / 4 D_b^2 \beta_m^2]^{1/2} \quad \dots(9)$$

$$C_b = \sigma' C_b / C_o$$

$$C_s = \sigma' C_s / C_o \sigma$$

$$k = (D_b / D_s)^{1/2}$$

and C_o is assumed as constant source concentration, σ and σ' are segregation ratio with

$$\begin{aligned} A_{1m} &= \frac{R \alpha_m}{4k S D_b^2 \beta_m^3} - \frac{R}{k S \alpha_m \beta_m} \left(1 + \frac{W_b \mu_b E l}{4R}\right) \\ A_{2m} &= \frac{R l}{2k S D_b \beta_m} + \frac{W_b \mu_b E}{4k S D_b \beta_m^3} + \frac{\sigma b}{2k D_s \beta_m} \\ A_{3m} &= \frac{R b \alpha_m}{4 S D_b^2 \beta_m^2} + \frac{\sigma l}{\alpha_m} \end{aligned} \quad \dots(10)$$

$$A_{4m} = \frac{W_b \mu_b E b}{8 S D_b \beta_m^2}$$

$$\alpha_m = 2 D_b \beta_m \theta_m$$

and β_m is the m th positive root of the transcendental equation,

$$\tan(\beta l \theta) [W_b \mu_b E / 4k S \beta - \sigma \tan(k\beta b)] = -\theta R / k S \quad \dots(11)$$

The rate of grain boundary diffusion and hence the rate of average concentration (\bar{C}_s) of diffusing impurities in the accumulation surface can be computed with the help of Eq. (8). Fig. 5 shows the effect of the direction and magnitude of an electric field on the growth rate of \bar{C}_s corresponding to the case $D_b \gg D_s$, assuming $W_b \approx W_s$ and $b \approx l$. From Fig. 5, it is clear that whereas positive field helps in increasing \bar{C}_s , negative field decreases the rate of accumulation of \bar{C}_s . That is, a retarding field will check the rate of diffusion of impurities down the grain boundaries. The doped impurities like In, Zn and H are likely to develop a concentration gradient from the top surface of CdS pellet, resulting in a retarding built-in field that opposes the diffusion of copper ions through the grain

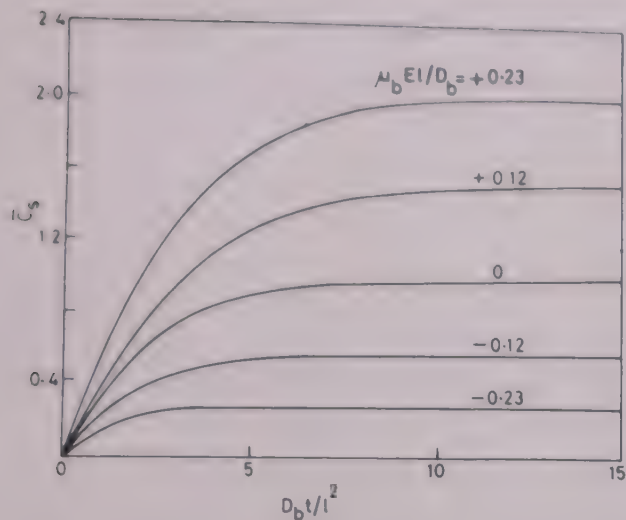


Fig. 5—Time dependence of \bar{J}_s with the electric field for the case when $D_b \gg D_s$.

boundaries in CdS-Cu₂S solar cells. In the case of hydrogen-treated cells, the rate of degradation is observed to be even less than that for In and Zn doped cells. This is perhaps due to the additional effect of hydrogen treatment generating a large number of sulphur vacancies at the CdS surface layer. These sulphur vacancies compensate for any copper vacancies resulting from the Cu⁺ ion diffusion from the top surface down the grain boundary and the deviation from stoichiometry is thus kept minimum in this case. Table 1 shows the improvement in J_{sc} values from 7.8 to 15.0 mA/cm² and in V_{oc} values from 410 to 540 mV. The improvement in fill factor is also remarkable.

4 Conclusion

Before fabrication of the cells, different CdS layer treatments such as vacuum annealing, low pressure sintering and suitable impurity incorporation have been found effective in view of their initial performance and reduction in degradation compared to untreated cells. In low pressure sintering and vacuum annealing, narrowing of grain boundaries due to better packing of grains compared to untreated cells (Fig. 6) and also the removal of oxygen impurities from the grain boundaries slow down considerably the rate of Cu⁺ ion diffusion, and consequently retard cell degradation. On the other hand, doped impurities like In, Zn and H in CdS layer act as shallow donors and contribute electrons to some of the acceptor states in the grain boundary region, thereby reducing $N_{D\text{eff}}$. The degradation of the cells is arrested significantly presumably through the development of a retarding built-in field arising out of the concentration gradient of the ionized impurities from the top surface of the CdS layer¹¹.

Out of all the impurities incorporated, hydrogen proves to be most beneficial probably because it enjoys an additional advantage of producing sulphur

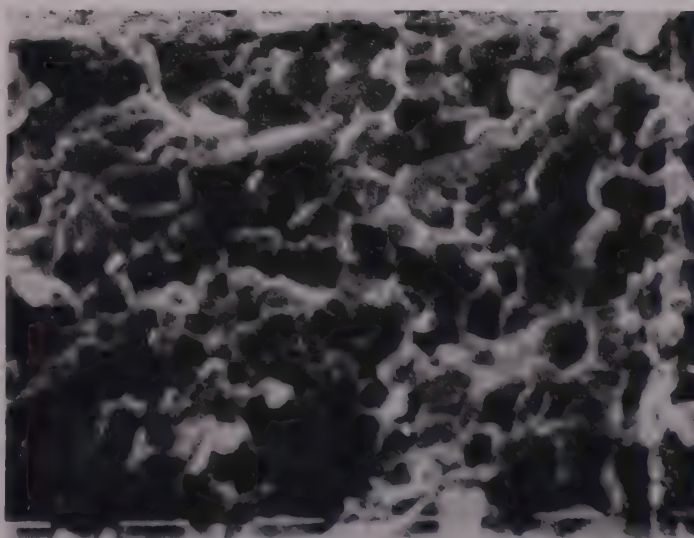
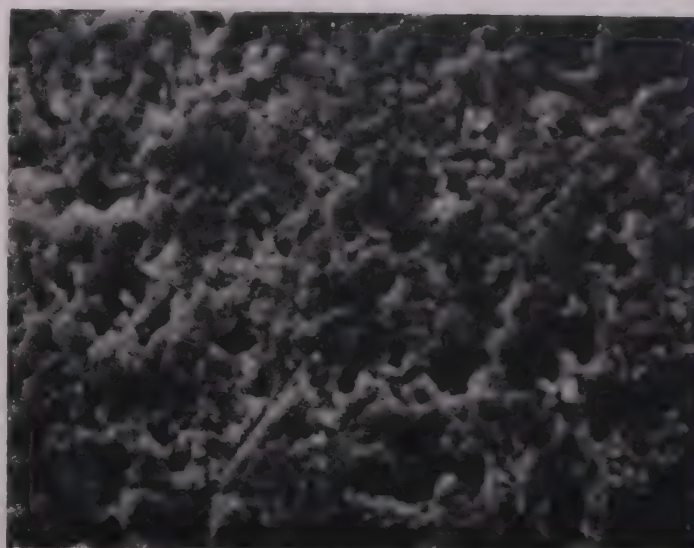
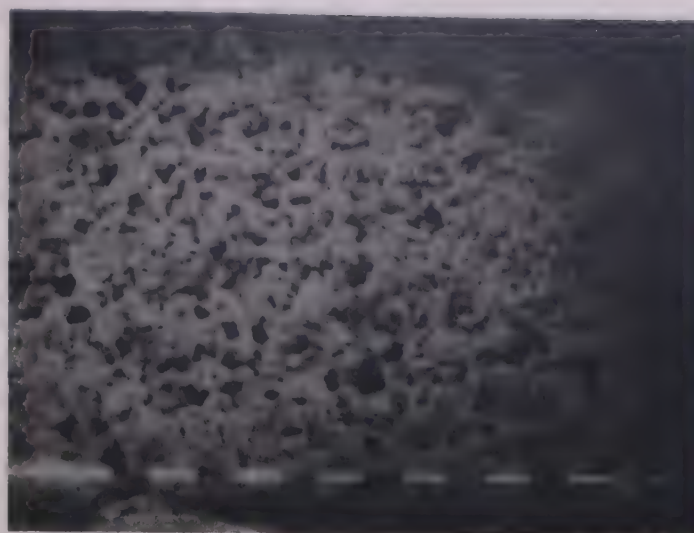


Fig. 6—SEM photographs of CdS layer sintered at (a) 800°C, 3 hr, vacuum annealed (pressure \approx 5 torr), (b) 600°C, 1½ hr, low pressure (pressure \approx 1 torr), (c) 800°C, 3 hr, conventionally sintered (pressure \approx 2 atm)

vacancies at the surface of CdS through the formation of H₂S. These sulphur vacancies help in increasing: (a) the mobility (μ) of CdS layer, and (b) the retarding built-in field, which opposes Cu⁺ ion diffusion through the grain boundary. For quantitative investigations of these effects, further studies are necessary.

Acknowledgement

One of the authors (SB) acknowledges with thanks the financial support received from the University of Kalyani, to complete this work.

References

- 1 Nakayama N, *Jpn J Appl Phys (Japan)*, **8** (1969) 450.
- 2 Rickert R, Wedde C, Palz W, *et al.*, *Proceeding of the Eleventh IEEE Photovoltaic Specialists Conference*, Phoenix, Arizona, May 1975 IEEE, New York, (1975) 439.
- 3 Mulder B J, *Phys Status Solidi a (Germany)*, **13** (1972) 79.
- 4 Leoug J Y, *Optical and transport properties of reactively sputtered Cu_xS* , Ph D dissertation, Solar Energy Research Institute, Colorado, USA, 1980.
- 5 Palz W, Besson J, Nguyen Duy T & Vedel J, *Proceeding of the Ninth Photovoltaic Specialist Conference*, 2-4 May 1972, Silver Spring, Maryland, USA, IEEE, New York (1972) 91.
- 6 Saha H & Mukhopadhyay K, *J Appl Phys (USA)*, **51** (1980) 6165.
- 7 Bube R H, *Photoconductivity of solids* (John Wiley, New York), 1960, 188.
- 8 Saha H, Basu P, Mukhopadhyay K & Sen Gupta S, *Indian J Pure & Appl Phys*, **17** (1979) 215.
- 9 Mukhopadhyay K & Saha H, *Solar Cell (GB)*, **4** (1981) 135.
- 10 Haines W G & Bube R H, *IEEE Trans Electron Devices (USA)*, **ED-27**, (11) (1980) 2133.
- 11 Banerjee S & Saha H, *J Phys D (GB)*, **16** (2) (1983) 185.
- 12 Rothwarf A, *International Workshop on cadmium sulphide solar cells and other abrupt heterojunctions*, (University of Delaware, Newark) 30 April to 2 May (1975) 9.
- 13 Windawi H W, *Proceeding of the international workshop on cadmium sulphide solar cell and other abrupt heterojunctions* (University of Delaware, Newark) 30 April-2 May (1975) 177.
- 14 Hall R B & Singh V P, *J Appl Phys (USA)*, **50** (1979) 6406.
- 15 SZe S M, *Physics of semiconductor devices* (John Wiley, New York) 1969.

Reflectivity of Tellurium Thin Films

I P JAIN*

Department of Physics, University of Rajasthan, Jaipur 302 004

Received 1 August 1981; accepted 6 January 1983

Tellurium thin films obliquely deposited by vacuum evaporation method on to Corning 7059 glass substrate at a pressure of 5×10^{-5} torr have been found to be optically anisotropic. A study of the reflectivity in the visible region of electromagnetic spectrum has been made as a function of angle of incidence (ψ), wavelength of light (λ), thickness (t) of the film and deposition angle (θ) of the film. It is observed that the films develop a coarse structure as t or θ increases. When the illumination of the film is with polarized light, the reflectivity of the film has different values for directions of the light vector parallel and perpendicular to the direction of deposition. This is explained on the basis of 'self-shadowing' effect which occurs during deposition. In obliquely deposited films, the growing crystallites cast shadows behind them and they grow in the direction of the vapour beam. A light beam passing through such a film, suffers greatest absorption and transmission and minimum reflection when the electric vector is parallel to the long axis of the crystallites. Accordingly, the obliquely deposited films are optically anisotropic. The anisotropy in reflectivity of tellurium films increases with the increase in θ , and is negligible for films deposited normally.

1 Introduction

Obliquely deposited tellurium films have been shown to exhibit optical anisotropy. When polarized light is incident on such oblique incidence film, the transmission is found to depend on the orientation of electric vector of the incident light. This effect was first studied in oblique incidence films by Bergholm¹ and then by Cau². This type of anisotropy has also been studied by Smith *et al.*³ in Permalloy films, Nakai⁴ and Pandya and Chopra⁵ in germanium films and Tanaka and Takahashi⁶ in aluminium films. Jain *et al.*⁷ have found that the obliquely deposited Te films exhibit resistivity anisotropy. A study of reflectivity of such films has been made for the visible region of electromagnetic spectrum, and the results are presented in this paper.

2 Experimental Details

2.1 Sample Preparation

Tellurium films of thickness 300, 400 and 450 Å in 20 mm × 20 mm area were prepared on to Corning 7059 glass substrate (25 mm × 25 mm × 0.625 mm thick) at different deposition angles by evaporation of bulk material (Koch Light 99.999% pure) in a vacuum system maintained at a pressure of 5×10^{-5} torr using a conventional oil diffusion pump backed by a two-stage rotary pump. The film thickness and deposition rate for each deposition angle were measured separately using a quartz crystal thickness monitor. The rate of deposition was approximately 10 Å/s, and the substrate was kept at room temperature.

The geometry of the film sample is shown in Fig. 1(a) which also shows the arrangement for deposition of tellurium at an oblique angle of incidence. The structure of such films is shown in Fig. 1(b).

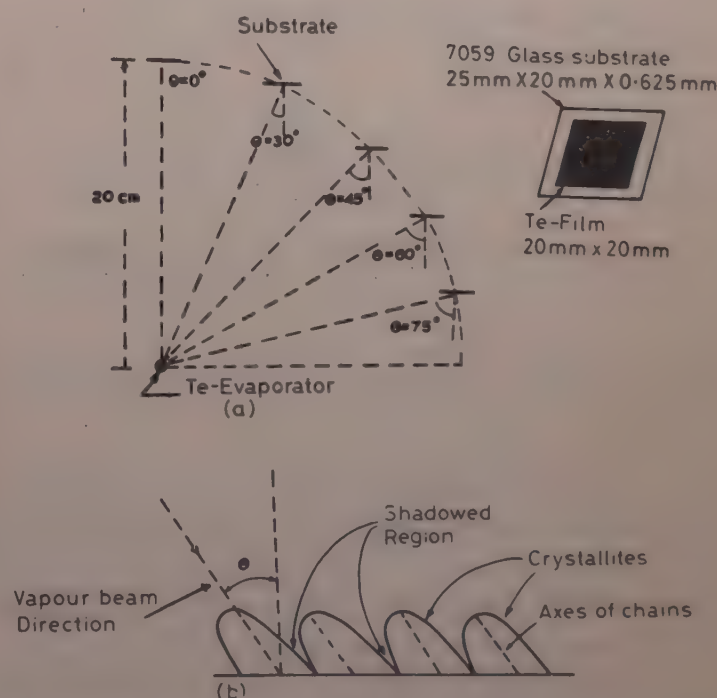


Fig. 1—(a) Schematic diagram of oblique deposition of tellurium film (angle θ is the deposition angle); (b) Structure of Te-films obliquely deposited

2.2 Apparatus for the Determination of Reflectivity of Thin Tellurium Films

The instrument on the lines suggested by Abeles⁸ was used for the measurement of reflectivity of thin tellurium films. In Fig. 2 a conventional research spectrometer with scale sensitivity of 1 minute is shown along with a source and detector. The light source used is a mercury lamp from which the monochromatic light is generated by putting the mercury light filter between the collimator and source. The film is placed on the prism table using a film holder which holds the film in a vertical plane.

An RCA photomultiplier (PM) tube 1P28 was used for measuring the intensities of the incident and

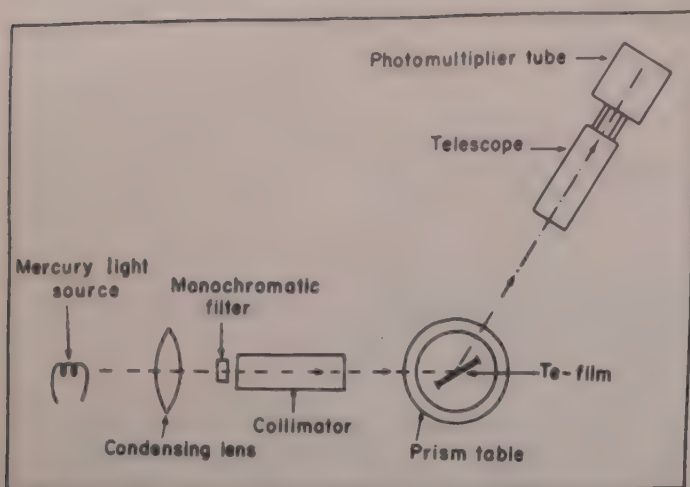


Fig. 2—Instrument for measuring reflectivity of thin tellurium films

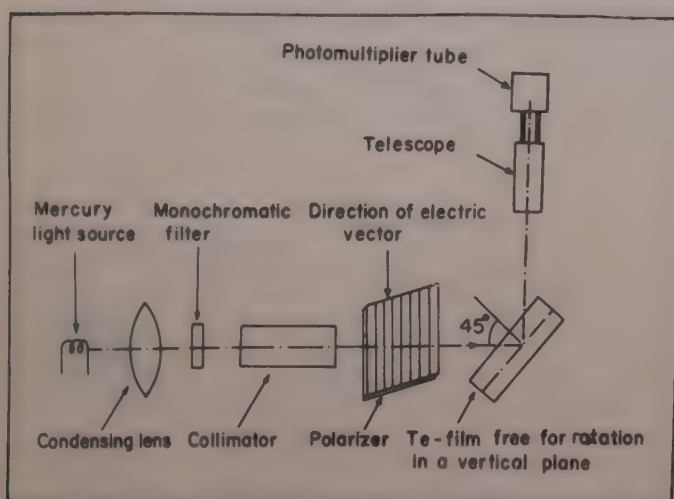


Fig. 3—Schematic diagram of the experimental set-up for determining reflectivity anisotropy of Te-film obliquely deposited ($\psi = 45^\circ$)

reflected beam of light. The PM tube is mounted in a light proof enclosure and attached to the telescope of the spectrometer replacing the eye piece. The photocathode of the PM tube is adjusted and exposed to the image formed at the telescope end.

For measuring the current which is proportional to the intensity of light, a dc microammeter of the range 0-500 μ A is incorporated in the output circuit of the PM tube.

Fig. 3 shows the experimental arrangement for studying the anisotropy of reflectivity. A polarizer is attached to the collimator of the spectrometer and the film is fixed on a holder which can rotate the film around a vertical plane.

3 Adjustments and Measurements

For the arrangement of Fig. 2, filters (supplied by Carl Zeiss Jena, Germany) of different wavelengths as shown in Fig. 4 have been used. The film coated substrate is fixed in the holder of the prism table of the spectrometer. The height of the prism table is adjusted to make all the light fall normal to the film surface. The prism table can be adjusted for the required angle of

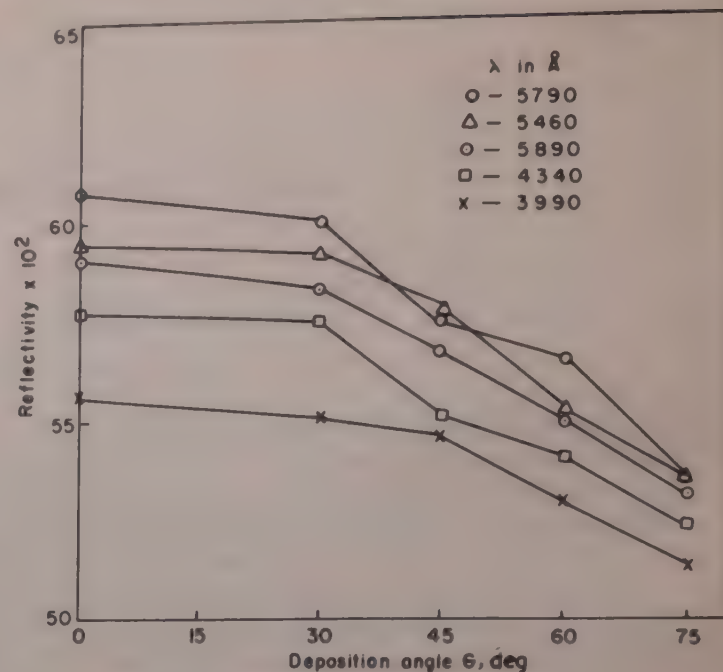


Fig. 4—Reflectivity of films as a function of θ for various values of λ [$t = 450$ Å, $\psi = 45^\circ$]

incidence of light beam at the film surface. The PM tube with its telescope arm can be rotated to receive the reflected light from the film surface. The PM current corresponding to incident and reflected light is measured to determine the reflectivity of the film.

The experimental arrangement of Fig. 3 is used to measure the anisotropy of reflectivity. Films deposited at angles 0, 30, 45, 60 and 75 deg having a thickness of 450 Å in each case are used. Each film is fixed vertically on the prism table and the incident light made an angle of 45° with the film surface. A provision is also made to rotate the film about the normal to the surface of the film. The film is rotated on an interval of 30° for full rotation that is 0° to 360° and the intensity of reflected light was measured at each angle.

4 Results and Discussion

The various factors influencing optical reflectivity are discussed in the following different subsections.

4.1 Effect of Angle of Incidence of Monochromatic Light

Fig. 5 shows the relation between the reflectivity of tellurium thin film and the angle of incidence of (ψ) of monochromatic light beam. The reflectivity of the film increases with the increase in angle of incidence of light beam for different deposition angles (θ). The mechanism of the reflection in the oblique incidence film has been discussed by Holland^{9,10} and this type of reflectivity is named as specular reflectivity. It is suggested^{9,10} that the reflectivity increases with the angle of incidence of light beam and our results are in confirmation with this observation (Fig. 5).

The nature of dependence of the reflectivity on the angle of incidence suggests, that the elevation of the

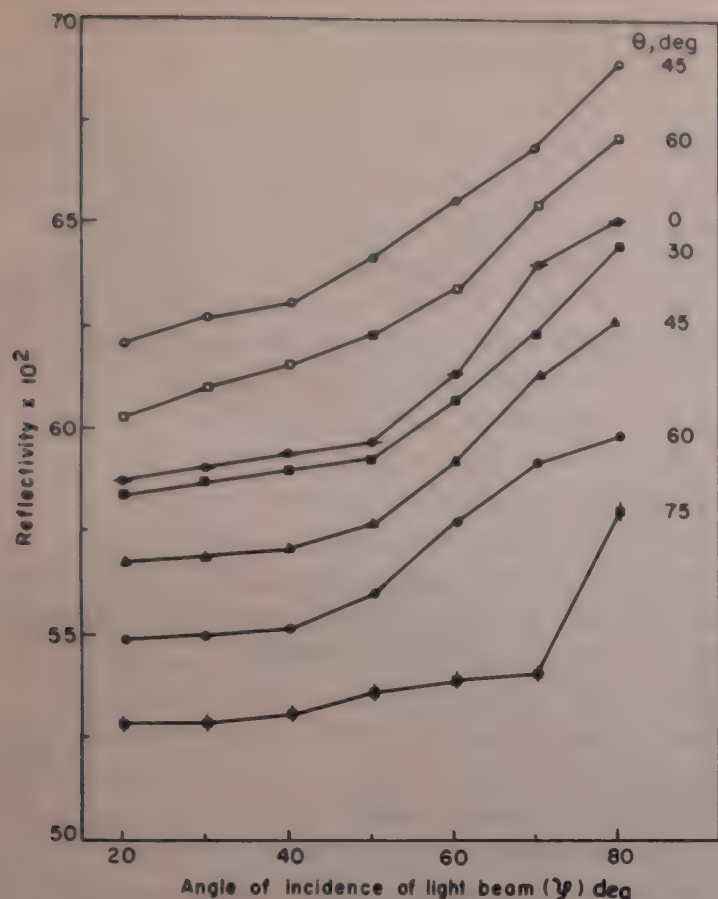


Fig. 5—Change in reflectivity of tellurium thin films with the angle of incidence (ψ) of light beam for various values of θ [$t = 450 \text{ \AA}$ and $\lambda = 5460 \text{ \AA}$]

crystallites of the film deposited at an oblique angle changes with the deposition angle. This change in elevation is introduced by the self-shadowing effect that occurs during the oblique deposition as shown in Fig. 1(b). The growing crystallites prevent the impinging atom from reaching the substrate where the crystallites cast shadows leaving undeposited areas shown as shadowed region in Fig. 1(b). Hence, in forming a film, all the crystallites grow long, crosswise to the direction of deposition. When the deposition angle is larger, the crystallites grow more inclined; therefore the areas of the boundaries become larger and the crystallites are considered to touch one another more loosely.

Fig. 5 also shows the asymmetry in the reflectivity from an obliquely deposited tellurium film. In Fig. 5 the 'solid points' show the reflectivity of the film when incident light is from the side of vapour beam (direction of deposition) and 'open points' when incident light is from the opposite side (normal to the direction of deposition). Fig. 5 shows a difference between the reflectivities corresponding to the solid and open points. It can be seen that the solid-point reflectivity is less than that corresponding to the open points. This is because when light falls from the side of vapour beam there is more absorption and transmission due to the structure of the film. This suggests that the crystallites of the film deposited at an oblique angle of incidence are asymmetrical in their shape.

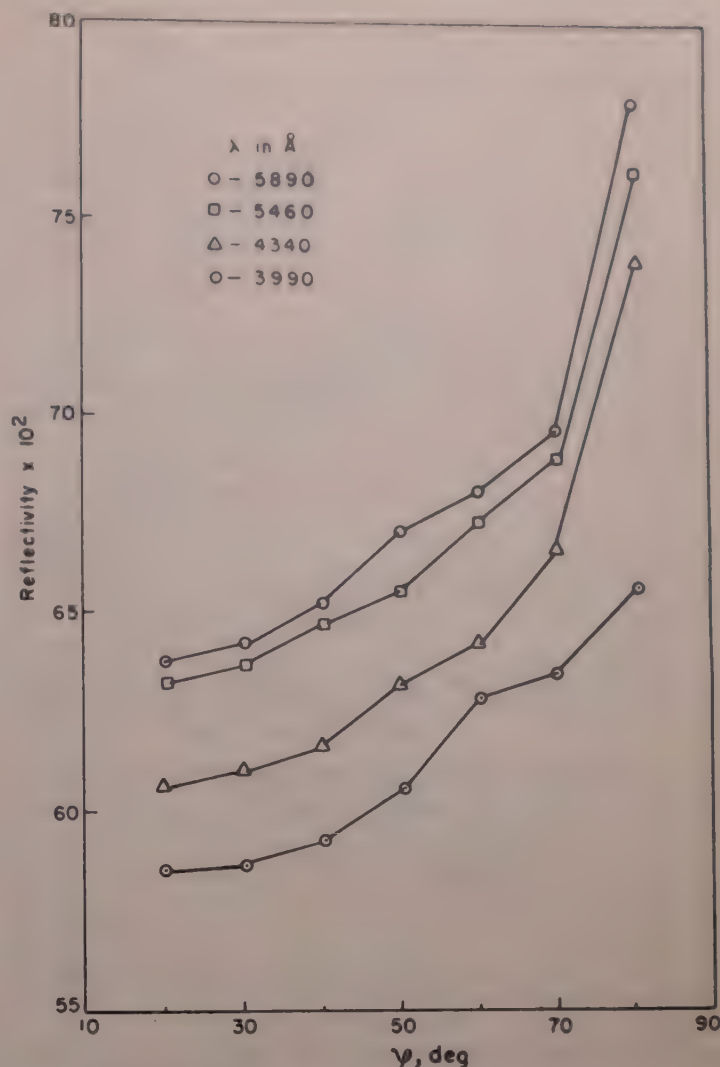


Fig. 6—Reflectivity of films as a function of ψ for various values of λ [$t = 300 \text{ \AA}$, $\theta = 45^\circ$]

4.2 Effect of Wavelength of Incident Light

Fig. 6 shows the change in reflectivity with angle of incidence ψ for different wavelengths of light. The reflectivity of tellurium film increases with the increase in wavelength of incident light. This is in accordance with the result of Holland⁹ where a surface having lower reflectivity for shorter wavelengths will show higher reflectivity for longer wavelengths.

4.3 Effect of Deposition Angle

The reflectivity as a function of θ is shown in Fig. 4 for different wavelengths of light and in Fig. 7 for different ψ of monochromatic light. From Figs 4 and 7 a difference in the reflectivity is found for different values of θ . It is clear from Figs 4 and 7 that the reflectivity of tellurium films decreases as θ increases. This suggests that as θ increases, the areas of the shadowed region also increases. In such films the transmission and absorption increases resulting in low reflectivity. We may say that the surface of a film prepared by oblique incidence evaporation becomes more coarse as θ increases.

4.4 Thickness Effect

Fig. 8 shows the relation between reflectivity and ψ of light beam for different film thicknesses keeping θ of

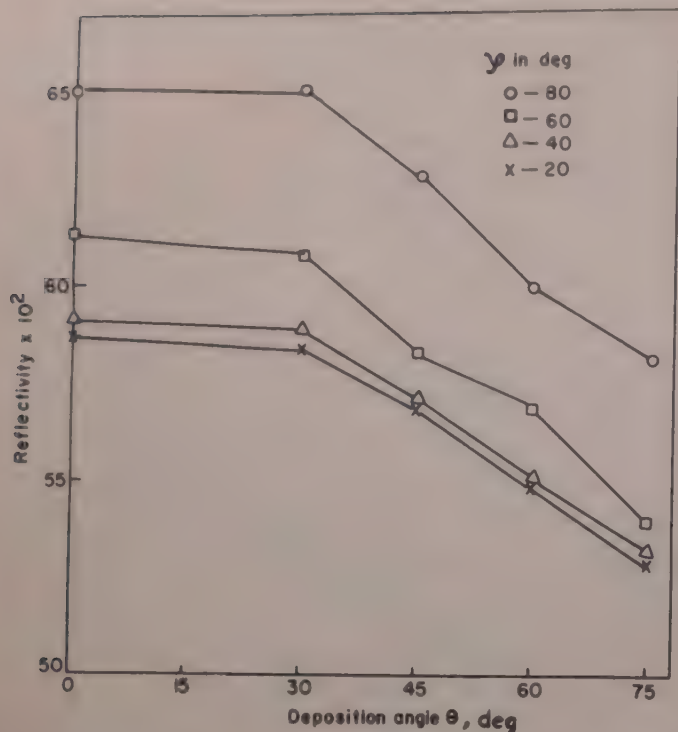


Fig. 7—Reflectivity of films as a function of θ for various values of ψ [$\lambda = 5460 \text{ \AA}$, $t = 450 \text{ \AA}$]

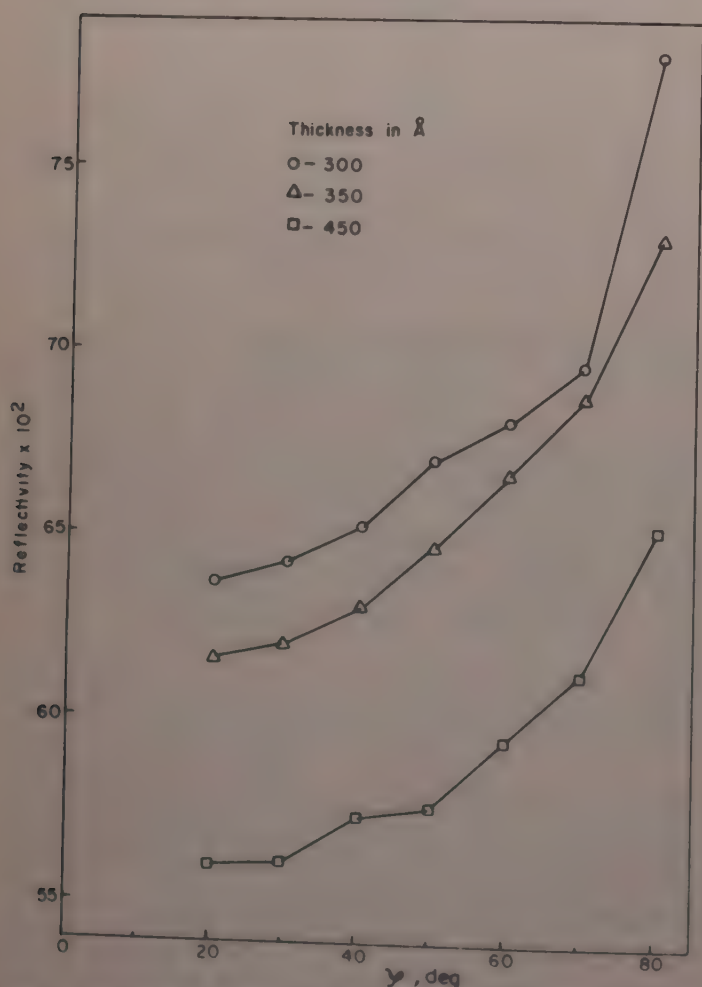


Fig. 8—Reflectivity of films as a function of ψ for various values of t ($\lambda = 5890 \text{ \AA}$, $\theta = 45^\circ$)

the film constant equal to 45. It is found that the reflectivity decreases as the film thickness increases from 300 to 450 Å. This decrease in reflectivity is due to increasing columnar growth¹¹ in thicker films which introduces more shadowed region.

4.5 Effect of Rotation of Films when Light is Polarized (Optical Anisotropy)

Tellurium films, obliquely deposited, are shown to exhibit optical anisotropy when polarized light is incident on it; the reflectivity is found to depend on the orientation of electric vector of the incident light.

R_{\perp}/R_{\parallel} factor is a measure of anisotropy of a film, where R_{\perp} and R_{\parallel} are the reflectivities of film perpendicular and parallel to the long axes of the chains of the film. These chains are the results of columnar growth of the film formed during oblique deposition¹¹. In oblique incidence film, the tendency for the grains to grow in the direction of the vapour beam causes the interstices (shadow region, or interspace between the crystallites) also to tilt in that direction. This explains why oblique incidence films are considerably transparent when the film is viewed with the light rays almost parallel to the vapour beams. A comparatively larger proportion of the light will pass unabsorbed through the interstices with a maximum at the angle of incidence where the interstices and light direction coincide. Similarly, the absorption will also be maximum (as compared to other directions of incidence of light beam) because the light may be multiply reflected in the shadowed region, thereby suffering more absorption.

Fig. 9 gives the variation of reflectivity of Te thin films with the direction of electric vector of the incident plane-polarized light. The orientation of the electric

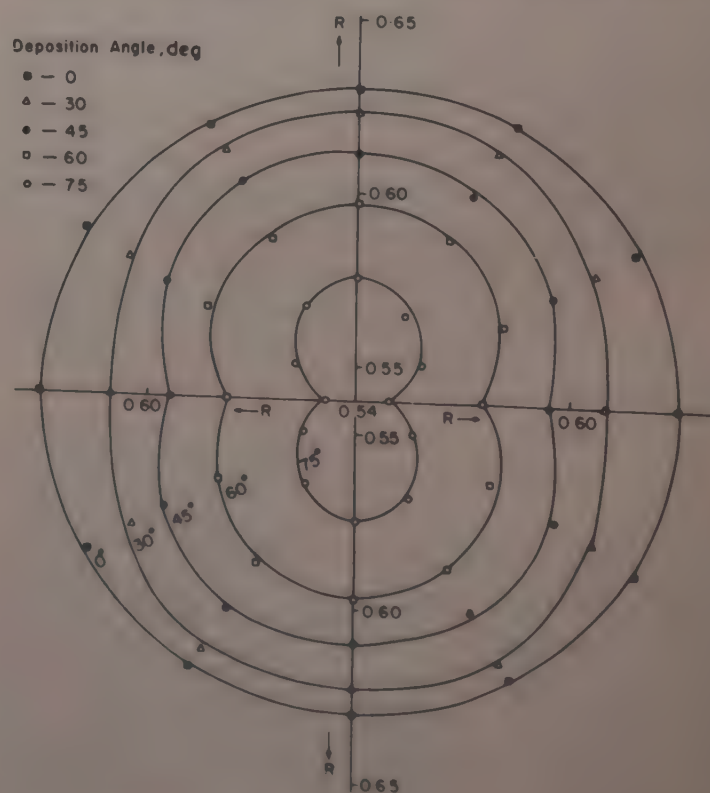


Fig. 9—Variation of the reflectivity with the direction of electric vector of the incident plane polarized light [x-axis shows the reflectivity when the direction of the films coincides with the direction of electric vector of the incident polarized light. $t = 450 \text{ \AA}$, $\lambda = 5890 \text{ \AA}$. Error in the measurement of reflectivity = 0.0036.]

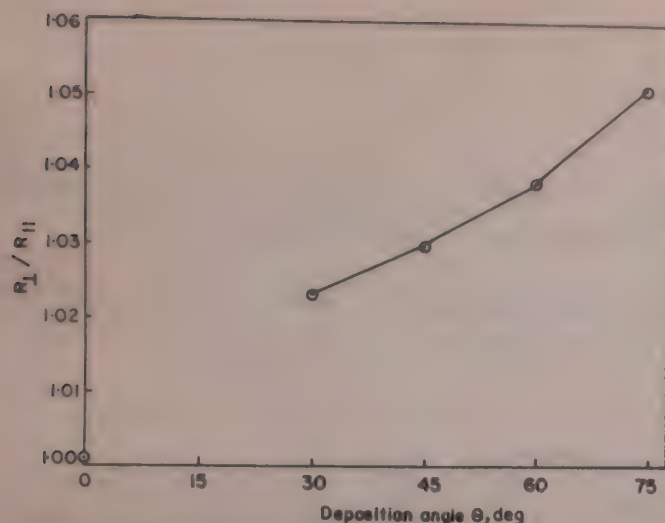


Fig. 10—Ratio of 'perpendicular' reflectivity (R_{\perp}) to the 'parallel' reflectivity (R_{\parallel}) as a function of θ (Error in the measurement of reflectivity is ± 0.0036 .)

vector is determined with the help of a polarizer and analyzer.

From Fig. 9 it is clear that the reflectivity of the obliquely deposited tellurium film has different values in directions parallel and perpendicular to the direction of deposition. Therefore, light when passing through such a film of oriented long crystallites, shows maximum transmission and absorption when the electric vector is parallel to the long axes of the crystallites, and the reflectivity in such a case is minimum (Fig. 9).

Fig. 10 shows anisotropy of reflectivity (R_{\perp}/R_{\parallel}) as a function of deposition angle (θ). It is clear from the figure that the anisotropy of reflectivity increases with the increase in θ . The anisotropy is negligible for films deposited normally.

5 Conclusions

1 The reflectivity of tellurium films increases with the increase in angle of incidence of monochromatic light beam.

2. The relectivity of tellurium films increases with the increase in wavelength of the incident light.

3 The reflectivity of the films decreases as the angle of deposition increases. The asymmetrical nature of reflectivity suggests that the crystallites of the films deposited at an oblique incidence are asymmetrical in structure.

4. The reflectivity also decreases with the increase in film thickness. This appears to be due to the increasing columnar growth in thicker films which introduces larger shadowed region.

5. The reflectivity of Te films depends upon the orientation of the electric vector of the incident plane polarized light. When a light beam passes through a film of oriented long crystallites, it shows maximum transmission when the electric vector is parallel to the long axis of the crystallites and hence the minimum reflectivity.

6. The anisotropy of reflectivity increases with increase in the deposition angle of the film, and is negligible for films deposited normally.

References

- 1 Bergholm C, *Ann Phys (USA)*, **43** (1914) 1.
- 2 Cau M, *Ann Phys (USA)*, **11** (1929) 354.
- 3 Smith D O, Cohen M S & Weiss G P, *J Appl Phys (USA)*, **31** (1960) 1755.
- 4 Nakai J, *Oyo Butsuri (Japan)*, **32** (1963) 91.
- 5 Pandya D K & Chopra K L, *Phys Status Solidi a (Germany)*, **35** (1976) 725.
- 6 Tanaka S & Takahashi T, *Oyo Butsuri (Japan)*, **32** (1963) 173.
- 7 Jain I P, Thakur D K & Garg J C, *Indian J Pure & Appl Phys*, **13** (1975) 432.
- 8 Abeles S F, *J Opt Soc Am (USA)*, **47** (1957) 473.
- 9 Holland L, *Vacuum deposition of thin films* (Chapman and Hall, London) 1970, 330.
- 10 Holland L, *J Opt Soc Am (USA)*, **43** (1953) 376.
- 11 Jain I P, *Electrical and optical properties of tellurium thin films*, PhD thesis, University of Rajasthan, Jaipur, 1975.

Dielectric Parameters for Semiconducting As-Ge-Te and Se-Ge-Te Glassy Alloys: Part I—Dielectric Dispersion in Glasses

K K SRIVASTAVA*, D R GOYAL**, K N LAKSHMINARAYAN & RENU VERMA

Department of Physics, Panjab University, Chandigarh 160014

and

F HUFNAGEL

Institut für Physik, Johannes Gutenberg Universität, 6500 Mainz, West Germany

Received 26 June 1982

Recent work on dielectric properties of semiconducting As-Ge-Te and Se-Ge-Te glasses has been critically examined with a view to highlighting the problems associated with dielectric measurements for glasses having large conductivity. The theoretical and experimental results, reported in this paper, provide an evidence of weak dielectric dispersion in these glasses. A large variation of dielectric permittivity with respect to temperature and frequency, as reported earlier, appears to be primarily due to imperfect contact.

1 Introduction

In our recent communications^{1,2}, we have reported dielectric parameters for a variety of As-Ge-Te and Se-Ge-Te alloys. All these glasses displayed almost a similar behaviour of dielectric constant with respect to temperature and frequency. A typical example of $\text{As}_{10}\text{Ge}_{15}\text{Te}_{75}$ is shown in Fig. 1. Our results for some silver-doped $\text{As}_{10}\text{Ge}_{15}\text{Te}_{75}$ glasses³ also showed the same trend, i.e. the dielectric constant remained independent of temperature and frequency at low temperatures but, as the temperature was increased beyond the room temperature, a strong dielectric dispersion ($> 100\%$) was observed for all the materials at frequencies 0.5 to 5.0 MHz. A large change of more than a factor of two (Fig. 1) in relative permittivity for all the glasses emphasizes the need for a critical analysis of the sample-system, particularly when all the materials¹⁻³ have a relatively large conductivity (10^{-5} - $10^{-3} \Omega^{-1}\text{-cm}^{-1}$) and the measurements were made without coating the sample†. Guillaud *et al.*⁴ also reported strong dielectric dispersion around 1 kHz at room temperature for the uncoated samples of selenium. Incidentally, their samples also had conductivity $\sim 10^{-6} \Omega^{-1}\text{-cm}^{-1}$. Similarly, Tsugane *et al.*⁵ observed strong dispersion in kHz-MHz range for As-Te glasses which had dc conductivity lying between 10^{-4} and $10^{-6} \Omega^{-1}\text{-cm}^{-1}$. Incidentally, these authors also made measurements on uncoated samples.

It is well known that an imperfect contact gives rise to spurious dielectric dispersion in cases of conducting

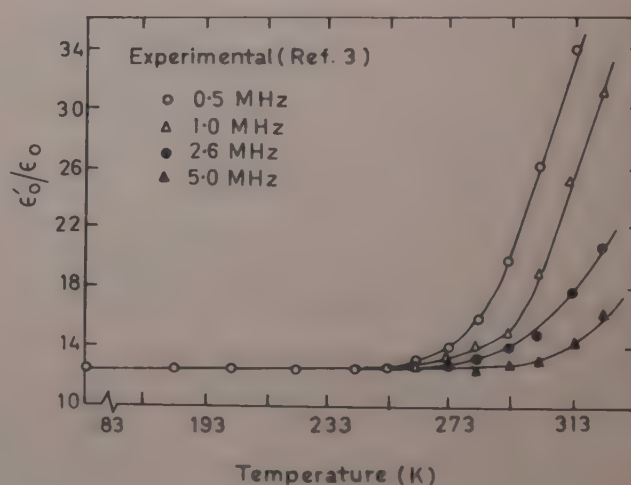


Fig. 1—Variation of dielectric permittivity (ϵ'/ϵ_0) with temperature and frequency for the uncoated sample of semiconducting alloy $\text{As}_{10}\text{Ge}_{15}\text{Te}_{75}$

materials. One can, therefore, utilize the known concepts for a quantitative estimation and a critical examination of such spurious dielectric dispersions in case of semiconducting glasses. The present work is an effort in this direction.

2 Theoretical Considerations

From Fig. 2 (a and b) the uncoated sample can be considered⁶ to be equivalent to a system consisting of (a) the sample material having conductivity σ_1 , and real dielectric constant ϵ'_1 , and (b) air-film having dielectric constant $\epsilon'_2 (= \epsilon_0$, permittivity of free space) and negligibly small conductivity $\sigma_2 (\approx 0)$. The sample material, can therefore, be characterized with the complex dielectric constant $\epsilon_1 = \epsilon'_1 - i\sigma_1/\omega$ and the system of Fig. 2(b) would behave as if the material had a dielectric constant given by:

$$\epsilon = \frac{(\epsilon'_1 - i\sigma_1/\omega)\epsilon_2}{(\epsilon'_1 - i\sigma_1/\omega)f_2 + \epsilon'_2 f_1} \quad \dots (1)$$

* Present address: Department of Physics, M D University, Rohtak

† Electrode elements are well known to diffuse into these materials. Therefore, uncoated samples were preferred to avoid errors due to migration of these elements, particularly when measurements are made at higher temperatures. This obviously resulted in an imperfect contact between electrodes and the surface of the sample.

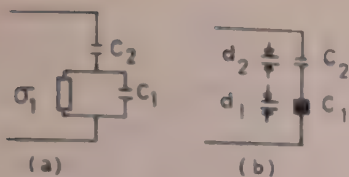


Fig. 2(a)—Schematic diagram of an uncoated sample [C_2 represents the capacitance of the air film; C_1 and σ_1 are the capacitance and the conductivity of the material respectively.]

Fig. 2(b)—Equivalent circuit of the system shown in (a) [d_1 and d_2 are the thicknesses of the material and air film respectively.]

where $f_1 = d_1/(d_1 + d_2)$ and $f_2 = d_2/(d_1 + d_2)$

Eq. (1) predicts that:

(a) If $\omega \rightarrow 0$ (condition for static dielectric constant),
 $\epsilon \rightarrow \epsilon_s \approx \epsilon'_2/f_2$... (2)

(b) If $\omega \rightarrow \infty$ (condition for optical dielectric constant),

$$\epsilon \rightarrow \epsilon_{op} \approx \frac{\epsilon'_1 \epsilon'_2}{\epsilon'_1 f_2 + \epsilon'_2 f_1} \quad \dots (3)$$

From Eqs (1)-(3), it follows that:

$$\frac{\epsilon - \epsilon_{op}}{\epsilon_s - \epsilon_{op}} = \frac{1}{1 + i\omega\tau} \quad \dots (4)$$

$$\text{where } \tau = \left[\frac{\epsilon'_1 f_2 + \epsilon'_2 f_1}{f_2 \sigma_1} \right] \quad \dots (5)$$

The above analysis shows that a system of the type shown in Fig. 2 would appear to behave like a dipolar system because Eq. (4) is a typical equation for a dielectric system consisting of molecules having a relaxation time τ . Rationalizing Eq. (1), we obtain:

$$\epsilon' = \frac{\epsilon'_2}{f_2} \left[1 - \frac{f_1 \epsilon'_2 (\epsilon'_1 f_2 + \epsilon'_2 f_1)}{(\epsilon'_1 f_2 + \epsilon'_2 f_1)^2 + (f_2 \sigma_1 / \omega)^2} \right] \quad \dots (6)$$

which has the following implications:

(a) If the conductivity of the sample material is small ($< 10^{-7} \Omega^{-1} \cdot \text{m}^{-1}$), or measurements are carried out at high frequencies ($> 10^8$ Hz), then Eq. (6) will reduce to:

$$\epsilon' = \frac{\epsilon'_1 \epsilon'_2}{\epsilon'_1 f_2 + \epsilon'_2 f_1} \quad \dots (7)$$

Further, if the volume fraction (f_2) of the air-film is also very small [see Eq. (12)], then the apparent (measured) value of dielectric constant (ϵ') will approach the true value, i.e.

$$\epsilon' \approx \epsilon'_1$$

In other words, for materials having low conductivity, the existence of an imperfect contact will

not seriously affect the measurements even if an uncoated sample is used.

(b) If the material has a large conductivity (say $\sim 10^{-1} \Omega^{-1} \cdot \text{m}^{-1}$), or measurements are carried out at relatively low frequencies (say < 100 Hz), then the factor $(f_2 \sigma_1 / \omega)$ will be much larger than $(\epsilon'_1 f_2 + \epsilon'_2 f_1)$ and therefore,

$$\epsilon' \approx \epsilon'_2 / f_2 \quad \dots (8)$$

Eq. (8) reveals that, under such a circumstance, the apparent value (ϵ') will be not only quite large but could also tend to be independent of ϵ'_1 .

Our results for As-Ge-Te and Se-Ge-Te glasses indicated a large variation in their conductivity ($10^{-10} \Omega^{-1} \cdot \text{m}^{-1}$ to $10^{-1} \Omega^{-1} \cdot \text{m}^{-1}$) when the temperature was raised from 83 to about 340 K. A large change in conductivity was mainly observed above room temperature. Obviously, therefore, the uncoated samples of such materials should show a large variation in ϵ' with increasing temperature. According to Eq. (6), this spurious behaviour should occur when the magnitudes of the factors $(f_2 \sigma_1 / \omega)$ and $(\epsilon'_1 f_2 + \epsilon'_2 f_1)$ become comparable.

In order to make a quantitative analysis, one can solve Eq. (6) by substituting $\epsilon'_2 = \epsilon_0$, $\epsilon'_1 = (12.2 \epsilon_0)^*$ and $f_1 = (1 - f_2)$ into Eqs (6) and (7) which respectively become:

$$f_2 [(\epsilon'_1 / \epsilon_0)^2 - \epsilon'_1 / \epsilon_0] + \epsilon'_1 / \epsilon_0 + f_2 (\sigma_1 / \epsilon_0 \omega)^2 = \epsilon' / \epsilon_0 [1 + f_2^2 (\epsilon'_1 / \epsilon_0 - 1)^2 + 2 f_2 (\epsilon'_1 / \epsilon_0 - 1) + (f_2 \sigma_1 / \epsilon_0 \omega)^2] \quad \dots (9)$$

and

$$f_2 = \frac{\epsilon'_1 / \epsilon_0 - 12.2}{12.2 (\epsilon'_1 / \epsilon_0 - 1)} = \frac{k'_1 - 12.2}{12.2 (k'_1 - 1)} \quad \dots (10)$$

Using our experimental results at 0.5 MHz (Fig. 1), we note that $\epsilon' / \epsilon_0 = 12.2$ at 83 K and $\epsilon' / \epsilon_0 = 20.4$ at 293 K. The values of σ_1 at these temperatures have been found to be $10^{-4} \Omega^{-1} \cdot \text{m}^{-1}$ and $9.93 \times 10^{-4} \Omega^{-1} \cdot \text{m}^{-1}$ respectively. Substitution of these values in Eq. (9) and the use of Eq. (10) after a rearrangement gives a 4th degree equation in k'_1 , i.e.

$$k_1'^4 - 2 k_1'^3 + 1181.4 k_1'^2 - 52262.3 k_1' + 447383.5 = 0 \quad \dots (11)$$

where $k'_1 = \epsilon'_1 / \epsilon_0$

Of the four roots, two are found to be complex and hence meaningless, because k'_1 is the real value of dielectric permittivity. The remaining two roots are 12.2 and 18.13. The former value demands that f_2 should be equal to zero [Eq. (10)] and, therefore, is not of interest for the system under study. We considered

*The reported value of 12.2 of the relative dielectric constant (Ref. 3) corresponds to that at liquid nitrogen temperature (i.e. σ_1 very small) and justifiably, therefore, it is taken to be true value according to criterion (a) mentioned above.

only the second root ($= 18.13$) and calculated the volume fraction (f_2) of the air film by using Eq. (10) which gives:

$$f_2 = 0.0285 \quad \dots (12)$$

These calculated values of k'_1 and f_2 were fed back to Eq. (6) which, after substitution of $\epsilon'_2 = \epsilon_0$ and $f_1 = (1 - f_2)$, becomes:

$$\epsilon'/\epsilon_0 = 35 \left[1 - \frac{1.447}{2.218 + (\sigma_1/\epsilon_0 \omega \times 0.0285)^2} \right] \quad \dots (13)$$

Eq. (13) can be used to predict the behaviour of apparent (measured) dielectric constant at a given frequency (f) if σ_1 is known at different temperatures.

3 Results and Discussion

The validity of the implication of Eq. (6) was checked by estimating the magnitudes of the factors ($f_2 \sigma_1/\omega$) and $(\epsilon'_1 f_2 + \epsilon'_2 f_1)$ which were found to be of the same order around room temperature for all the glasses at the frequency of operation. Quoting the result of $\text{As}_{10}\text{Ge}_{15}\text{Te}_{75}$, for example, we took $\sigma_1 = 10^{-3} \Omega^{-1} \cdot \text{m}^{-1}$ (Ref. 7), $f_2 = 0.02$ [Eq. (12)], $\epsilon'_1 = 12.2\epsilon_0$, $f = \omega/2\pi = 0.5 \text{ MHz}$ and found the values of the factors to be of the same order, i.e. 6.36×10^{-12} and 10.83×10^{-12} respectively at room temperature. Obviously, therefore, one would expect an appreciable dispersion even around room temperature. Fig. 1 confirms this finding.

Similarly, one can predict the apparent value of relaxation time (τ) by using Eq. (5). Substituting $\epsilon'_2 = \epsilon_0$ (air film), $\epsilon'_1 = 12.2\epsilon_0$, $\sigma_1 = 10^{-3} \Omega^{-1} \cdot \text{m}^{-1}$, and $f_2 = 0.02$ in Eq. (5), the value of τ comes out to be $\sim 5 \times 10^{-7} \text{ s}$. Our experimentally reported values of τ (Ref. 2) for these glasses do fall in the range 10^{-6} – 10^{-7} s . Also, according to Eq. (5), $\tau \propto 1/\sigma_1$ and therefore the values of τ should decrease with increasing conductivity. The results, shown in Table 1, do support this observation. One can see that with increasing temperature (i.e. increasing conductivity), the value of τ decreases for almost all the glasses of As-Ge-Te and Se-Ge-Te.

As mentioned earlier, Eq. (13) can be used to find the variation of ϵ' with respect to frequency and temperature for a sample system, having an imperfect contact, if the conductivity of the material is known at the desired temperature. Such calculations have been made for all the alloys of As-Ge-Te and Se-Ge-Te. As an example, results for $\text{As}_{10}\text{Ge}_{15}\text{Te}_{75}$ are shown in Fig. 3. Similar results were obtained for other alloys of As-Ge-Te and Se-Ge-Te. A fair agreement between the calculated and experimental results suggests that such a strong dielectric dispersion, as observed experimentally, is primarily due to imperfect contact. It is difficult to assess the extent of contribution of the material to the observed dispersion. However, some inferences can be drawn by way of the following observations. Fig. 3

Table 1—Experimental Values of τ and α at Different Temperatures for Various Alloys of As-Ge-Te and Se-Ge-Te

Material	Temperature (K)	Macroscopic relaxation time (τ) s	Distribution parameter (α)
$\text{As}_{25}\text{Ge}_{10}\text{Te}_{75}$	283	2.47×10^{-6}	0.29
	293	1.08×10^{-6}	0.34
	303	7.61×10^{-7}	0.41
$\text{As}_5\text{Ge}_{15}\text{Te}_{80}$	283	1.18×10^{-6}	0.35
	293	—	—
	303	2.92×10^{-7}	0.42
$\text{As}_{15}\text{Ge}_{10}\text{Te}_{75}$	283	1.01×10^{-6}	0.34
	293	3.84×10^{-7}	0.42
	303	1.86×10^{-6}	0.53
$\text{As}_5\text{Ge}_{10}\text{Te}_{85}$	283	2.24×10^{-6}	0.23
	293	9.79×10^{-7}	0.31
	303	3.66×10^{-7}	0.39
$\text{Se}_{20}\text{Ge}_{20}\text{Te}_{60}$	333	5.61×10^{-6}	0.37
	343	7.77×10^{-7}	0.46
	353	5.04×10^{-7}	0.52
$\text{Se}_{25}\text{Ge}_{20}\text{Te}_{55}$	333	1.38×10^{-5}	0.50
	343	4.81×10^{-6}	0.57
	353	5.58×10^{-7}	0.64

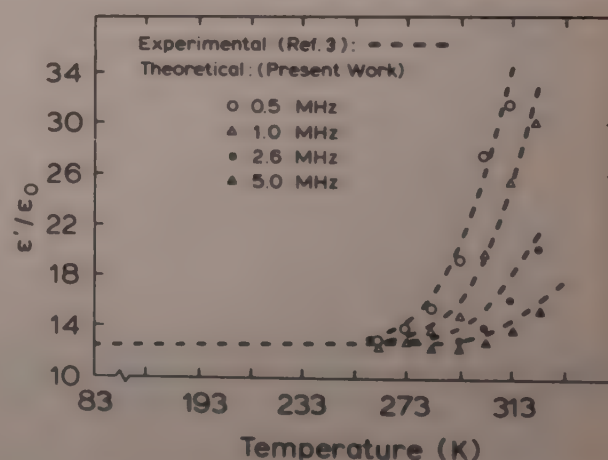


Fig. 3—Variation of dielectric permittivity (ϵ'/ϵ_0) with temperature and frequency for the uncoated sample of semiconducting alloy $\text{As}_{10}\text{Ge}_{15}\text{Te}_{75}$. Dashed curves are the experimental curves, and the data points are the calculated values obtained by using Eq. (13).

reveals that even at room temperature, there is a strong dispersion ($\sim 100\%$). We measured the resistance of our $\text{As}_{10}\text{Ge}_{15}\text{Te}_{75}$ sample at room temperature and found it to be $\sim 50 \text{ k}\Omega$. We, therefore, replaced the sample system of Fig. 2 by a similar (but not exactly equivalent) R-C network shown in Fig. 4(a), which had a metal resistor in place of glassy alloy. The network consisted of a metal oxide resistor of $\sim 50 \text{ k}\Omega$ (in place of As-Ge-Te sample) and polystyrene lossless capacitors in place of C_1 and C_2 . Frequency dependence of the real and imaginary parts of complex capacitance was studied at room temperature for this network and the results (in the form of a Cole-Cole plot) are shown in Fig. 4(b). These results were

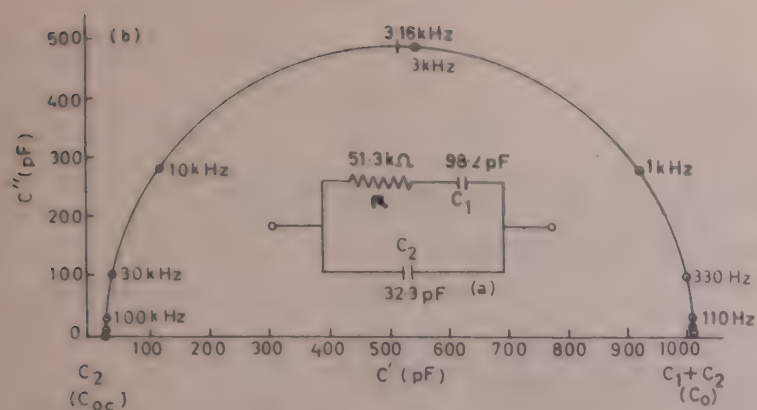


Fig. 4(a)—R-C network with a metal oxide resistor (R) and polystyrene (lossless) capacitors (C_1 and C_2)

Fig. 4(b)—Frequency dependence of the real and imaginary parts of complex capacitance for the R-C network of Fig. 4(a)

provided to the author (KKS) by Prof. N Koizumi of Kyoto University, Japan. The semicircle, thus obtained, indicates the distribution parameter (α) to be zero, whereas we obtained finite values of α for all the samples of As-Ge-Te and Se-Ge-Te (see Table 1). Obviously, it indicates that the two systems [Fig. 2(a) and Fig. 4(a)] are not identical and therefore, the results reported for these glasses¹⁻³ are not exclusively due to the imperfect contact. The material does seem to have some contribution to the observed behaviour.

According to Eq. (6), the discrepancy between the apparent and true behaviour arises only because these glasses have relatively large conductivity. We therefore, selected a similar glassy-system, having low conductivity, by replacing Te with Se. Glassy alloys $\text{As}_x\text{Ge}_y\text{Se}_z$ (with $x = 2$, $z = 3$ and $y = 0.1, 1.0, 5.0$ and 10.0 atomic %) were prepared in this laboratory. The conductivity of these glasses at room temperature was $\sim 10^{-12} \Omega^{-1}\text{-m}^{-1}$. Their dielectric behaviour was studied at room temperature in the same frequency range (0.5-5.0 MHz) by using uncoated samples. All these glasses showed a weak dispersion (10% to 20%) which appears to be their true behaviour because, according to Eq. (6), no errors are likely to be

introduced due to imperfect contact in an uncoated sample if the material has low conductivity.

The above discussion indicates that As-Ge-Te and Se-Ge-Te glasses, in the absence of an imperfect contact, should display a weak dispersion in the rf range. However, the experimenter remains in a dilemma while studying the dielectric parameters of semi-conducting glasses having large conductivity, particularly when the measurements are to be made at higher temperatures and in the kHz-MHz range. A coated sample introduces error due to diffusion of electrode elements into the material, whereas an imperfect contact in uncoated samples leads to an enhanced dispersion. Incidentally, not many dielectric data are reported in the literature for such glasses and, therefore, one cannot make even a comparative study.

Acknowledgement

The authors are grateful to Mr S R Ovshinsky, President, Energy Conversion Devices Inc., USA, for gifting them the semiconducting alloys of As-Ge-Te. One of the authors (KKS) is grateful to the German Academic Exchange Service, Federal Republic of Germany, for providing financial assistance during his recent visit to the Gutenberg University.

References

- 1 Panwar O S, Kumar A, Goyal D R, *et al.*, *J Non-Cryst Solids* (Netherlands), **30** (1978) 37.
- 2 Srivastava K K, Kumar A, Panwar O S & Lakshminarayan K N, *J Non-Cryst Solids* (Netherlands), **33** (1979) 205.
- 3 Panwar O S, Radhakrishna M, Srivastava K K & Lakshminarayan K N, *J Non-Cryst Solids* (Netherlands), **33** (1979) 411.
- 4 Guillaud G, Fornazero J & Maitrot M, *J Appl Phys* (USA), **48** (1977) 3428.
- 5 Tsugane S, Haradome M & Hioki R, *Jpn J Appl Phys* (Japan), **4** (1965) 77.
- 6 Goyal D R, Walker S & Srivastava K K, *Phys Status Solidi a* (Germany), **64** (1981) 351.
- 7 Srivastava K K, Goyal D R, Kumar A, *et al.* *Phys Status Solidi a* (Germany), **41** (1977) 323.

Vibrational Assignment & Calculation of Thermodynamic Properties of *p*-Fluorobenzyl Alcohol

SYED TARIQ*†

Department of Physics, Churachandpur College, Churachandpur 795 128
and

NAUSHAD ALI & P K VERMA

Department of Physics, Aligarh Muslim University, Aligarh 202 001

Received 16 July 1982

Infrared and Raman spectra of *p*-fluorobenzyl alcohol are recorded in the region $4000\text{--}200\text{ cm}^{-1}$. Assignments of all the observed frequencies are proposed and thermodynamic functions calculated for a few temperatures in the range from 100 to 1500 K. The depolarization ratios of the Raman bands suggest a C_s symmetry for the molecule with the CCOH plane parallel to the plane of the phenyl ring.

1 Introduction

Vibrational spectra of benzyl halides¹⁻³ and halogenobenzyl halides^{2,3-5} had been the subject of many investigators. Assignments of the vibrational spectra of benzyl alcohol⁶ and the compounds $p\text{-CNC}_6\text{H}_4\text{CH}_2\text{Z}$, where $\text{Z} = \text{OH}, \text{CN}, \text{Cl}$ or I were also reported⁷. Most of the studies were carried out in order to interpret the vibrational spectra of benzyl metal halides in the regions $1800\text{--}400\text{ cm}^{-1}$ (Ref. 2) and $650\text{--}200\text{ cm}^{-1}$ (Refs 3, 4). Although the vibrational spectra of benzyl compounds were studied by many workers¹⁻⁷ earlier, a full interpretation for the complete spectrum was available only for *p*-fluorobenzyl chloride⁵ and benzyl alcohol⁶. This paper presents the results of an investigation of the compound *p*-fluorobenzyl alcohol (*p*-FBA) in which the aim is to identify the observed frequencies in the infrared and Raman spectra of the compound and to ascertain the approximate symmetry of the molecule with the help of the depolarization ratios of the Raman bands.

2 Experimental Details

The compound *p*-FBA was procured from Chemical Dynamics Corp., New Jersey and was used without further purification. The infrared spectrum of the liquid sample was run several times on PE 580 infrared spectrophotometer in CsI liquid cell of 0.025 mm thickness. The Raman spectrum was excited by the 4880 Å line of a Spectra Physics Model 164 argon ion laser and was recorded on Coderg PHO spectrometer. The spectrum was recorded once with the laser polarized vertically and once with the laser polarized

horizontally. The infrared and laser Raman spectra are reproduced in Figs 1 and 2 respectively.

3 Results and Discussion

It has been reported that the substitution of a hydrogen atom in the methyl group of toluene³ and *p*-halogenotoluene³ by a halogen atom reduces the overall symmetry of the molecule. Depolarization ratios of the Raman bands in the spectra of benzyl halides and *p*-halogenobenzyl halides indicate a C_1 symmetry for the molecules. Similar observations were also made in the case of *p*-fluorobenzyl chloride⁵. However, in the present investigation, the depolarization ratios of the Raman bands in the spectrum of *p*-FBA suggest that the molecule has approximately

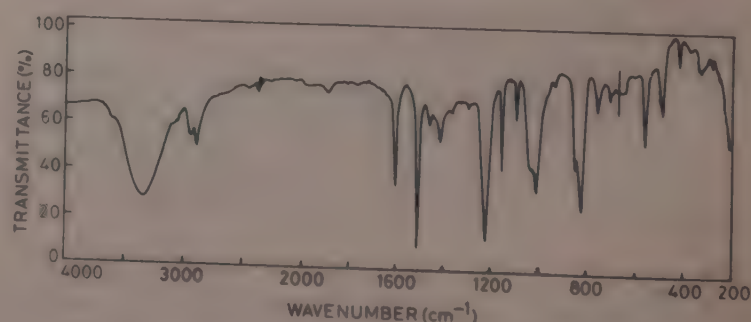


Fig. 1—Infrared spectrum of *p*-fluorobenzyl alcohol

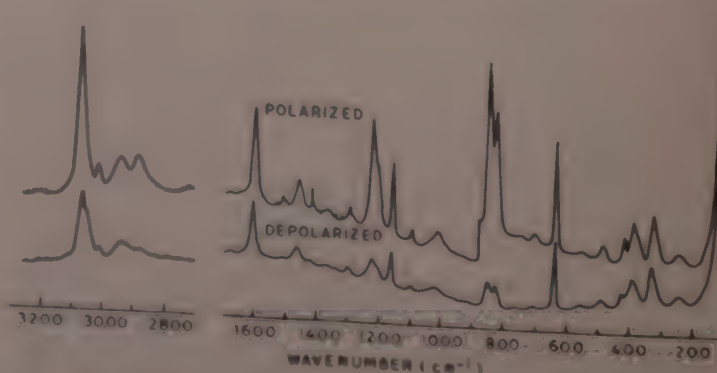


Fig. 2—Raman spectrum of *p*-fluorobenzyl alcohol

†Present address: Department of Physics, Aligarh Muslim University, Aligarh 202 001

C_s symmetry. The molecule may have either of the two conformations: (a) FCCOH plane parallel to the phenyl ring or (b) FCCOH plane perpendicular to the phenyl ring. The fundamental vibrations exclusive of those associated with the substituent divide into $(21a' + 9a'')/(17a' + 13a'')$ in conformation with (a)/(b). In conformation (a), $21a'$ and $9a''$ modes will consist of $11a_1 + 10b_2$ and $6b_1 + 3a_2$ modes respectively of C_{2v} symmetry. In conformation (b), the $17a'$ and $13a''$ modes will comprise $11a_1 + 6b_1$ and $10b_2 + 3a_2$ modes respectively of C_{2v} symmetry. Normal vibrations associated with the substituent comprise $7a' + 5a''$ modes in either of the conformations.

The most appropriate way of interpreting the vibrational frequencies of *p*-FBA is to consider it as a derivative of the corresponding *p*-fluorotoluene. In Table 1 are presented the assignments of *p*-FBA along with the assignments of *p*-fluorotoluene⁸ and *p*-

fluorobenzyl chloride⁵. In making the assignments, guidance has been taken from comparison with the assignments of similar *para*-substituted benzenes^{5,7-10}. The numbering of corresponding modes of vibration of benzene has been made following Wilson¹¹ and the approximate description is that of Whiffen¹². The assignments of the vibrations of the methylene and hydroxyl groups are given in Tables 2 and 3 respectively.

3.1 Vibrations of Aromatic Ring

In *p*-FBA 21 modes $(15a' + 6a'')/(10a' + 11a'')$ are insensitive to substitution. Their assignments follow in a straightforward way from those of other *para*-substituted benzenes. These assignments are self evident and require no further discussion.

The remaining 9 modes $(6a' + 3a'')/(2a' + 7a'')$ are sensitive to the mass and nature of the substituents and are discussed below. It may, however, be noted that these vibrations are strongly coupled; therefore calling them as stretching and bending vibration is only an approximation.

Four of the substituent sensitive modes fall in the a_1 symmetry class. These represent two ring-substituent stretching modes 7a and 13 and two in-plane ring deformation modes 6a and 12. In case of *p*-FBA, the last three vibrations are assigned to the infrared frequencies 1220, 482 and 705 cm^{-1} . The corresponding Raman frequencies 1224, 488 and 708 cm^{-1} are

Table 1—Assignments of Fundamental Frequencies (in cm^{-1}) of *p*-FC₆H₄CH₂Z

Assign- ment	Mode	Z:	H	Cl	OH	
		Wil- son No.	(Ref. 8) IR	(Ref. 5) IR	IR	Raman
a'	a_1 $\nu(\text{CH})$	2	3068	3073	3055 m	3058 sh
	$\nu(\text{CH})$	20a	3065	3045	3020 w	
	$\nu(\text{CC})$	8a	1603	1607	1602 vs	1606 p
	$\nu(\text{CC})$	19a	1513	1512	1508 vs	1515 p
	$\nu(\text{CX})$	13	1224	1225	1220 vs	1224 p
	$\nu(\text{CX})$	7a	1214	1207	(1210)	1208 sh
	$\beta(\text{CH})$	9a	1157	1160	1155 s	1160 p
	$\beta(\text{CH})$	18a	1017	1016	1010 s	1012 p
	Ring	1	842	851	8850 s	852 p
	$\beta(\text{CC})$	12	728	732	705 w	708 p
	$\beta(\text{CC})$	6a	455	474	482 w	488 p
	b_2 $\nu(\text{CH})$	20b	3040	3073	3080 m	3075 p
	$\nu(\text{CH})$	7b	3040	3005	3010 sh	3010 p
	$\nu(\text{CC})$	8b	1592	1602	(1595)	
	$\nu(\text{CC})$	19b	1435	1416	1418 m	1420 p
a''	b_1 $\nu(\text{CH})$	10b	929	912	935 w	940 dp
	$\nu(\text{CH})$	11	817	836	830 sh	
	$\nu(\text{CC})$	4	695	690	690 w	
	$\nu(\text{CC})$	16b	502	524	560 m	560 dp
	$\nu(\text{CX})$	5	342	355	320 w	
	$\nu(\text{CX})$	17b	158	204	250 w	248 dp
	a_2 $\nu(\text{CH})$	17a	956	940	965 sh	960 dp
	$\nu(\text{CH})$	10a	810	830	820 vs	825 p
	$\nu(\text{CC})$	16a	404	421	402 vw	396 p

ν = stretching; β = in-plane bending; γ = out-of-plane bending; s = strong; vs = very strong; m = medium; w = weak; vw = very weak; sh = shoulder; p = polarized; and dp = depolarized. Figures in parenthesis are the expected values.

Table 2—Assignments (in cm^{-1}) of Methylene Group Vibrations of *p*-Fluorobenzyl Alcohol

Assignment	IR	Raman
a'' CH ₂ asym. stretching	2940 m	2940 p
a' CH ₂ sym. stretching	2885 m	2880 p
a' CH ₂ in-plane bending	1460 m	1465 p
a' CH ₂ wagging	1330 vw	
a'' CH ₂ twisting	1280 vw	1280 vw
a'' CH ₂ rocking	760 m	760 dp

For abbreviations see footnote in Table 1

Table 3—Assignment of COH Group Vibrations (in cm^{-1}) of *p*-Fluorobenzyl Alcohol

Assignment	IR	Raman
a' $\nu(\text{OH})_{\text{monomer}}$	3610 w	
a' $\nu(\text{OH})_{\text{associated}}$	3340 vs, vb	
a' $\beta(\text{OH})$	1365 m	1368 p
a' $\nu(\text{C—OH})$	1035 s, b	
a'' $\gamma(\text{OH})$	600 vw	
a' $\beta(\text{C—OH})$	380 w	380 sh
a'' C—CH ₂ OH torsion	(150)	

For abbreviations see footnote in Table 1. The summation bands are 2450: 2×1220 , 2260: $1155 + 1095$, 2062: $1035 + 1020$, 1890: $965 + 935$, 1860: 2×935 , 1820: $1010 + 820$, 1770: $1010 + 760$, 1020: $600 + 420$.

polarized. In substituted benzenes, with a substituent having a carbon atom adjacent to the ring, mode 7a occurs in the region 1200 cm^{-1} (Refs 5, 7-10). In benzyl alcohol, the C—X stretching vibration is placed at 1208 cm^{-1} .⁷ In the infrared spectrum of *p*-FBA, this vibration is probably masked by the strong CF stretching mode 13. However, this vibration is observed in the Raman spectrum at 1208 cm^{-1} .

Two of the substituent-sensitive modes fall in the b_2 symmetry class and should approximate ring-substituent in-plane bending modes 9b and 15. In *p*-fluorobenzene derivatives, mode 9b is predominantly a CF bending vibration and shows a marked constancy at about 420 cm^{-1} (Refs 5, 8-10). Accordingly, the 424 cm^{-1} infrared frequency and the 420 cm^{-1} polarized Raman band are assigned to the CF in-plane bending mode 9b. The second in-plane bending mode 15 is identified with the 330 cm^{-1} infrared frequency with a Raman counterpart at 332 cm^{-1} .

Two of the three b_1 substituent sensitive modes are ring-substituent out-of-plane bending modes 5 and 17b. The former is placed at 320 cm^{-1} in the infrared spectrum of *p*-FBA. Mode 17b is highly sensitive to the substitution in the methyl group. For the substituents $Z = \text{H, Cl and Br}$, this vibration is reported at 158, 204 and 180 cm^{-1} respectively.³ In *p*-FBA, the mode 17b is identified with the infrared frequency 250 cm^{-1} . The corresponding Raman band at 248 cm^{-1} is depolarized. The third substituent sensitive mode 16b of b_1 symmetry class is approximately an out-of-plane ring deformation. In *para*-substituted benzenes, the frequency of this mode appears as a medium intensity band in the region $446\text{ to }552\text{ cm}^{-1}$ (Ref. 13). The medium intensity 560 cm^{-1} infrared band in *p*-FBA has a depolarized Raman counterpart. No satisfactory interpretation exists for it other than as a fundamental and the only obvious assignment available for it is mode 16b.

3.2 Vibrations of Methylene Group

Majority of the methylene group vibrations could be located without ambiguity. The CH_2 asymmetric and symmetric stretchings, the CH_2 in-plane bending and the CH_2 rocking vibrations can be readily identified with the infrared frequencies 2940, 2885, 1460 and 760 cm^{-1} respectively. Their counterparts in the Raman spectrum are 2940, 2880, 1465 and 760 cm^{-1} respectively. While the first three are polarized, the last is depolarized. The difficulty, however arises in the identification of the wagging and twisting vibrations because of their weak absorption. The CH_2 wagging frequency in CH_2X compounds depends on the nature of the substituent X (Ref. 14). In associated primary alcohols^{6,14} it absorbs weakly near 1330 cm^{-1} . The calculated and observed frequencies of CH_2 wagging

mode in *n*-paraffins are 1341 and 1375 cm^{-1} respectively¹⁵. Accordingly, the weak and diffuse infrared band at 1330 cm^{-1} in *p*-FBA is attributed to the CH_2 wagging mode. The CH_2 twisting vibration appears at a little lower frequency than that of the CH_2 wagging vibration¹⁴. The weak absorption at 1280 cm^{-1} in the infrared spectrum of *p*-FBA is identified with the CH_2 twisting mode. These assignments are consistent with those proposed for similar modes in *n*-paraffins¹⁵.

3.3 Vibrations of COH Group

In monomeric species of benzyl alcohol, the OH stretching mode is observed as a weak and sharp band around 3620 cm^{-1} (Ref. 16, 17). The same causes a very intense and broad absorption at 3345 cm^{-1} in the infrared spectrum of associated benzyl alcohol⁶. In the present investigation, the weak and sharp band at 3610 cm^{-1} and the very intense and broad band at 3340 cm^{-1} in the infrared spectrum may be readily assigned to the OH stretching mode of monomeric and associated species respectively. In benzyl alcohol the C—O stretching vibration is reported to occur at 1029 cm^{-1} .⁶ In a previous study, this mode is assigned at 1010 cm^{-1} in benzyl alcohol¹⁸. In the infrared spectrum of *p*-FBA, this mode is attributed to the strong and broad band at 1035 cm^{-1} . In aliphatic primary alcohols in associated state, the OH in-plane bending vibration causes weak and diffuse absorption in the region $1330\text{--}1410\text{ cm}^{-1}$ (Ref. 19, 20). The weak and diffuse infrared band at 1365 cm^{-1} in the spectrum of *p*-FBA is attributed to the OH in-plane bending vibration. The out-of-plane OH bending vibration is placed at 600 cm^{-1} corresponding to the diffuse and weak infrared band. This is in agreement with the assignment proposed for this mode in case of benzyl alcohol⁶. The CH_2OH torsion frequency lies below the region of present investigation. The expected value for this mode is around 150 cm^{-1} .

4 Conclusion

The depolarization ratios of the modes 10a and 16a in a_2 symmetry class and that of $\nu_{\text{asym}}(\text{CH}_2)$ mode favour a C_1 symmetry for the *p*-FBA molecule. But there are five Raman bands which are depolarized. This, therefore, rules out a totally asymmetric stereochemical structure for the molecule.

The two bands at 825 and 396 cm^{-1} in the Raman spectrum of *p*-FBA are polarized. The Raman band at 825 cm^{-1} and its infrared counterpart at 820 cm^{-1} are very strong in intensity. It is therefore taken as a fundamental and assigned to the mode 10a of a_2 symmetry class. The only other possibility is to assign it to a combination band $560 + 248 = 825\text{ A}'$ deriving its intensity from a fundamental. The Raman band at 396

Table 4—The Molal Thermodynamic Properties (in cal/°C) of *p*-FBA in the Ideal-Gas State

<i>T</i> (K)	$-(G^0 - H_0^0)/T$	$(H^0 - H_0^0)/T$	S^0	C_p
100	53.02	8.97	61.99	11.66
200	60.27	12.62	72.89	21.23
300	66.24	17.21	83.45	31.51
400	71.84	21.98	93.82	40.93
500	77.25	26.58	103.83	48.75
600	82.47	30.82	113.29	55.05
700	87.52	34.66	122.18	60.27
800	92.37	38.10	130.47	64.23
900	97.04	41.20	138.24	67.66
1000	101.53	43.99	145.52	70.51
1100	105.84	46.52	152.36	72.93
1200	109.99	48.81	158.80	75.00
1300	113.98	50.89	164.87	76.76
1400	117.82	52.79	170.61	78.28
1500	121.52	54.51	176.03	79.59

cm^{-1} is assigned to the lower component 16a of the degenerate mode e_{1u} (404) of benzene with a very weak counterpart at 402 cm^{-1} in the infrared spectrum. This mode is seldom observed in *para*-substituted benzenes. Therefore the other possible explanation is to assign it to the difference frequency $820-424: 396 \text{ A}'$. Apart from these two and the $\nu_{\text{asym}}(\text{CH}_2)$ mode, the depolarization ratios of all the other observed Raman bands favour a C_s symmetry for the molecule with the CCOH group lying in the plane of the phenyl ring.

5 Thermodynamic Functions

The fundamental frequencies listed in Tables 1-3 were used to calculate the vibrational contributions to the thermodynamic functions. To compute the rotational contributions, the following dimensions were used: C—C = 1.397 \AA ; C—H = 1.084 \AA ; C—F = 1.35 \AA ; C—O = 1.48 \AA ; O—H = 0.95 \AA ; C—CH₂OH = 1.50 \AA ; $\angle\text{COH} = 108.9^\circ$. Tetrahedral values were used for H—C—H, C—C—O and C—C—H angles, all other angles were taken as 120° . For this model, the products of the three moments of inertia was found to be $17.16 \times 10^{-113} \text{ g}^3 \times \text{cm}^6$. The

symmetry numbers are 1 for overall rotation. The total contributions to the thermodynamic functions for 1 mol of the ideal gas at 1 atm are summarized in Table 4. The computation for the vibrational contribution was done on VAX 11/780 computer.

Acknowledgement

The authors are grateful to Prof. M Z Rahman Khan, Chairman, Physics Department for the keen interest taken by him during the course of this work. We are also grateful to Prof. Ben van der Veken of Laboratorium voor Anorganische Scheikunde, Antwerpen, Belgium for recording the Raman spectrum. Financial assistance received by one of the authors (ST) from the University Grants Commission, New Delhi, is gratefully acknowledged.

References

- 1 Mannion J J & Wang T S, *Spectrochim Acta (GB)*, **20** (1964) 45.
- 2 Cattanch C J & Mooney E F, *Spectrochim Acta Vol A (GB)*, **24** (1968) 407.
- 3 Verdonck L & Van der Kelen G P, *Spectrochim Acta Vol A (GB)*, **28** (1972) 51, 55.
- 4 Verdonck L & Van der Kelen G P, *Spectrochim Acta Vol A (GB)*, **29** (1973) 813.
- 5 Seth-Paul W A & Shino H, *Spectrochim Acta Vol A (GB)*, **31** (1975) 1605.
- 6 Varsanyi G, *Assignments for vibrational spectra of 700 benzene derivatives*, Vol 1 (Wiley, New York) 1974.
- 7 Wilson H W & Bloor J E, *Spectrochim Acta (GB)*, **21** (1965) 45.
- 8 Green J H S, *Spectrochim Acta Vol A (GB)*, **26** (1970) 1503.
- 9 Jakobsen R J, *Spectrochim Acta (GB)*, **21** (1965) 433.
- 10 Green J H S & Harrison D J, *Spectrochim Acta Vol A (GB)*, **32** (1976) 1265, 1279.
- 11 Wilson E B, *Phys Rev (USA)*, **45** (1934) 706.
- 12 Whiffen D H, *J Chem Soc (GB)*, (1956) 1350.
- 13 Jakobsen R J & Bentley F F, *Appl Spectrosc (USA)*, **18** (1964) 88.
- 14 Colthup N B, Daly L H & Wilberley S W, *Introduction to infrared and Raman spectroscopy* (Academic Press, New York) 1964.
- 15 Gordon M B, *J Chem Phys (USA)*, **19** (1951) 345.
- 16 Anet F A L & Bavin P M G, *Can J Chem (Canada)*, **34** (1956) 1757.
- 17 Bellamy L J & Pace R J, *Spectrochim Acta Vol A (GB)*, **27** (1971) 705.
- 18 Zeiss H H & Tsulsui M, *J Am Chem Soc (USA)*, **75** (1953) 897.
- 19 Stuart A V & Sutherland G B B M, *J Chem Phys (USA)*, **24** (1956) 559.
- 20 Krimm S, Liang C Y & Sutherland G B B M, *J Chem Phys (USA)*, **25** (1956) 778.

Calculation of Judd-Ofelt Intensity Parameters (T_λ) in Some Nd(III) Complexes by Using the Statistical Method

G K JOSHI*

Department of Chemistry, Government PG College, Nagaur (Raj) 341 001

Received 13 September 1982

The statistical method for calculating T_λ -parameters has been described in detail. The symmetry of the complexes has been discussed on the basis of T_4/T_6 ratio. A relation $P \propto \nu T_6$ (or $P \propto \nu T_4$) has been suggested in comparison to $P \propto \nu b^2$ for hypersensitive transitions observed in the lanthanide complexes. The applicability of the theory as well as the statistical method used for calculating electronic spectral parameters (T_λ , F_K and ζ_{4f}) has been established from rms deviation point of view. The statistical method suggested in the paper is an alternative to a computer programming method.

1 Introduction

Judd and Ofelt have derived an equation for the oscillator strength (P) of a transition between a ground state ($f^n\psi_J$) and an excited state ($f^n\psi'_J$), of the lanthanide ion in solution given as¹:

$$P = \sum_{\lambda=2,4,6} T_\lambda \nu (f^n\psi_J \| U^{(\lambda)} \| f^n\psi'_J)^2 \quad \dots(1)$$

where the unit tensor operators [$U^{(\lambda)}$] connect the initial and final states via T_λ ($\lambda = 2, 4, 6$) parameters. The oscillator strength (P) is the probability of an electronic transition and can be given as²:

$$P = 4.6 \times 10^{-9} \times \epsilon_m \times \Delta\nu_{1/2} \quad \dots(2)$$

where ϵ_m is the molar absorptivity of the peak maximum and $\Delta\nu_{1/2}$ is the half-intensity band width, i.e. the width at $\frac{1}{2}\epsilon_{\max}$. For an allowed transition, P equals one. Since the $f \leftrightarrow f$ transitions are mostly induced electric dipole transitions, the value of P is of the order of 10^{-6} , i.e. $P \ll 1$. The value of the oscillator strength due to magnetic-dipole (P_{md}) or electric-quadrupole (P_{eq}) is still lesser and it is of the order of 10^{-8} or 10^{-10} respectively. The selection rules³ for these transitions are $\Delta J \leq 1$ and $\Delta J \leq 2$ in Russell-Saunders approximation. In $f \leftrightarrow f$ spectra, most of the transitions have $\Delta J \geq 2$. In Judd-Ofelt parameters (T_λ) we have $\Delta J \leq \lambda$; i.e. for T_2 , T_4 and T_6 , we have $\Delta J \leq 2$, $\Delta J \leq 4$ and $\Delta J \leq 6$ respectively. Thus the T_6 parameter is best determined while T_2 is poorly determined. Sometimes the value of T_2 comes to be negative which is meaningless because by definition $T_\lambda \geq 0$.

The transitions considered to be potentially hypersensitive or pseudo-hypersensitive from the value of oscillator strength (P) have been found to exhibit approximately a linear relationship⁴ between P and νb^2 where ν is the frequency of the transition and b is the bonding parameter. Thus it has been suggested that the relation $P \propto \nu T_\lambda$ or $P \propto T_\lambda$ should also follow

approximately for such transitions when the Judd-Ofelt relation [Eq. (1)] is closely examined.

It has also been observed that the ratio T_4/T_6 is found to be nearly constant^{5,6} for the complexes having the same symmetry. Thus the Judd-Ofelt parameters (T_λ) are the characteristic intensity parameters for the intra- f^n -transitions observed in the lanthanide complexes. Therefore, it has been thought desirable to use the statistical method for computing T_λ -parameters (which is an alternative to a computer programming method). Previously, the statistical methods for computing electronic spectral parameters (Slater-Condon and Racah interelectronic repulsion and Lande spin-orbit interaction parameters, etc.) resulting from intra- f^n -transitions have been reported by earlier workers^{7,8}. The attempts to calculate T_λ -parameters by using the statistical methods are rare because most of the work on the intensity of lanthanide $f \leftrightarrow f$ spectra has been done after the publication of the theory of lanthanide intensity by Judd⁹ and Ofelt¹⁰ independently in 1962.

In the present paper, the T_λ -parameters for the two Nd(III) complexes with vanillin Schiff bases derived from *ortho*-phenylenediamine and from *ortho*-aminobenzenethiol have been studied.

2 Experimental Procedure

2.1 Synthesis

The complexes have been synthesized by the method described by Ansari and Ahniad¹¹ by refluxing for about 6 hr, a mixture of ethanolic solution of $\text{NdCl}_3 \cdot 6\text{H}_2\text{O}$ and the Schiff-base ligand prepared from vanillin and *ortho*-phenylenediamine (or *ortho*-aminobenzenethiol) in the molar ratio 1:1. However, the ligands V.o-PhDA (vanillin-*ortho*-phenylenediamine) and V.o-ABT (vanillin-*ortho*-aminobenzenethiol) have been synthesized by condensation reaction in ethanol between vanillin and the respective

amine in the molar ratio 2:1 and 1:1 respectively. In the reaction mixture, the precipitation occurs with a change in colour from light yellow to dark brown. AnalaR grade chemicals were used. Both the complexes were found soluble in dimethylsulfoxide (DMSO).

2.2 Infrared Spectra

The bands appearing near 3300 cm^{-1} (lattice water), 1635 cm^{-1} ($\nu_{\text{C}=\text{N}}$), 1445 cm^{-1} ($\nu_{\text{phenolic C-O}}$), 1005 cm^{-1} (coordinated water) and 780 cm^{-1} ($\nu_{\text{metal-nitrogen}}$) in the complexes suggest⁶ that the ligands are coordinated to Nd(III) ion through oxygen of the phenolic group and nitrogen of the imine group. The water is present in the form of lattice water as well as in the form of coordinated water. However, the bands showing $\nu_{\text{metal-sulphur}}$ and $\nu_{\text{metal-chlorine}}$ could not be recorded as the same fall beyond the range of the instrument.

The analytical and infrared data propose the chemical formula for the complexes as: $\text{Nd(V.SB)Cl} \cdot 3\text{H}_2\text{O}$, where V.SB is a vanillin Schiff base ligand.

2.3 Electronic Spectra

The absorption spectra were measured on Carl-Zeiss VSU-2 spectrophotometer in the region 360-1000 nm in a mixed solvent, DMSO and alcohol (3:1).

3 Method of Calculation

In the calculation of T_λ -parameters, the statistical method known as partial and multiple regression method¹² has been used. The purpose of the partial regression method is to obtain a measure of the relation between two variables when the other variable is constant. The equations for the partial and multiple regression have the following form:

$$Y = a + b_1 X_1 + b_2 X_2 + b_3 X_3 + \dots + b_p X_p \quad \dots (3)$$

where there are p independent variables and the regression coefficients b_1, b_2, b_3, \dots , etc are referred to as partial regression coefficients.

The observed oscillator strength (P_{obs}) of the energy transition can be expressed in terms of T_2, T_4 and T_6 parameters as follows:

$$P_{\text{obs}} = T_2 \nu [U^{(2)}]^2 + T_4 \nu [U^{(4)}]^2 + T_6 \nu [U^{(6)}]^2 \quad \dots (4)$$

The values of $[U^{(2)}]^2, [U^{(4)}]^2$ and $[U^{(6)}]^2$ have been taken as used by Carnall *et al.*¹ The eight bands in the present Nd(III) complexes have been considered. These have been assigned the energy levels as $^4F_{3/2}, ^4F_{5/2}, ^4F_{7/2}, ^4F_{9/2}, ^4G_{5/2}, ^4G_{7/2}, ^2G_{9/2}$ and $^4G_{9/2}$. From the observed oscillator strength for the said eight bands, the eight equations of form as given in Eq. (3) have been obtained. Here we have following:

$$Y = \frac{P_{\text{obs}}}{\nu}, \quad a = 0, \quad b_1 = T_2, \quad b_2 = T_4, \quad b_3 = T_6$$

$$X_1 = [U^{(2)}]^2, \quad X_2 = [U^{(4)}]^2 \quad \text{and} \quad X_3 = [U^{(6)}]^2$$

Now three main steps are involved further to compute the values T_2, T_4 and T_6 in terms of b_1, b_2 and b_3 .

Step I—From the eight equations so obtained, the values of $a_{11}, a_{22}, a_{33}, a_{21}, a_{31}$ and a_{32} have been calculated from the relations given as follows:

$$a_{11} = \sum x_1^2, \quad a_{22} = \sum x_2^2, \quad a_{33} = \sum x_3^2, \quad a_{21} = \sum x_2 x_1, \\ a_{31} = \sum x_3 x_1 \quad \text{and} \quad a_{32} = \sum x_3 x_2$$

$$\text{where} \quad \sum x_1^2 = \sum X_1^2 - \frac{(\sum X_1)^2}{N}$$

(Similarly relations involving $\sum x_2^2$ and $\sum x_3^2$ can also be given), and

$$\sum x_2 x_1 = \sum X_2 X_1 - \frac{\sum X_2 \times \sum X_1}{N}$$

(Similarly relations involving $\sum x_3 x_1$ and $\sum x_3 x_2$ can also be given)

Here the value of N is eight.

Step II—From the values of a_{11}, a_{22}, \dots , etc. the values of c_{11}, c_{12}, \dots , etc have been obtained by following the instructions given in the literature¹² and using the matrix given as Table 1.

The values obtained for c_{11}, c_{12}, \dots , etc. can be however, checked by the following relation:

$$c_{11} \times a_{11} + c_{12} \times a_{21} + c_{13} \times a_{31} = 1.00 \quad \dots (5)$$

Step III—From the values of c_{11}, c_{12}, \dots , etc. the values a, b_1, b_2 and b_3 can be computed by using the relations given as follows:

$$b_1 = c_{11} \times \sum x_1 y + c_{12} \times \sum x_2 y + c_{13} \times \sum x_3 y \\ b_2 = c_{12} \times \sum x_1 y + c_{22} \times \sum x_2 y + c_{23} \times \sum x_3 y \\ b_3 = c_{13} \times \sum x_1 y + c_{23} \times \sum x_2 y + c_{33} \times \sum x_3 y \\ a = \bar{Y} - b_1 \bar{X}_1 - b_2 \bar{X}_2 - b_3 \bar{X}_3 \quad \dots (6)$$

Here we have

$$\sum x_1 y = \sum X_1 Y - \frac{\sum X_1 \times \sum Y}{N}$$

(Similarly values of $\sum x_2 y$ and $\sum x_3 y$ can be given) and

$$\bar{Y} = \sum Y / N$$

(Similarly \bar{X}_1, \bar{X}_2 and \bar{X}_3 can be given)

Table 1—Matrix for Calculating c_{ij} from a_{ij}

Line	Abbreviated solution					
1	a_{11}	a_{21}	a_{31}	1.0	0	0
2		a_{22}	a_{32}	0	1.0	0
3			a_{33}	0	0	1.0
Lines 4-9				c_{11}	c_{12}	c_{13}
10					c_{22}	c_{23}
11						c_{33}
12						

In the present calculation a is zero, but it can be obtained if there are four parametric calculations instead of three variables. The values of c_{11} , c_{12} ..., etc have been computed for the said eight bands and are given as follows:

$$c_{11} = 3.895, \quad c_{12} = -6.56, \quad c_{13} = 1.55$$

$$c_{22} = 18.21, \quad c_{23} = -2.44 \quad \text{and} \quad c_{33} = 5.30$$

From the values of c_{11} , c_{12} ..., etc given here the T_λ -parameters can be computed for any Nd(III) complex where only the said eight bands are considered. If certain other bands are observed, then fresh calculations for c_{11} , c_{12} ..., etc will have to be done.

4 Results and Discussion

The Judd-Ofelt intensity parameters (T_2 , T_4 and T_6) are reported in Table 2. The other electronic spectral parameters^{6,13,15} [Slater-Condon (F_k) and Lande (ζ_{4f})] have also been reported in same table. The later parameters are interelectronic repulsion and spin-orbit interaction parameters. These have also been computed by using the statistical method given earlier by Misra and Joshi⁸. The values of energy parameters F_k and ζ_{4f} are reduced as compared to the values of these parameter for Nd(III) free ion⁶ showing the expansion of $4f$ -orbital in the complex formation.

The values of T_4/T_6 for the present complexes are 1.009 and 4.922. This shows that these complexes do not have a similar symmetry. This reflects that Nd(III) ion

may exhibit different coordination numbers in these complexes. Since a lanthanide ion may have a coordination number ranging from 6 to 9, here Nd(III) ion in the V.o-ABT complex may exhibit lesser coordination number in comparison to the V.o-PhDA complex. The V.o-ABT ligand is behaving as a tridentate ligand while the ligand V.o-PhDA is behaving as a tetradentate ligand. The value of T_4/T_6 for the complex Nd.v.o-PhDA is nearly the same as have been reported earlier for the similar complexes by Joshi *et al.*⁶

The transition $^4I_{9/2} \rightarrow ^4G_{5/2}$ behaves as a hyper-sensitive transition and it follows the relation $P \propto \nu T_6$ (or $P \propto \nu T_4$) in the present complexes (Table 1).

The value of rms deviation (σ) lies in between 0.21×10^{-6} to 0.84×10^{-6} for the observed and calculated value of oscillator strengths for the various bands. This shows that the applicability of the both the Judd-Ofelt relation and the statistical method used here is quite established in the present case. This is because, the value of P_{calc} is again computed from the values of T_2 , T_4 and T_6 which are obtained from the Judd-Ofelt relation by using the statistical method. The statistical method used for computing F_k and ζ_{4f} parameters have also yielded the good results (rms deviation lies in between ± 60.4 to $\pm 53.2 \text{ cm}^{-1}$).

In the present calculation of the T_λ -parameters, the two levels $^2P_{1/2}$ and $^4G_{11/2}$ have not been considered as these levels have negligible values¹ for $[U^{(A)}]^2$ elements.

Table 2—Computed Values of Oscillator Strength (P), Judd-Ofelt Intensity Parameters (T_2 , T_4 , T_6) and Other Electronic Spectral Parameters (F_2 , F_4 , F_6 and ζ_{4f} in cm^{-1}) for the Nd(III) Complexes

Level and parameter	Nd. V. o-PhDA				Nd. V. o-ABT			
	E_{expt} cm^{-1}	E_{calc} cm^{-1}	$P_{\text{expt}} \times 10^6$	$P_{\text{calc}} \times 10^6$	E_{expt} cm^{-1}	E_{calc} cm^{-1}	$P_{\text{expt}} \times 10^6$	$P_{\text{calc}} \times 10^6$
$^2P_{1/2}$	23148	23135	0.95	0.83	23137	23131	1.97	0.84
$^4G_{11/2}$	21645	21502	0.29	0.27	21645	21500	0.48	0.14
$^4G_{9/2}$	21254	21217	1.99	2.09	21097	21098	1.36	1.42
$^2G_{9/2}$	19531	19557	0.67	0.53	19550	19524	0.59	0.32
$^4G_{7/2}$	19157	19220	4.87	4.52	19179	19177	2.14	3.38
$^4G_{5/2}$	17241	17218	17.87	17.82	17265	17257	11.88	11.33
$^4F_{9/2}$	14641	14730	0.81	0.52	14663	14704	1.06	0.25
$^4F_{7/2}$	13298	13267	5.87	5.79	13263	14280	2.49	1.63
$^4F_{5/2}$	12422	12443	7.72	7.35	12392	12459	3.48	3.75
$^4F_{3/2}$	11429	11425	2.85	3.05	11455	11452	4.12	2.64
rms dev (σ)	± 60.4		$\pm 0.21 \times 10^{-6}$		± 53.2		$\pm 0.84 \times 10^{-6}$	

$T_2 \times 10^{10}$	6.88	2.88
$T_4 \times 10^{10}$	9.39	9.55
$T_6 \times 10^{10}$	9.31	1.94
T_4/T_6	1.008	4.922
F_2	327.826	330.500
F_4	52.057	59.917
F_6	5.240	5.270
ζ_{4f}	863.87	858.85

Acknowledgement

The author is highly thankful to Shri B L Gajja and Dr B R Joshi, Drought Prone Area Project, Jodhpur for a useful discussion about the statistical method used in the paper. The author also thanks the University Grants Commission, New Delhi, for awarding him a Teacher Fellowship. He is also grateful to Prof. R C Kapoor and Dr Sudhindra N Misra, Department of Chemistry, University of Jodhpur, Jodhpur, for their valuable guidance and interest in the work. The author cannot forget to thank his friend Shri I R Joshi, Scientist, Defence Laboratory, Jodhpur, for inspiration and help throughout the work.

References

- 1 Carnall W T, Fields P R & Wybourne B G, *J Chem Phys (USA)*, **42** (1965) 3797.
- 2 Drago R S, *Physical methods in inorganic chemistry* (Affiliated East-West Press Pvt Ltd, New Delhi) 1968, Ch. 6, 147.
- 3 Mehta P C & Tandon S P, *J Chem Phys (USA)*, **53** (1970) 414.
- 4 Henrie D E & Choppin G R, *J Chem Phys (USA)*, **49** (1968) 477.
- 5 Surana S S L, Mathur R C & Tandon S P, *Spectrosc Lett (USA)*, **11**(6) (1978) 389.
- 6 Joshi G K, Bhutra M P & Misra Sudhindra N, *J Inorg Nucl Chem (GB)*, **43** (1981) 525.
- 7 Peacock R D, *Structure and bonding* (Springer-Verlag, New York) 1975, 22, 88.
- 8 Misra Sudhindra N & Joshi G K, *Indian J Pure & Appl Phys*, **19** (1981) 279.
- 9 Judd B R, *Phys Rev (USA)*, **127** (1962) 750.
- 10 Ofelt G S, *J Chem Phys (USA)*, **37** (1962) 511.
- 11 Anasari M S & Ahmad N A, *J Inorg Nucl Chem (GB)*, **38** (1976) 1232.
- 12 Goulden C H, *Method of statistical analysis* (Asia Publishing House, Bombay) 1964, Ch. 8, 134.
- 13 Surana S S L, Megh Singh & Misra Sudhindra N, *J Inorg Nucl Chem (GB)*, **42** (1980) 61.
- 14 Tandon S P & Govil R C, *Z Naturf (Germany)*, **26a** (1971), Heft 8, 1357.
- 15 Misra Sudhindra N, Joshi G K & Megh Singh, *J Inorg Nucl Chem (GB)*, **43** (1981) 206.

Dipole Moment Study of OH—O Bond in Organic Complexes

AMAR SINGH, RAJNI MISRA, J P SHUKLA & M C SAXENA*

Physics Department, Lucknow University, Lucknow

Received 3 July 1982; revised received 16 November 1982

The dipole moment and the apparent equilibrium constant (K_{app}) of the complexes of ethyl acetate, butyl acetate and benzyl acetate with phenol and *n*-butyl alcohol in carbon tetrachloride at 30°C have been calculated using Few and Smith method [*J Chem Phys (GB)*, (1949) 2781.]. The dipole moment values were also calculated using Huyskens's method for different concentrations of acids and bases. The enhancement of the dipole moment values confirms the hydrogen bonding between all the acetate molecules and phenol and *n*-butyl alcohol.

1 Introduction

The formation of hydrogen bond leads to an increased polarity of the bond A—H (proton donor), and hence to a larger dielectric constant and dipole moment. Dielectric investigations of interacting solutes in an inert solvent provide valuable information regarding the formation of molecular complex in solution. Huyskens and his collaborators¹ have developed methods to determine the stereo-chemistry of hydrogen bonded complexes from the dielectric measurements of solutions of proton donor plus proton acceptor in an inert solvent. The dipole moment of the complex is a function of the relative strengths of the acid and base and can be calculated. The enhancement of the dipole moment ($\Delta\mu$) over the sum of the dipole moments of the interacting components corresponds to charge redistribution along the A—H—B bond. In this paper, we are reporting the dipole moment study of 1:1 complex of acetates, namely ethyl acetate, butyl acetate and benzyl acetate with phenol and *n*-butyl alcohol in carbon tetrachloride at 30°C. The apparent equilibrium constant, molar polarization and dipole moment of the complex were calculated using the Few and Smith² method. For comparative study and for the study of the variation of dipole moment values with the concentration of acid and base in the solution, these were also computed using the method of Debecker and Huyskens³.

2 Theory

Few and Smith² suggested that the induced polarization (ΔP) with association of two interacting polar solute molecules of proton donor (A) and proton acceptor (B) in an inert solvent (S), due to hydrogen bonding can be given as:

$$\Delta P = P_{(AB)S} - [P_{(A)S} + P_{(B)S}] \quad \dots (1)$$

where $P_{(AB)S}$ is the molar polarization of the mixture

of A and B in an inert solvent (S) at infinite dilution and $P_{(A)S}$ and $P_{(B)S}$ are the molar polarizations of the solutes A and B.

The dipole moment of the complex can be calculated as:

$$\mu_{ab} = 0.12812 [(P_{(AB)S} - R_{(D\infty)}) \cdot T]^{1/2} \quad \dots (2)$$

where $R_{(D\infty)}$ is the molar refraction of the 1:1 complex. $P_{(AB)S}$ can be obtained with the help of Eq. (1), if ΔP is known because the other factors $P_{(A)S}$ and $P_{(B)S}$ can be observed experimentally. In order to calculate ΔP , the method of Cleverdon *et al.*⁴ was used which relates the induced polarization (ΔP) with the apparent equilibrium constant (K_{app}) and the molar polarization of the proton donor A in the BS mixture solvent ($P_{(A)BS}$) as:

$$\frac{\Delta P}{P_{(A)BS} - P_{(A)S}} = 1 + \frac{M_B}{K_{app} W'_B d_{BS}} \quad \dots (3)$$

where M_B is the molecular weight of the proton acceptor, d_{BS} , the density of the solvent mixture BS and $W'_B = W_B / (W_B + W_S)$; W_B and W_S being the weight factors of B and the solvent S.

Eq. (3) may be written as:

$$\frac{1}{P_{(A)BS} - P_{(A)S}} = \frac{1}{\Delta P} + \frac{1}{\Delta P K_{app}} \frac{M_B}{W'_B d_{BS}} \quad \dots (4)$$

The plot of $\frac{1}{P_{(A)BS} - P_{(A)S}}$ and $\frac{M_B}{W'_B d_{BS}}$ is a straight line with intercept $1/\Delta P$ and slope $1/\Delta P K_{app}$. Using the values of ΔP and Eqs (1) and (2), the dipole moments of the complexes were calculated.

The mean square value of the dipole moment was also calculated using the method of Debecker and Huyskens³, as:

$$\mu_{exp}^2 = \frac{9kT}{4\pi N} \left[\frac{X_1 - 1}{X_2(2 + 1)} - 3 \left\{ \frac{X_1 - 1}{1 - 2X_1 + X_2} + \left(1 - \frac{X_1 - 1}{1 - 2X_1 + X_2} \right) \left(\frac{\eta_{21}^2 - 1}{\eta_{21}^2 + 1} \right) \right\} \right] \quad \dots (5)$$

where V is the molar volume of the solution and V_1 that of the solvent; ϵ and ϵ_1 are the dielectric constants of the solution and solvent respectively; X_1 the mole fraction of the solvent; $X_{23} = 1 - X_1$ the mole fraction of the interacting polar components; and η_{23} is the refractive index of the polar components in the solution.

The dipole moment of the 1:1 complexed species, in the concentration range where $C_B \gg C_A$ and most of the molecules predominantly exist as 1:1 complex, was calculated using Eq. (6)

$$\mu_{\xi}^2 = \frac{\mu_{\text{exp}}^2(C_A + C_B) - \mu_b^2(C_B - C_A)}{C_A} \quad \dots (6)$$

where C_B and C_A are the initial concentrations of proton acceptor and proton donor molecules in the solution and μ_{ξ} is the dipole moment of the complex.

The change in dipole moment $\Delta\mu$ was calculated using the relation

$$\Delta\mu = \mu_{ab} - \mu_a - \mu_b \quad \dots (7)$$

where μ_{ab} is the dipole moment of the complex and μ_a and μ_b are the dipole moments of proton donor and proton acceptor solute molecules, respectively.

3 Experimental Details

The dielectric constant ϵ of the solution and of solvent (ϵ_1) at static frequency were measured using a

Toshniwal RL09 dipole meter and, the refractive index using an Abbe's refractometer. The cell temperature was maintained at $30 \pm 0.2^\circ\text{C}$ by circulating water through the glass jacket of the cell.

The chemicals used were obtained from BDH Ltd. Poole, England and High Purity Chemicals Pvt Ltd. New Delhi. The physical parameters of all the chemicals were checked against their literature values.

4 Results and Discussion

The limiting values of the molecular polarization, the density, d_{BS} , of solvent mixture and concentrations of acids and bases for all the systems are given in Table 1. The variation of dipole moment values (μ_{exp} and μ_{ξ}), calculated using Huyskens method³, with $(C_B - C_A)$ is reported in Table 2. Table 3 includes the dipole moment, apparent equilibrium constant (K_{app}) and induced polarization (ΔP) for all complexed species calculated using the Few and Smith² method.

The dipole moment of the ethyl acetate + phenol system obtained using Few and Smith² method was found to be 3.4 D. It may be observed from Table 2, that μ_{ξ} values vary irregularly with $C_B - C_A$ values. The dipole moments μ_{ξ} represent here the dipole moments of solute (proton donor, proton acceptor and 1:1 complex) molecules in the solution. On increasing the concentration of proton acceptor C_B , keeping C_A

Table 1—Limiting Values of Molecular Polarization

	C_B mol/l	C_A mol/l	d_{BS}	$M_B \times 10^3$ $W'_B d_{BS}$	10 $P_{(A\infty)BS} - P_{(A\infty)S}$
Ethyl acetate + Phenol	0.93	0.11-0.86	1.518	1.086	1.160
	1.70	0.13-0.78	1.445	0.601	0.699
	2.35	0.21-1.27	1.434	0.424	0.679
	2.96	0.17-1.24	1.378	0.347	0.609
Butyl acetate + Phenol	0.69	0.25-1.13	1.507	1.480	1.810
	1.26	0.23-1.39	1.455	0.804	0.963
	1.74	0.18-1.11	1.410	0.588	0.721
	2.19	0.17-1.02	1.380	0.466	0.570
Benzyl acetate + Phenol	0.64	0.15-0.76	1.535	1.576	1.460
	1.17	0.13-1.11	1.479	0.757	0.739
	1.61	0.17-1.05	1.445	0.627	0.589
	2.04	0.16-1.08	1.415	0.506	0.515
Ethyl acetate + <i>n</i> -butyl alcohol	0.93	0.19-1.41	1.503	1.097	1.960
	1.70	0.20-1.81	1.443	0.602	1.053
	2.35	0.18-1.53	1.399	0.435	0.741
	2.96	0.26-1.47	1.352	0.360	0.618
Butyl acetate + <i>n</i> -Butyl alcohol	0.69	0.14-1.31	1.539	1.440	1.660
	1.26	0.31-1.53	1.468	0.797	1.005
	1.74	0.30-1.38	1.448	0.565	0.699
	2.19	0.24-1.45	1.371	0.469	0.612
Benzyl acetate + <i>n</i> -Butyl alcohol	0.64	0.31-1.09	1.514	1.598	1.932
	1.17	0.18-1.73	1.484	0.866	1.226
	1.61	0.34-1.74	1.442	0.629	0.797
	2.04	0.26-1.64	1.416	0.507	0.602

Table 2—Dipole Moment Values Calculated using Huyskens Method

Ethyl acetate + phenol			Butyl acetate + phenol			Benzyl acetate + phenol		
$C_B - C_A$ mol/l	μ_{exp} D	μ_z D	$C_B - C_A$ mol/l	μ_{exp} D	μ_z D	$C_B - C_A$ mol/l	μ_{exp} D	μ_z D
0.17	2.12	3.03	0.07	2.45	3.50	0.03	2.46	3.50
0.44	1.96	2.12	0.25	2.41	3.58	0.06	2.49	3.54
0.58	2.25	2.76	0.52	1.98	3.04	0.25	2.42	3.65
0.61	2.37	3.51	0.92	2.35	3.76	0.38	2.46	3.66
0.77	2.24	3.46	1.08	2.34	3.64	0.55	2.40	3.69
0.89	2.29	3.46	1.12	2.31	3.95	0.56	2.33	3.45
1.03	2.22	3.88	1.30	2.17	3.93	0.70	2.39	3.64
1.17	2.37	3.87	1.49	2.30	3.84	0.79	2.36	3.94
1.23	2.38	3.71	1.67	2.26	3.98	0.93	2.31	3.64
1.30	2.22	3.64	1.71	2.30	3.74	1.36	2.28	3.76
1.43	2.32	3.70	1.98	2.23	3.78			
1.73	2.22	3.75						
0.44	2.06	2.99	0.08	2.08	2.95	0.05	2.02	2.87
0.48	2.05	3.19	3.30	2.14	3.07	0.23	2.04	2.90
0.74	2.05	3.85	0.36	2.20	3.16	0.32	2.00	2.87
0.82	2.06	3.04	0.53	2.14	3.11	0.33	2.01	2.95
0.87	2.20	3.42	0.57	2.17	3.15	0.37	2.07	2.96
1.13	1.96	3.11	0.74	2.09	3.63	0.47	1.94	2.78
1.39	2.00	3.11	0.79	2.13	3.12	0.62	2.02	2.93
1.44	2.06	3.28	0.95	2.18	3.53	0.68	1.96	2.81
1.49	2.05	3.13	1.02	2.08	3.03	0.97	1.99	2.97
1.76	1.99	3.35	1.27	2.06	3.03	0.99	2.03	2.93
1.80	1.87	2.84	1.63	2.05	3.10	1.27	1.99	3.15
			1.95	2.05	3.42	1.32	2.01	3.05
						1.75	1.99	3.39

Table 3—Dipole Moment and Equilibrium Constant Values of the Complexes Obtained using Few and Smith Method²

	ΔP	$(P_{AB})_{\infty S}$	K_{app} l/mol	$R_{(D\infty)}$	μ_{ab} (D)	$\Delta\mu$
Ethyl acetate + phenol	200.00	257.56	30.0	26.9	3.38	-0.04
Butyl acetate + phenol	238.09	295.37	34.5	28.54	3.64	-0.07
Benzyl acetate + phenol	181.82	237.00	66.00	28.06	3.18	-0.43
Ethyl acetate + <i>n</i> -butyl alcohol	125.00	182.55	48.00	27.15	2.74	-0.53
Butyl acetate + <i>n</i> -butyl alcohol	153.85	212.27	58.49	28.32	3.02	-0.51
Benzyl acetate + <i>n</i> -butyl alcohol	125.00	181.70	72.00	28.52	2.74	-0.69

at a constant level, a concentration range is reached where the contribution to the total dipole moment would be mainly due to the 1:1 complexed species. Hence nearly constant value of μ_z may be equated to μ_{ab} , the dipole moment of the complex system as suggested by Huyskens *et al.* in that concentration range.

Ethyl acetate + phenol system has yielded μ_z of 3.5 D in the $C_B - C_A$ range of 0.77-0.89. This may be compared to μ_{ab} of 3.4 D obtained using the Few and Smith method. Similarly μ_z of 3.6 D obtained in the $C_B - C_A$ range of 1.08 for butyl acetate + phenol and μ_z

of 3.5 D, 2.8 D, 3.0 D and 2.8 D for benzyl acetate + phenol, ethyl acetate + *n*-butyl alcohol, butyl acetate + *n*-butyl alcohol and benzyl acetate + *n*-butyl alcohol in the respective values of the concentrations ($C_B - C_A$) are in good agreement. This clearly exhibits the concentration ranges in which the complexes are formed. As may be seen from Table 2 in the case of ethyl acetate + *n*-butyl alcohol it appears that complex formation takes place at still higher concentration.

It is also found that the apparent dipole moments (μ_{exp}) of various complex systems are smaller than the μ_z or μ_{ab} values. This is reasonable since μ_{exp} would

comprise the dipole moments of individual solute molecules and of the complexes in the solution. This should thus not exceed the values obtained for the complexed species.

From Table 3, where $\Delta\mu$ is negative for all the six systems, it is clear that there is no contribution arising due to ionic structures as it would involve very high positive value for $\Delta\mu$ (> 10 D).

Acknowledgement

One of us (RM) is grateful to the State Council of

Science and Technology, U.P., for the financial assistance.

References

- 1 Duterme P, Clerbaux T, Huyskens Z & Huyskens P, *J Phys Chem (USA)*, **72** (1968) 2373.
- 2 Few A V & Smith J W, *J Chem Soc (GB)*, (1949) 2781.
- 3 Debecker G & Huyskens P, *J Chim Phys (France)*, **68** (1971) 287, 295.
- 4 Cleverdon D, Colline G B & Smith J W, *J Chem Soc (GB)*, (1956) 4499.

Interaction of Tachyons with Superluminal Electromagnetic Fields

O P S NEGI* & B S RAJPUT

Department of Physics, Kumaun University, Naini Tal 263 002

Received 15 October 1981; accepted 1 February 1983

The study of interaction of tachyons with superluminal electromagnetic fields has been undertaken and it has been shown that the energy of this interaction is similar to that of bradyons with ordinary electromagnetic fields except that the roles of virtual and longitudinal parts are interchanged. It has also been shown that the interaction of tachyons with superluminal electromagnetic fields in time-energy representation is identical to the interaction of bradyons with ordinary electromagnetic fields in space-momentum representation.

1 Introduction

Beginning with Tanaka¹, there has been a continuing interest in faster than light particles (tachyons). In order to re-examine the theoretical existence of these particles and to develop a self-consistent quantum field theory, we have derived² the reduced expansions of fields associated with spin-1 tachyons in terms of standard helicity representations of Poincare group³⁻⁴ by using real superluminal Lorentz transformations of Antippa⁵. These reduced expansions have been used to construct the Lorentz invariant second quantized theory for these particles⁶ and it has been shown that in our theory the discrepancies pointed out in various papers⁷⁻¹¹ on the second quantization have been removed. In a recent paper, we¹² have also examined the question of emission of Cerenkov radiation by tachyons and it has been shown that the tachyons emit Cerenkov radiation through their coupling with subluminal electromagnetic fields and that a charged tachyon can emit Cerenkov radiation only in the medium in which it travels with a velocity slower than the velocity of light.

In the present paper, we undertake the study of interaction of tachyons with superluminal electromagnetic fields² by using our reduced expansions for these fields and the corresponding charge and current source densities, and it has been shown that the coupling of tachyons with superluminal electromagnetic field is due to its scalar component just like the coupling of bradyons with subluminal fields comes from the longitudinal component. It has also been shown that in superluminal electromagnetic field the virtual component is the consequence of charge source density and cannot be made vanishing by imposing Lorentz condition in contrast to the result for ordinary electromagnetic field for zero mass system.

Hamiltonian of interaction of tachyons with superluminal electromagnetic fields has been shown to

be similar to that of the bradyons interacting with subluminal electromagnetic fields except that the inequality $|\mathbf{p}| \geq k$ occurs in momentum integration and the virtual part plays the role of longitudinal part. Hamiltonian of interaction of tachyons with superluminal electromagnetic fields in time-energy representation is identical to that of bradyons with subluminal electromagnetic fields in space-momentum representation. It leads to the tachyon-bradyon reciprocity.

2 Reduced Expansions

Using the real superluminal Lorentz transformations⁵, we² have recently derived the following reduced expansions for the components of four potential $\{A_\mu\} = (i\varphi, \mathbf{A})$ in terms of standard helicity representations of Poincare group for imaginary mass system;

$$\begin{aligned} \varphi(\mathbf{x}, T) = & \frac{1}{4\pi^{3/2}} \int_{|\mathbf{p}| \geq k} \frac{d\mathbf{p}}{\omega(k, \mathbf{p})} \\ & \times \left[\frac{p}{k} \{ f^0(k, \mathbf{p}, 0) \exp[i(\mathbf{p} \cdot \mathbf{x} - \omega T)] \right. \\ & + h^{0*}(k, \mathbf{p}, 0) \exp[-i(\mathbf{p} \cdot \mathbf{x} - \omega T)] \} \\ & + \frac{\omega}{k} \{ f(k, \mathbf{p}, 0) \exp[i(\mathbf{p} \cdot \mathbf{x} - \omega T)] \\ & + h^*(k, \mathbf{p}, 0) \exp[-i(\mathbf{p} \cdot \mathbf{x} - \omega T)] \} \dots (1) \end{aligned}$$

and

$$\begin{aligned} \mathbf{A}(\mathbf{x}, T) = & \frac{1}{4\pi^{3/2}} \int_{|\mathbf{p}| \geq k} \frac{d\mathbf{p}}{\omega(k, \mathbf{p})} \\ & \times \left[\left(\frac{\omega \mathbf{p}}{k} \right) \{ f^0(k, \mathbf{p}, 0) \exp[i(\mathbf{p} \cdot \mathbf{x} - \omega T)] \right. \\ & + h^{0*}(k, \mathbf{p}, 0) \exp[-i(\mathbf{p} \cdot \mathbf{x} - \omega T)] \} \\ & + \frac{\mathbf{p}}{k} \{ f(k, \mathbf{p}, 0) \exp[i(\mathbf{p} \cdot \mathbf{x} - \omega T)] \end{aligned}$$

$$\begin{aligned}
 & + h^*(k, \mathbf{p}, 0) \exp[-i(\mathbf{p} \cdot \mathbf{x} - \omega T)] \} \\
 & + \sum_{\lambda=\pm 1} \frac{\lambda}{2^{1/2}} \{ f(k, \mathbf{p}, \lambda) \sigma(k, \mathbf{p}, \lambda) \\
 & \times \exp[i(\mathbf{p} \cdot \mathbf{x} - \omega T)] + h^*(k, \mathbf{p}, \lambda) \sigma^*(k, \mathbf{p}, \lambda) \\
 & \times \exp[-i(\mathbf{p} \cdot \mathbf{x} - \omega T)] \} \quad \dots (2)
 \end{aligned}$$

where

$$\mathbf{p} \cdot \mathbf{x} = p_1 x_1 + p_2 x_2 + p_3 t, \quad \omega T = \omega x_3 \quad \dots (3)$$

and

$$\sigma(k, \mathbf{p}, \lambda) = \begin{bmatrix} \frac{p_1(p_1 + i\lambda p_2)}{p(p + p_3)} & -1 \\ \frac{p_2(p_1 + i\lambda p_2)}{p(p + p_3)} & -i\lambda \\ \frac{p_1 + i\lambda p_2}{p} & \end{bmatrix} \quad \dots (4)$$

The wave amplitudes $f^0(k, \mathbf{p}, 0)$, $f(k, \mathbf{p}, 0)$ and $f(k, \mathbf{p}, \lambda)$ are the representations for spin-0, helicity-0 (virtual term); spin-1, helicity-0 (longitudinal term) and spin-1, helicity $\lambda = \pm 1$ (transverse term) respectively, in the basis characterized in Hilbert space upon which the generators of inhomogeneous Lorentz group operate. Energy eigen-value $\omega(k, \mathbf{p})$ is given in terms of mass ik and momentum \mathbf{p} as follows:

$$\omega(k, \mathbf{p}) = (|\mathbf{p}|^2 - k^2)^{1/2} \quad \dots (5)$$

which to be real requires

$$|\mathbf{p}| \geq k \quad \dots (6)$$

Reduced expansions (1) and (2) may be used to derive the following reduced expansions for electromagnetic fields in terms of standard helicity representations of Poincare group for imaginary mass system²:

$$\begin{aligned}
 \mathbf{E}^L &= \frac{i}{4\pi^{3/2}} \int \frac{d\mathbf{p}}{\omega(k, \mathbf{p})} \left(k \frac{\mathbf{p}}{p} \right) \\
 & \times \{ f^0(k, \mathbf{p}, 0) \exp[i(\mathbf{p} \cdot \mathbf{x} - \omega T)] \\
 & - h^0(k, \mathbf{p}, 0) \exp[-i(\mathbf{p} \cdot \mathbf{x} - \omega T)] \} \quad \dots (7a)
 \end{aligned}$$

$$\begin{aligned}
 \mathbf{E}^T &= \frac{i}{4\pi^{3/2}} \sum_{\lambda=\pm 1} \frac{\lambda}{2^{1/2}} \int \frac{d\mathbf{p}}{\omega(k, \mathbf{p})} \{ f(k, \mathbf{p}, \lambda) \\
 & \times \sigma(k, \mathbf{p}, \lambda) \exp[i(\mathbf{p} \cdot \mathbf{x} - \omega T)] \\
 & - h^*(k, \mathbf{p}, \lambda) \sigma^*(k, \mathbf{p}, \lambda) \\
 & \times \exp[-i(\mathbf{p} \cdot \mathbf{x} - \omega T)] \} \quad \dots (7b)
 \end{aligned}$$

$$\begin{aligned}
 \mathbf{H}^T &= \frac{1}{4\pi^{3/2}} \sum_{\lambda=\pm 1} \frac{1}{2^{1/2}} \int \frac{d\mathbf{p}}{\omega(k, \mathbf{p})} p \{ f(k, \mathbf{p}, \lambda) \\
 & \times \sigma(k, \mathbf{p}, \lambda) \exp[i(\mathbf{p} \cdot \mathbf{x} - \omega T)] \\
 & + h^*(k, \mathbf{p}, \lambda) \sigma^*(k, \mathbf{p}, \lambda) \\
 & \times \exp[-i(\mathbf{p} \cdot \mathbf{x} - \omega T)] \} \quad \dots (8)
 \end{aligned}$$

where \mathbf{E}^L and \mathbf{E}^T are respectively longitudinal and transverse parts of electric field while the magnetic field

\mathbf{H} is purely transverse. The expressions given by (7) and (8) are the reduced expansions for superluminal electromagnetic fields, i.e. the fields produced by spin-1 tachyons. In the superluminal frame, these electromagnetic fields couple to tachyons according to usual Maxwell's equations in view of tachyon-bradyon reciprocity. Therefore, these electromagnetic fields behave in superluminal frame as the electromagnetic fields produced by spin-1 bradyons do in subluminal frame. The details of superluminal and subluminal electromagnetic fields have already been given by us in our earlier work^{2, 13-16}.

Superluminal electromagnetic fields given by reduced expansions (7) and (8) satisfy the usual Maxwell's equations in superluminal frame of reference with the following charge (ρ) and current (\mathbf{J}) source densities;

$$\begin{aligned}
 \rho &= \frac{1}{4\pi^{3/2}} \int \frac{d\mathbf{p}}{\omega(k, \mathbf{p})} \left(\frac{k\mathbf{p}}{\omega} \right) \{ f^0(k, \mathbf{p}, 0) \exp[i(\mathbf{p} \cdot \mathbf{x} - \omega T)] \\
 & + h^0(k, \mathbf{p}, 0) \exp[-i(\mathbf{p} \cdot \mathbf{x} - \omega T)] \} \quad \dots (9)
 \end{aligned}$$

and

$$\begin{aligned}
 \mathbf{J} &= \frac{1}{4\pi^{3/2}} \int \frac{d\mathbf{p}}{\omega(k, \mathbf{p})} \left(\frac{k\mathbf{p}}{p} \right) \\
 & \times \{ f^0(k, \mathbf{p}, 0) \exp[i(\mathbf{p} \cdot \mathbf{x} - \omega T)] \\
 & + h^0(k, \mathbf{p}, 0) \exp[-i(\mathbf{p} \cdot \mathbf{x} - \omega T)] \} \\
 & + \frac{1}{4\pi^{3/2}} \sum_{\lambda=\pm 1} \frac{\lambda}{2^{1/2}} \int \frac{d\mathbf{p}}{\omega(k, \mathbf{p})} k^2 \\
 & \times \{ f(k, \mathbf{p}, \lambda) \sigma(k, \mathbf{p}, \lambda) \exp[i(\mathbf{p} \cdot \mathbf{x} - \omega T)] \\
 & + h^*(k, \mathbf{p}, \lambda) \sigma^*(k, \mathbf{p}, \lambda) \exp[-i(\mathbf{p} \cdot \mathbf{x} - \omega T)] \} \quad \dots (10)
 \end{aligned}$$

In superluminal field, longitudinal component has nothing to do with charge source density which is the direct consequence of the scalar part of superluminal vector potential (2) and cannot be made vanishing with Lorentz condition². This effect of scalar part of superluminal electromagnetic field for its contribution towards charge source density is similar to that of longitudinal part of subluminal field in bradyonic case¹⁷. Thus, tachyon-bradyon reciprocity directly leads to the interchange of longitudinal and scalar part while passing from subluminal to superluminal realm².

3 Interaction of Tachyons with Superluminal Electromagnetic Fields

In order to undertake the study of interaction of spin-1 tachyons with the superluminal electromagnetic fields by using our reduced expansions (1), (2), (9) and (10), we may write the total Lagrangian density as follows:

$$L = L_1 + L_2 \quad \dots (11)$$

where L_f is the free-field Lagrangian density of the field associated with spin-1 tachyons and L_I is the Lagrangian density due to interaction of tachyons with superluminal electromagnetic fields, and may be written as follows:

$$L_I = A_\mu^*(x) J^\mu(x) \quad (\mu = 0, 1, 2, 3) \quad \dots (12)$$

The free-field Lagrangian density of the field associated with spin-1 tachyons may be written as follows in terms of four-vector potential⁶:

$$L_f = \partial_\nu A_\mu^*(x) \partial_\nu A^\mu(x) + k^2 A_\mu^*(x) A^\mu(x) \quad (\mu, \nu = 0, 1, 2, 3) \quad \dots (13)$$

from which the free-field Hamiltonian operator have been derived in our earlier paper⁶ as follows:

$$\begin{aligned} \hat{H}_f = & - \int_{|\mathbf{p}| \geq k} d\mathbf{p} \{ \hat{f}^{0*}(k, \mathbf{p}, 0) \hat{f}^0(k, \mathbf{p}, 0) \\ & + \hat{h}^0(k, \mathbf{p}, 0) \hat{h}^{0*}(k, \mathbf{p}, 0) \} \\ & + \sum_{\lambda = \pm 1} \int_{|\mathbf{p}| \geq k} d\mathbf{p} \{ \hat{f}^*(k, \mathbf{p}, \lambda) \hat{f}(k, \mathbf{p}, \lambda) \\ & + \hat{h}(k, \mathbf{p}, \lambda) \hat{h}^*(k, \mathbf{p}, \lambda) \} \quad \dots (14) \end{aligned}$$

From Eqs (12) and (13) we get the total Lagrangian density of the field associated with spin-1 tachyons as:

$$L = \partial_\nu A_\mu^*(x) \partial_\nu A^\mu(x) + k^2 A_\mu^*(x) A^\mu(x) + A_\mu^*(x) J^\mu(x) \quad \dots (15)$$

from which the following field equation may be derived by taking the variation with respect to $A_\mu^*(x)$:

$$(\square - k^2) A^\mu(x) = J^\mu(x) \quad \dots (16)$$

The interaction Lagrangian density (12) yields the following expansion for Hamiltonian density:

$$H_I = -L_I = -A_\mu^*(x) J^\mu(x) \quad \dots (17)$$

Substituting the reduced expansions of four-vector potential $\{A_\mu^*\}$ and four-current $\{J^\mu\}$ from Eqs (1), (2), (9) and (10) into Eq. (17) and taking the integration over volume, we get the following expansion for Hamiltonian operator:

$$\begin{aligned} \hat{H}_I = & - \int_{|\mathbf{p}| \geq k} d\mathbf{p} \left(\frac{k^2}{2\omega^2} \right) \{ \hat{f}^{0*}(k, \mathbf{p}, 0) \hat{f}^0(k, \mathbf{p}, 0) \\ & + \hat{h}^0(k, \mathbf{p}, 0) \hat{h}^{0*}(k, \mathbf{p}, 0) \} \\ & + \sum_{\lambda = \pm 1} \int_{|\mathbf{p}| \geq k} d\mathbf{p} \left(\frac{k^2}{2\omega^2} \right) \{ \hat{f}^*(k, \mathbf{p}, \lambda) \hat{f}(k, \mathbf{p}, \lambda) \\ & + \hat{h}(k, \mathbf{p}, \lambda) \hat{h}^*(k, \mathbf{p}, \lambda) \} \quad \dots (18) \end{aligned}$$

which shows that in the interaction of tachyons with superluminal electromagnetic fields there is a definite contribution of scalar component which cannot be made vanishing on imposing Lorentz condition² while in the interaction of bradyons with subluminal charge source density the interaction energy comes due to the

longitudinal part. In superluminal fields interacting with tachyons the coupling due to the longitudinal part has nothing to do with interaction Hamiltonian. Since strength of coupling due to the virtual term is less than the strength of coupling due to longitudinal term¹⁸, the strength of coupling of tachyons with superluminal fields is smaller than that of bradyons with subluminal fields. For all other purposes, the interaction of tachyons with superluminal electromagnetic fields is same as the interaction of bradyons with subluminal electromagnetic fields on changing the role of virtual and longitudinal components while passing from bradyons to tachyons via superluminal Lorentz transformations. It leads to tachyon-bradyon reciprocity.

In the absence of charge source density the virtual component of fields vanishes and the fields become purely transverse and then the interaction Hamiltonian (18) may be written as follows in space-momentum representation:

$$\begin{aligned} \hat{H}_I = & \sum_{\lambda = \pm 1} \int_{|\mathbf{p}| \geq k} d\mathbf{p} \left(\frac{k^2}{2\omega^2} \right) \{ \hat{f}^*(k, \mathbf{p}, \lambda) \hat{f}(k, \mathbf{p}, \lambda) \\ & + \hat{h}(k, \mathbf{p}, \lambda) \hat{h}^*(k, \mathbf{p}, \lambda) \} \quad \dots (19) \end{aligned}$$

which is the same as the interaction of bradyons with subluminal electromagnetic fields, except that here the condition (6) is imposed on momentum integration and the roles of energy and momentum get interchanged.

Restricting the propagation of spin-1 tachyons along the tachyon corridor fixed along x_3 -axis and keeping in mind the reciprocity principle according to which the roles of time and space coordinate along the direction of motion are interchanged under superluminal Lorentz transformations, the interaction Hamiltonian may be written as follows in time-energy (ω - t) representation in which the tachyons will behave as bradyons:

$$\begin{aligned} \hat{H}_I = & \sum_{\lambda = \pm 1} \int d\omega \left(\frac{k^2}{2p^2} \right) \{ \hat{f}^*(k, \omega, \lambda) \hat{f}(k, \omega, \lambda) \\ & + \hat{h}(k, \omega, \lambda) \hat{h}^*(k, \omega, \lambda) \} \quad \dots (20) \end{aligned}$$

Then the fields become Hermitian⁶ and the interaction Hamiltonian of tachyons with transverse superluminal electromagnetic fields may be written as follows in this time-energy representation:

$$\hat{H}_I = \sum_{\lambda = \pm 1} \int d\omega \left(\frac{k^2}{p^2} \right) \hat{f}^*(k, \omega, \lambda) \hat{f}(k, \omega, \lambda) \quad \dots (21)$$

which is similar to that of interaction of bradyons with subluminal electromagnetic fields in space-momentum representation.

4 Discussion

In superluminal electromagnetic fields [i.e. reduced expansions given by Eqs (7) and (8)], the longitudinal

component has nothing to do with charge source density and the virtual part plays the role of longitudinal part just like the component of space coordinate along tachyon corridor plays the role of time on passing from subluminal to superluminal realm via the real superluminal Lorentz transformations. This contribution of the scalar part of superluminal electromagnetic field towards charge source density is similar to that of the longitudinal part of subluminal fields.

The Lagrangian density given by Eq. (12) for the interaction of tachyons with superluminal electromagnetic fields gives the interaction of superluminal electromagnetic fields for tachyons to the four-current density which satisfies the Maxwell's equations in the new frame in which the divergence, curl and time derivatives are redefined² by keeping in mind the interchange in the role of time with space coordinate along the relative motion of frames under superluminal Lorentz transformations⁵. It has been shown that the interaction energy of tachyons with superluminal electromagnetic fields is due to the coupling of scalar and transverse parts and the longitudinal component has no contribution. It has also been shown that the strength of coupling of tachyons with superluminal electromagnetic fields is less than that of bradyons with the ordinary subluminal fields. In other words, the charge source density does not remain conserved on passing from subluminal to superluminal realm¹⁶.

Furthermore, it has been shown that the interaction of tachyons with superluminal electromagnetic fields may be interpreted as the interaction of bradyons with subluminal electromagnetic fields on changing the role of virtual and longitudinal components. It is the direct consequence of tachyon-bradyon reciprocity. In the absence of charge source density the fields becomes purely transverse with respect to tachyon corridor, for which it has been shown that the interaction of tachyons with superluminal fields is the same as the interaction of bradyons with subluminal fields, except that the

condition (6) is imposed on momentum integration and the momentum is interchanged with energy. Eq. (22) for the energy of interaction of tachyons with superluminal electromagnetic fields in energy-time representation is similar to that for the energy of interaction of bradyons with subluminal electromagnetic fields in space-momentum representation. It leads to the conclusions that the tachyons interact among themselves via the superluminal electromagnetic fields as observed in a subluminal reference frame and that the superluminal electromagnetic fields couple with tachyons according to the usual Maxwell's equations¹⁹.

Acknowledgement

One of the authors (OPSN) is thankful to the CSIR, New Delhi, for financial assistance.

References

- 1 Tanaka S, *Prog Theor Phys (Japan)*, **24** (1960) 177.
- 2 Rajput B S, Purohit K D & Negi O P S, *Indian J Pure & Appl Phys*, **19** (1981) 1081.
- 3 Moses H E, *J Math Phys (USA)*, **8** (1967) 1134.
- 4 Moses H E, *J Math Phys (USA)*, **9** (1968) 16.
- 5 Antippa A F, *Phys Rev D (USA)*, **11** (1975) 724.
- 6 Rajput B S, Negi O P S & Purohit K D, *Indian J Pure & Appl Phys*, **20** (1982) 22.
- 7 Feinberg G, *Phys Rev (USA)*, **159** (1967) 1089.
- 8 Arons M E & Sudarshan E C G, *Phys Rev (USA)*, **173** (1968) 1622.
- 9 Dhar J & Sudarshan E C G, *Phys Rev (USA)*, **174** (1968) 1808.
- 10 Hamamoto S, *Prog Theor Phys (Japan)*, **48** (1972) 1037.
- 11 Schroer B, *Phys Rev D (USA)*, **3** (1971) 1764.
- 12 Negi O P S & Rajput B S, *Indian J Pure & Appl Phys*, **20** (1982) 472.
- 13 Negi O P S & Rajput B S, *Lett Nuovo Cimento (Italy)*, **32** (1981) 117.
- 14 Negi O P S, Chandola H C, Purohit K D & Rajput B S, *Phys Lett B (Netherlands)*, **105** (1981) 281.
- 15 Negi O P S & Rajput B S, *Phys Lett B (Netherlands)*, **113** (1982) 180.
- 16 Negi O P S & Rajput B S, *J Math Phys (USA)*, **23** (1982) 1964.
- 17 Rajput B S, Purohit K D & Chandola H C, *Indian J Pure & Appl Phys*, **19** (1981) 386.
- 18 Gupta S N, *Proc Phys Soc London (GB)*, **63** (1950) 601; **64** (1951) 850; Bleuler K, *Helv Phys Acta (Austria)*, **23** (1950) 567.
- 19 Marchildon L, Everett A E & Antippa A F, *Nuovo Cimento B (Italy)*, **53** (1979) 253.

Laser Excited Raman & Infrared Spectra of α -, β - & γ -Picolines

O P LAMBA, J S PARIHAR, H D BIST* & Y S JAIN†

Department of Physics, Indian Institute of Technology, Kanpur 208 016

Received 12 July 1982

A detailed vibrational study of the Raman (liquid phase) and infrared (vapour and liquid phases) spectra of α -, β - and γ -picolines is reported. The vapour phase infrared band (*A*-, *B*- and *C*-type) contours and the accurate depolarization ratios measured for the observed bands have been used to revise several earlier vibrational assignments.

1 Introduction

Raman scattering and IR absorption spectra of α -, β - and γ -picolines have earlier been studied in the selected ranges of vibrational frequencies¹⁻⁸. Long *et al.*^{1,2} gave for the first time a detailed analysis of the spectra supported by the normal coordinate analysis. Green *et al.*⁵ reported an independent study of these molecules. However, the vapour phase infrared band contours and laser excited Raman spectra, which may provide a better understanding of the vibrational dynamics of these molecules, are not available in the literature. In this paper we, therefore, report the study of such spectra and provide an analysis consistent with polarization data and vapour phase IR band contours. Some of the vibrational assignments have been modified.

2 Experimental Details

α -, β - and γ -Picolines obtained from M/s British Drug House were purified by refluxing over KOH pellets and distilling thrice under vacuum. Raman spectra were recorded on Cary-82 Raman spectrophotometer using 514.5 nm radiation 4W Ar⁺ ion laser (coherent radiation) as a source of excitation. A 1-cm quartz cell with multiple reflection arrangement served the purpose of the sample container. A polarization scrambler was used to reduce errors in the polarization measurements.

Infrared spectra were recorded on PE-521 double beam spectrophotometer. A 10-m variable path multiple reflection cell was used to record vapour phase spectra and fixed cells of thicknesses 0.025 mm and 0.5 mm with CsBr and NaCl optics were used to record liquid phase spectra.

3 Results and Discussion

The typical laser Raman spectra of liquid picolines recorded at room temperature are shown in Fig. 1. Fig.

2 shows the vapour phase IR spectra of the three molecules. These spectra cover only 250-520 cm⁻¹ range, and depict the typical *A*-, *B*- and *C*-type band contours which form the basis of our assignments. Detailed IR spectra of the vapour phase picolines are given in Ref. 9.

The peak positions measured from the spectra are given in Tables 1-3 along with the values of depolarization ratio (ρ) of the Raman bands and the nature of the band types of vapour phase IR bands. Our assignments are given in the last column of each table. The notations describing the normal modes of the molecules are those used by Green *et al.*⁵ These have been chosen particularly to facilitate the comparison of our assignments with those suggested by these authors (cf. Table 4). However, it should be noted that the notations of the modes are used for brevity in discussion, particularly for α - and β -picolines since the heavy substituents (such as CH₃) at (1) and (2) positions definitely modify the description of the normal modes and the notations cannot stand for the same description for which they stand for γ -picoline. The vibrations of the methyl group are described by usual symbols such as ν_{CH} , δ_{HCH} , Rock-CH₃, etc. The wavenumber accuracy of the measured frequencies lies within ± 1 cm⁻¹ for well developed bands and ± 5 cm⁻¹ for overlapping and broad and diffuse bands. The error in (ρ) values for different bands are between ± 0.01 and ± 0.05 (for weak and diffuse bands). In general, the $\Delta\nu_{PR}$ separation for *A*-, *B*- and *C*-type bands lies within 13 ± 2 , 12 ± 2 and 20 ± 1 cm⁻¹, respectively. However, a few exceptions may be noticed to this observation, e.g. some *B*-type bands have $\Delta\nu_{PR}$ as high as 16 cm⁻¹ and some *C*-type bands have $\Delta\nu_{PR}$ as low as 14 cm⁻¹.

A typical picoline molecule has 36 normal modes of vibrations of which 27 can be associated with ring structure and 9 to the methyl group. Among the three molecules, γ -picoline, because of its higher symmetry, is

† Permanent address: Department of Physics, North-Eastern Hill University, Shillong

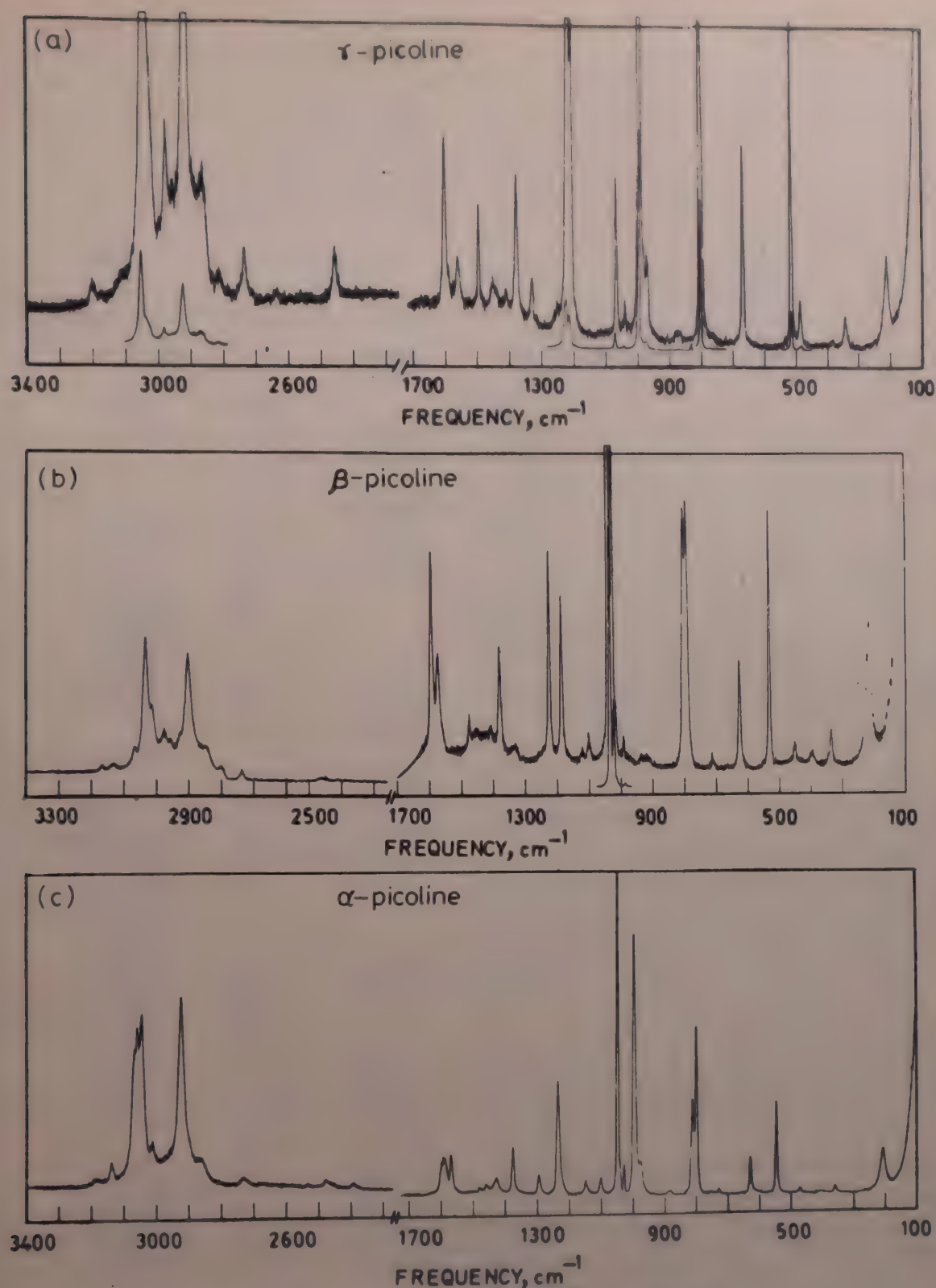


Fig. 1—Laser excited Raman spectra of liquid picolines

simpler for a better understanding of its normal modes. The analysis of the spectra of this molecule can, therefore, serve as the guideline for the analysis of the spectra of α - and β -picolines.

To a good approximation, γ -picoline is considered to have C_{2v} symmetry. Its 36 vibrations can easily be classified as: $12a_1(10R + 2M) + 12b_2(9R + 3M) + 8b_1(5R + 3M) + 4a_2(3R + 1M)$; R and M refer to the modes of vibrations associated with the ring and the methyl group, respectively. The other picolines belong to C_s symmetry. Their 24 in-plane vibrations of A' symmetry may be correlated with $12a_1 + 12b_2$

modes of γ -picoline. Similarly the 12 out-of-plane modes of A'' symmetry can be correlated with $8b_1 + 4a_2$ vibrations of γ -picoline. In the vapour phase, IR spectrum, a_1 , b_2 and b_1 symmetry modes of γ -picoline can be uniquely identified by their A -, B - and C -type band contours (typical examples of such bands are depicted in Fig. 2). The a_2 symmetry modes, which are not allowed in the infrared absorption spectrum, can be recognized as the additional depolarized bands appearing in the Raman spectrum. The identification of the modes of α - and β -picolines is slightly complicated by the fact that their A' modes may show

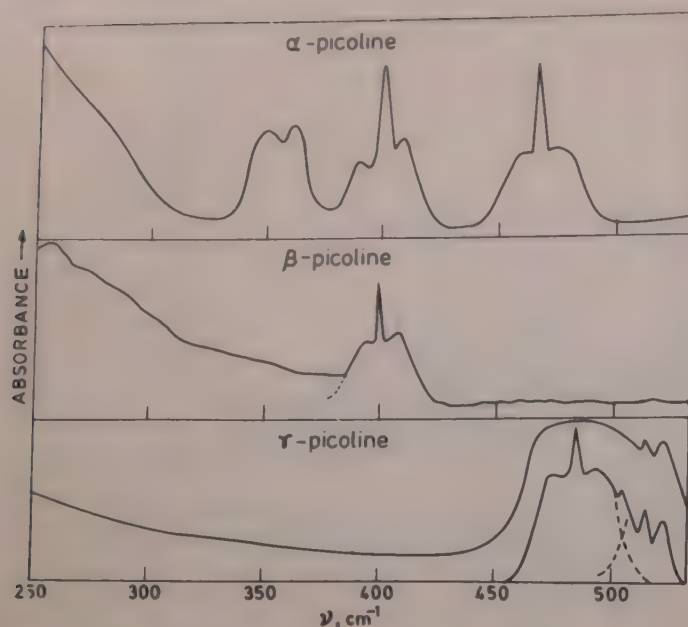


Fig. 2—Typical vapour-phase infrared spectra of picolines in 250–500 cm^{-1} frequency range

up as either *A*- or *B*-type band and exhibit depolarized Raman bands. It may be noted that *A''* modes also exhibit depolarized bands. However, the *A''* modes should distinctly appear as *C*-type bands in the IR spectrum.

Our assignments of different modes as given in Tables 1–3 are based on the facts that (i) the attributed band has the polarized/depolarized character as expected, and (ii) the associated band exhibits right band shape. In addition, we also consider that (i) in case the line in question cannot be explained as a combination or overtone of well established fundamental modes, it may either be a combination/overtone involving a mode which has not been observed directly or be one of the normal modes of vibrations; this we have particularly used to identify CH_3 twist (τ_{CH_3}) mode and some other modes (e.g. a_2 modes of γ -picoline and the corresponding modes of other molecules), and (ii) the intensity of the line in question should not be much different from the expected order [e.g. C—H bend (β_{CH}) and the angle deformation (δ_{HCH}) modes generally appear weakly in the Raman spectra, while the ring breathing mode appears strongly].

In general, our assignments suggested in view of the above mentioned points are in agreement with those reported earlier^{2,5}. However, different assignments have been proposed in several cases and in the following discussion, only these cases are discussed in detail.

Ring breathing mode (1)—The ring breathing vibrations generally appear as the strongest band in the Raman spectra of normal pyridine ring and substituted pyridine. Our assignments of this mode in γ -picoline (995 cm^{-1} band), suggested on the basis of above observations, agree well with that proposed by Long *et*

*al.*² and Green *et al.*⁵ However, in the case of β - and α -picolines, Green *et al.*⁵ have proposed 1025 and 994 cm^{-1} frequencies respectively for this mode where the Raman bands do not show maximum intensity. The strongest Raman bands in the spectra of β - and α -picolines are observed at 1040 and 1047 cm^{-1} respectively. If Green *et al.*'s proposal is accepted, one

Table 1—Raman and Infrared Frequencies of γ -Picoline

Raman (Liquid)	IR		Assignment
	Liquid	Vapour	
211(0.80)			16b
341(0.82)			15
382(0.75)	388		16a
488(0.76)	486	484.5(21)C	11
517(0.31)	515	513(15)A	6a
669(0.85)	666	678(12)B	6b
	710	713.5(17)C	15 + 16a } Fermi
	736	731.5(16)C	4 } Reson
		751(?)C	10b
		796(22)C	5
803(0.17)	800	801(?)A	12
873(0.84)	873		10a
		935(12)B	5 + τ_{CH_3}
980(?)			17a
997(0.17)	995	996.5(15)A	1
1041(0.30)	1039	1044.5(20)C	Wag CH_3
1070(0.25)	1068	1073.5(15)A	Rock CH_3
	1110	1108(11)B	18b
		1160(12)B	3
		1192(14)A	18a
1209(?)	1208	1209(?)C	Rock + τ_{CH_3}
1218(0.33)	1222	1223.5(15)A	13
	1286	1276.5(15)A	9a
		1314(11)A	12 + 6a
1331(0.75)	1333	1348(13)B	14
1381(0.40)	1381	1380(16)B	19b
1411(0.71)	1413	1420(22)B	
1435(?)	1444		δ_{HCH}
1451(0.60)		1458(13)A	
1496(0.38)	1498	1498(14)A	19a
1562(0.84)	1559	1570(14)B	8b
1605(0.84)	1603	1608(16)A	8a
2461			(13) ₂
2737			19b ₂
2817		2824(12)B	$2 \times \delta_{\text{HCH}}$
2870	2868	2883(15)A	
2922(0.20)	2928	2938(15)A	$\nu_{\text{CH}}(\text{CH}_3)$
2968(0.55)	2968	2967(11)B	
2980(0.55)			
	2996	3002(13)B	7b
3028(0.66)	3034	3039(12)B	20b
3049(0.28)			20a
3080(?)	3076	3076(14)A	2
3118			8b ₂
3203			8a ₂

Note: Values in parentheses in columns 1 and 3 respectively indicate the ρ and $\Delta\nu_{\text{PR}}$ (separation between *P* and *R* peak branches). The mark in the parentheses indicates that ρ $\Delta\nu_{\text{PR}}$ could not be measured with reasonable accuracy for the band

has to look for the suitable assignment for strongest Raman band of the spectra which is however found to be difficult. In this context, it may be mentioned that the assignment of β_{CH} mode as proposed by Green *et al.* to the strongest Raman band in case of both molecules

does not appear appropriate. We, therefore, believe that 1040 and 1047 cm^{-1} strongest Raman bands, respectively, observed for β - and α -picolines are due to ring breathing mode (1).

β_{CH} Modes (18a, 9a, 18b and 3)—The picoline molecule has four in-plane C—H bending modes, which are usually observed in 1000–1300 cm^{-1} range. Though the bands attributed earlier^{2,5} to these modes

 Table 2—Raman and Infrared Frequencies of β -Picoline

Raman Liquid	IR		Assignment
	Liquid	Vapour	
218(0.80)			16b
337(0.80)	340		15
395(0.70)	398	400(21)C	16a
	418		16b ₂
452(0.72)	453		11
	470		15 + τ_{CH_3}
534(0.30)	535	534(14)A	6a
	558		15 + 16b
628(0.56)	628	632.5(12)B	6b
714(0.50)	711	713.5(21)C	4
		751(?)C	10b
	787	785.5(21)C	5
794(0.20)			16a ₂ , 12
803(0.20)			16a ₂ , 12
919(?)	919	922.5(21)C	10a
937(?)			16a + 6a
986(?)	987	986(14)C?	Wag CH ₃
992(?)			17a
1027(?)	1027	1030.5(12)B	Rock CH ₃
1040(0.11)	1040	1049(14)A	1
1101(0.50)	1101	1102.5(12)B	18b
1123(?)	1125	1124(12)B	3
		1162(15)A	Rock + Twist (CH ₃)
1188(0.23)	1188	1192(15)A	18a
1226(0.18)	1225	1230(15)A	13
	1248	1243(13)B	6a + 4
		1297(15)A	9a
1336(?)	1333	1340(15)B	14
1380(0.30)	1383	1387(15)A	19b
1407(0.70)			
1430	1413	1423(11)B	δ_{HCH}
1456		1481(15)A	
1476(0.40)	1479	1481(15)A	19a
1571(0.55)	1576	1583(12)B	8b
1592(0.45)	1593	1601.5(14)A	8a
2460			(13) ₂
2738			8a + 13
2812		2821(11)B	2 × δ_{HCH}
2870	2869	2883(15)A	
2918(0.13)	2918		$\nu_{CH(A)}CH_3$
2944(?)	2948	2941(13)A	$\nu_{CH(E)}CH_3$
2971(?)	2975	2971(14)A	
2992(0.4)	2996	3006(15)B	7b
3030(0.59)	3032	3039(?)A	20b
3049(0.22)	3054	3069(?)A	20a
3082(?)	3085	3092(11)B	2
3148			8a + 8b
3182			8a ₂

Note: Values in parentheses in columns 1 and 3 respectively indicate the ρ and $\Delta\nu_{PR}$ (separation between P and R peak branches). The ' ' mark in the parentheses indicates that ρ $\Delta\nu_{PR}$ could not be measured with reasonable accuracy for the band.

 Table 3—Infrared and Raman Frequencies of α -Picoline

Raman Liquid	IR		Assignment
	Liquid	Vapour	
207(0.75)			16b
360(0.85)	359	358(11)B	15
407(0.76)	403	401(21)C	16a
	416		16b ₂
472(0.80)	466	468.5(20)C	11
545(0.35)	545	545.5(15)A	6a
629(0.53)	626	633(12)B	6b
		707(11)A	6a + τ_{CH_3}
730(0.70)	725	735(?)C	4
	751	751.5(21)C	10b
768(?)			5
800(0.16)	797		12
811			16a ₂
882(0.76)	884		10a
		930(11)A	(11) ₂
	974	976(14)A	17a
977(?)	999	999(12)B	Wag (CH ₃)
997(0.15)	1037	1032(13)A	Rock (CH ₃)
1030(?)	1047	1050.5(11)A	1
1050(0.13)	1095	1103(12)B	18b
1101(0.70)	1145	1147.5(14)A	3
1150		1193(12)B	Rock + τ (CH ₃)
1236(0.16)		1238(12)A	13
	1242	1245(14)A	18a
1295(0.64)	1291	1297(14)A	9a
		1354(13)B	14
1376(0.34)	1378	1382(14)A	19b
1428(0.50)	1431	1435(12)B	$\delta_{HCH(E)}$
1460(0.40)	1453	1477(15)A	$\delta_{HCH(A)}$
1480(0.40)	1481		19a
1569(0.72)	1570	1570(?)B	8b
1592(0.72)	1587	1588(?)B	13 + 15
1598(?)	1597	1603(?)A	8a
2730(?)			14 + 19b
2864(?)	2865	2881(15)A	2 δ_{HCH}
2924(0.16)	2928	2940(15)A	$\nu_{CH(CH_3)}$
2958(?)	2968	2970(?)B	$\nu_{CH(CH_3)}$
2978(?)	2998	2995(?)B	$\nu_{CH(CH_3)}$
3013(0.58)	3016	3024(12)B	7b
3047(0.36)			20a
3060(0.35)	3075	3076(14)B	20b
	3092	3094(11)A	2
3138			8b ₂
3186			8a ₂

Note: Values in parentheses in columns 1 and 3 respectively indicate the ρ and $\Delta\nu_{PR}$ (separation between P and R peak branches). The ' ' mark in the parentheses indicates that ρ $\Delta\nu_{PR}$ could not be measured with reasonable accuracy for the band.

Table 4--A Comparative Statement of Assignments of the Normal Modes of Picolines as Suggested by Us and Earlier Workers

	γ -Picoline			β -Picoline		α -Picoline	
a_1 -modes	Present study	Green <i>et al.</i>	Long <i>et al.</i>	Present study	Green <i>et al.</i>	Present study	Green <i>et al.</i>
6a X-sens	515	514	514	535	538	545	548
12 X-sens	800	801	801	803*	800	797	800
13 X-sens	1222	1212	1220	1225	1227	1236*	1233
1 Ring	995	994	994	1040	1025	1047	994
18a β_{CH}	1192†	1070	1042	1188	1041	1242	1047
9a β_{CH}	1276.5†	1220	1220	1297†	1190	1291	1143
19a $\nu_{CC, CN}$	1498	1495	1495	1479	1477	1481	1475
8a ν_{CC}	1603	1604	1603	1593	1594	1597	1590
20a ν_{CH}	3049*	3040	3040	3054	3054	3047*	3046
2 ν_{CH}	3076	3050	3050	3085	3085	3092	3080
b_2 - modes							
15 X-sens	341*	341	341	340	338	359	359
6b α_{CCC}	666	669	—	628	628	626	629
18b β_{CH}	1110	1090	1114	1101	1106	1095	1099
3 β_{CH}	1160†	1289	1283	1125	1286	1145	1291
14 $\nu_{CC, CN}$	1333	1365	1365	1340	1340	1354†	1376
19b $\nu_{CC, CN}$	1381	1417	1417	1383	1414	1376	1440
8b ν_{CC}	1559	1566	1561	1576	1575	1570	1565
7b ν_{CH}	2996	3010	3029	2996	3030	3016	3046
20b ν_{CH}	3034	3040	3050	3032	3054	3075	3080
b_1 -modes							
16b X-sens	211*	211	211	218*	217	207	207
11 ϕ_{CC}	486	490	—	453	457	466	470
4 ϕ_{CC}	726	728	728	711	708	725	729
10b γ_{CH}	781†	799	801	751†	788	751	751
5 γ_{CH}	796†	872	969	787	941	768*	940
a_2 -modes							
16a ϕ_{CC}	388	384	384	398	399	403	403
10a γ_{CH}	873	872	866	919	923	884	883
17a γ_{CH}	977*	972	937	992*	987	994	972
Methyl Group Modes							
Twist CH_3	137††		(?)	131††		162††	
Wag CH_3	1039		1148	987		999	
Rock CH_3	1068		1068	1027		1032	
$\delta_{HCH} (E)$	{ 1413		1378	1407*		1431	
	{ 1435*		1445	1430*		1431	
$\delta_{HCH} (A)$	1451*		1449	1456*		1453	
$\nu_{CH} (A)$	2928		2924	2918		2928	
$\nu_{CH} (E)$	{ 2968		2967	2948		2968	
	{ 2980*		2980	2975		2998	

*Raman (liquid) values; † vapour IR values; and ††calculated from combination modes as assigned in Tables 1-3

do lie in this range, however, they do not fit consistently with the general characteristics expected in the bands associated with these modes. For example, 1042 and 1220 cm^{-1} (γ -picoline), 1040 cm^{-1} (β -picoline) and 1047 cm^{-1} (α -picoline) Raman bands are too strong to be attributed to β_{CH} modes. The IR band observed around 1285 cm^{-1} shows a 4-type band shape peaking at 1276.5 cm^{-1} in the spectrum of γ -picoline, which makes its association with b_2 -mode 3 (as proposed earlier^{2, 5}) inconsistent. We, therefore, propose that

1192 and 1276.5 cm^{-1} bands showing 4-type band shapes should arise due to 18a and 9a modes, respectively, while 1110 and 1160 cm^{-1} bands showing B-type band shapes appear due to 18b and 3, in the same order. The bands associated with these modes of β - and α -picolines also satisfy the expected characteristics in them. Although it is quite consistent, however, it may be mentioned that 1145 cm^{-1} band attributed to mode 3 of α -picoline shows 4-type band in the IR spectrum.

$\nu_{\text{CC,CN}}$ Modes (14, 19b)—Long *et al.*² suggested that 1378 cm^{-1} band (γ -picoline) arises due to δ_{HCH} mode of CH_3 group. If it is true, the relative Raman intensity of this band (Fig. 1) suggests that it should be totally symmetric δ_{HCH} (A_1 -species under C_{3v} point group of CH_3) and should, therefore, show up A -type band in the vapour phase spectrum. However, the B -type shape exhibited by this band contradicts this assignment. It, therefore, appears more appropriate to attribute this mode to 19b which is expected around this frequency as a B -type band in the vapour phase IR spectrum. Another mode 14 has been assigned to 1333 cm^{-1} (liquid IR) band. We have not observed any band around 1365/1367 cm^{-1} as observed earlier^{2,5} due to this mode.

ν_{CH} Modes (2, 20a, 7b and 20b)—The picoline ring has four C—H stretching modes. Among these modes the one, in which all H atoms move in phase, is expected to appear weakly in IR and the strongest in the Raman spectra. This should be rigorously true for γ -picoline, for which the strongest Raman band is in fact found to be absent in IR spectrum though the mode is allowed in IR. Our expanded spectra have helped us to identify four different bands due to four C—H stretching modes, while the earlier reports have attributed a single frequency to two of the four modes.

ν_{CH} Modes (10b, 5)—Among the $5b_1$ and $3a_2$ symmetry modes of γ -picoline and the corresponding modes of α - and β -picolines, we differ from the earlier reports^{2,5} only in the assignments of two ν_{CH} modes, 10b and 5, of b_1 species (Table 4). Our assignments of b_1 modes in the case of γ -picoline are well evident because the associated bands show up C -type contour in the vapour phase IR spectrum. In the case of β -picoline, Green *et al.*⁵ proposed 788 cm^{-1} band to arise due to 10b. However, our vapour phase IR spectrum of this molecule shows a C -type band at 751 cm^{-1} which was somehow missed by Green *et al.*⁵ We, therefore, believe that 751 cm^{-1} band arises due to 10b which exactly matches with the frequency of this mode of γ -picoline. The 788 cm^{-1} band observed by us at 787 cm^{-1} has been attributed to 5 and is well supported by the C -type character in vapour phase IR spectrum. Thus all the five modes of b_1 species of γ -picoline have almost the same frequencies which are observed for the corresponding modes of β -picoline. Using this as a guideline we propose that the 768 cm^{-1} weak Raman band of α -picoline should arise due to 5 rather than 940 cm^{-1} as proposed by Green *et al.*⁵ The assignments of $3a_2$ modes are quite in agreement with those reported by Green *et al.*⁵ The 937 cm^{-1} frequency suggested by Long *et al.* for 17a of γ -picoline does not follow the selection rule as a_2 modes are forbidden in IR spectrum while a B -type band is observed at this frequency.

Methyl group vibrations—The methyl group vibrations particularly $\delta_{\text{HCH}}(A_1)$, $\delta_{\text{HCH}}(E)$, $\nu_{\text{CH}}(A)$ and $\nu_{\text{CH}}(E)$ can be easily assigned in view of their well known characteristic frequencies; A and E refer to symmetry species of C_{3v} point group. The $\delta_{\text{HCH}}(A)$ and $\nu_{\text{CH}}(A)$ are expected to show stronger Raman bands in comparison to E -species counterparts. Generally $\nu_{\text{CH}}(A)$ falls at a lower value than $\nu_{\text{CH}}(E)$ and $\delta_{\text{HCH}}(A)$ falls at a higher value than $\delta_{\text{HCH}}(E)$. The assignments in the case of γ -picoline follow these observations in addition to the expected band shapes and depolarization character. The degeneracy of $\nu_{\text{CH}}(E)$ and $\delta_{\text{HCH}}(E)$ is lifted with one exception in the case of α -picoline where a single frequency 1431 cm^{-1} (liquid)/1435 cm^{-1} (vapour) is observed for $\delta_{\text{HCH}}(E)$ mode.

The twist mode frequency in all these molecules has been computed from the combination modes as assigned in Tables 1-3. The bands associated with such combinations are those for which other suitable assignments could not be found. For γ -picoline, we observe two such combinations at 935 (B -type band) and 1209 (C -type band) cm^{-1} . These are respectively associated with $5(b_1) + \tau_{\text{CH}_3}(a_2)$ [796 + 135] and rock (b_2) + $\tau_{\text{CH}_3}(a_2)$ [1073.5 + 135.5] giving an average frequency of 137 cm^{-1} for τ_{CH_3} . Similarly for β -picoline, we observe two frequencies, 470 and 1162 cm^{-1} which are respectively associated with 15 (340 cm^{-1}) + τ_{CH_3} (130 cm^{-1}) and rock (1030.5 cm^{-1}) + τ_{CH_3} (131.5 cm^{-1}). These combinations give τ_{CH_3} an average frequency of 131 cm^{-1} . In the case of α -picoline, we observe two such combinations at 707 and 1193 cm^{-1} which are suggested to be $6a$ (545.5) + τ_{CH_3} (161.5) and rock (1032) + τ_{CH_3} (161), respectively. An average of 161 cm^{-1} frequency can be associated to τ_{CH_3} mode. If rotational motions giving rise to rock and wag are seen in C_{3v} symmetry, one finds them degenerate motions. However, in picolines, CH_3 group is attached to a planar molecule which obviously lifts up the degeneracy of these modes. These modes, in general, lie in the 950-1100 cm^{-1} range and are expected to fall close together. Our assignments are also well in line with this observation.

Issac *et al.*³, studying the far infrared spectra of several mono-substituted pyridines (taken in liquid, solid and solution states), concluded that pyridines substituted in two or three positions can usually be identified by their strong bands in 600-400 cm^{-1} region. Our vapour phase spectra (Fig. 2) not only corroborate this inference but reveal that the spectra of all the three picolines are quite distinct. The Raman spectra, however, show significant difference in other regions, e.g. (i) the strongest Raman peak, observed for γ -picoline at 995 cm^{-1} , appears around 1050 cm^{-1} for β - and α -picolines, (ii) the relative intensity of the peak

around 1496 cm^{-1} is observed to decrease considerably when the spectra are seen in order of γ -, β - and α -picolines; in fact in the last spectrum this band almost disappears, (iii) in the same order of spectra, the relative intensity of bands observed around 1600 cm^{-1} is also seen to fall appreciably, (iv) the ratio of the intensity of strong Raman peak due to symmetric $\nu_{\text{CH}}(20a)$ to that of the symmetric $\nu_{\text{CH}}(\text{CH}_3\text{ group})$ also decreases; it is higher than unity for γ -picoline while lower for α -picoline. For β -picoline, this ratio is almost unity.

4 Conclusion

The assignments of various modes of α -, β - and γ -picolines are discussed in view of the polarized Raman spectra and the vapour phase contour types. It may be suggested that certain prominent distinctions observed in the Raman spectra of α -, β - and γ -picolines may help in identifying 1-, 2- and 3-monosubstituted pyridines. However, to make this suggestion applicable without any doubt, the intensity behaviour of the Raman bands of a large number of monosubstituted pyridines should be studied.

Acknowledgement

One of us (HDB) thanks Prof. J C D Brand for hospitality during the course of the experimental work and to Dr Dave for providing freshly distilled samples. Financial support from the Department of Science and Technology, New Delhi, is gratefully acknowledged.

References

- 1 Long D A, Murfin F S, Hales J & Kynaston W, *Trans Faraday Soc (GB)*, **53** (1957) 1171.
- 2 Long D A & George W O, *Spectrochim Acta (GB)*, **19** (1963) 1777.
- 3 Issac R, Bentley F F, Sternglaz H, *et al.*, *Appl Spectrosc (USA)*, **17** (1963) 90.
- 4 Spinner E, *J Chem Soc (GB)*, (1963) 3860.
- 5 Green J H S, Kynaston W & Paisley H M, *Spectrochim Acta (GB)*, **19** (1963) 549.
- 6 Pandey B R & Tripathi R S, *Indian J Pure & Appl Phys.*, **9** (1971) 346.
- 7 Singh S S, *Labdev (India)*, **10** (1972) 14.
- 8 Berezine R I & Sidorov N K, *Opt & Spectrosc (USA)*, **32** (2) (1972) 279.
- 9 Parihar J S & Bist H D, *Technical Report No. IIT Phys 3 75*, (Indian Institute of Technology, Kanpur), 1975.

Electrodynamics of Monopoles

B S RAJPUT*, RAJENDRA P UPADHYAY† & O P S NEGI

Department of Physics, Kumaun University, Naini Tal 263 002

Received 7 December 1982

Electrodynamics of the fields associated with particles carrying magnetic charges (monopoles) has been constructed in the manner similar to the usual electrodynamics and it has been shown that the faster than light electric charge suffers a Lorentz force as if it were a magnetic monopole with magnetic charge of the same sign and magnitude.

Recent interest in the subject of monopoles^{1,2} has been enhanced by the observation of 't Hooft³ that the classical solutions having the properties of magnetic monopoles may be found in Yang-Mills theory⁴ and by an extension of this idea by Julia and Zee⁵ who showed that it is possible to construct the classical solutions in the presence of magnetic charge. Recently, the monopoles have become objects of renewed interest because of the quark-confinement problem in quantum chromodynamics. In the present communication, we have developed the electrodynamics of the fields associated with particles carrying magnetic charges (monopoles) and analysed the modified Lorentz force acting on such particles in the resulting electromagnetic fields.

Field equations in the presence of magnetic charge and current source densities may be written as follows:

$$\begin{aligned}\text{curl } \mathbf{E} &= -\frac{\partial \mathbf{H}}{\partial t} - \mathbf{k} \\ \text{curl } \mathbf{H} &= \frac{\partial \mathbf{E}}{\partial t} \\ \text{div } \mathbf{H} &= k_0 \\ \text{div } \mathbf{E} &= 0\end{aligned}\quad \dots(1)$$

where the natural units $\hbar = c = 1$ have been used and magnetic charge has been taken as the sink for the fields. The electric and magnetic fields satisfying these field equations may be written in the following form in terms of magnetic four-potential $B_\mu \equiv (\varphi, -\mathbf{B})$:

$$\mathbf{E} = \text{curl } \mathbf{B} \quad \dots(2)$$

$$\mathbf{H} = \frac{\partial \mathbf{B}}{\partial t} + \nabla \varphi \quad \dots(3)$$

The components of four-potential $\{B_\mu\}$ may be used to construct the following electromagnetic field tensor associated with the fields defined by Eqs (2) and (3):

$$\mathcal{H}_{\mu\nu} = B_{\mu,\nu} - B_{\nu,\mu} \quad \dots(4)$$

which generates the electric and magnetic fields in the following manner:

$$E^i = \epsilon^{ijk} \mathcal{H}_{jk} \quad \dots(5a)$$

$$H_i = \mathcal{H}_{0i} \quad \dots(5b)$$

and then field Eqs (1) may be written in the following compact form:

$$\mathcal{H}_{\mu\nu,\nu} = -k_\mu \quad \dots(6a)$$

$$\mathcal{H}_{\mu\nu,\nu}^d = 0 \quad \dots(6b)$$

where k_μ is the magnetic four-current density and d the dual of the tensor.

If we apply the complex superluminal Lorentz transformations⁷ on the usual field equation in presence of electric charge and current source densities, we get the following field equations in the superluminal frame when observed by an ordinary observer⁸:

$$F'_{\mu\nu,\nu} = -j'_\mu \quad \dots(7a)$$

$$F'_{\mu\nu,\nu} = 0 \quad \dots(7b)$$

where $F_{\mu\nu}$ is the usual electromagnetic field tensor and j_μ is the electric four-current density. Comparing these equations with Eqs (6a) and (6b), we may conclude that the magnetic charge gets coupled with the corresponding electromagnetic fields in the manner similar to that of the coupling of electric charge with superluminal electromagnetic field and as such we agree with Recami and Mignani⁹ that electric charge in superluminal frame (through complex superluminal transformation) behaves as a magnetic monopole.

In order to re-examine this behaviour of magnetic monopole in connection with Lorentz force, let us impose the following Lorentz condition:

$$\partial^\mu B_\mu = 0 \quad \dots(8)$$

on Eq. (6) and then we get

$$\square B_\mu = -k_\mu \quad \dots(9)$$

which may be generalized to the following form for non-zero mass system

$$(\square + m^2)B_\mu = -k_\mu \quad \dots(10)$$

*Department of Physics, Government Intermediate College,
Naini Tal 263 002

where we have used the condition

$$\partial^\nu B_\nu = \frac{1}{m^2} \partial^\nu k_\nu \quad \dots(11)$$

in place of the Lorentz condition.

The Lagrangian density which yields this field equation for non-zero mass case may be written in the following form:

$$\mathcal{L} = -m(1 - u^2)^{1/2} + \partial_\nu B^{\mu*} \partial^\nu B_\mu - m^2 B^{\mu*} B_\mu - k_\mu B^{\mu*} \quad \dots(12)$$

where the first term corresponds to the free particle and the last one to the interaction. This Lagrangian density gives the following expression for the Lorentz force acting on magnetic charge g in the electromagnetic fields given by Eqs (5):

$$\mathbf{F} = -g[\mathbf{H} - (\mathbf{u} \times \mathbf{E})] \quad \dots(13)$$

It has been shown by Recami and Mignani⁹ that the Lorentz force acting on an electric charge e moving with the superluminal velocity through electromagnetic fields is given by the equation:

$$\mathbf{F} = -e[\mathbf{H} - (\mathbf{V} \times \mathbf{E})], \quad |\mathbf{V}| > 1 \quad \dots(14)$$

Comparing this equation with Eq. (13), it may be concluded that the faster-than-light electric charge suffers a Lorentz force as if it were a magnetic monopole with a magnetic charge $g = e$ and not as that with $g = -e$ in contradiction with the conclusion of Recami and Mignani⁹. Rather this comparison demonstrates that a positive electric charge with

superluminal velocity will behave as a magnetic north pole (+ magnetic charge) in a subluminal frame instead of a south pole as claimed by Recami and Mignani⁹.

From the Lagrangian density, we may write the canonical energy momentum tensor in the following form:

$$T^{\mu\nu} = \Pi_\alpha^\mu(x) \partial^\nu \psi_\alpha(x) - g^{\mu\nu} \mathcal{L}(x) \quad \dots(15)$$

where

$$\Pi_\alpha^\mu(x) = \frac{\partial \mathcal{L}(x)}{\partial \partial_\mu \psi_\alpha(x)} \quad \text{and} \quad \psi_\alpha(x) = B_\mu(x) \quad \dots(16)$$

from which one may calculate in a straightforward manner the Hamiltonian operator \hat{H} and momentum operators \hat{p}_k . We find that these operators, thus obtained, satisfy the following commutation rule

$$[\hat{H}, \hat{p}_k] = 0 \quad \dots(17)$$

showing that momentum is conserved for magnetic monopole also.

References

- 1 Dirac P A M, *Proc R Soc London Ser A (GB)*, **133** (1931) 60.
- 2 Dirac P A M, *Phys Rev (USA)*, **74** (1948) 817.
- 3 't Hooft G, *Nucl Phys B (USA)*, **138** (1978) 1.
- 4 Yang C N & Mills R N, *Phys Rev (USA)*, **96** (1954) 191.
- 5 Julia B & Zee A, *Phys Rev D (USA)*, **11** (1975) 2227.
- 6 Thebaud L R, *Phys Rev D (USA)*, **14** (1976) 1673.
- 7 Recami E & Mignani R, *Riv Nuovo Cimento (Italy)*, **4** (1974) 209.
- 8 Rajput B S, *Proc Einstein Cent Symp*, Edited by Kondo K & Karade T M (Duhita Publisher, Nagpur), **1** (1980) 181.
- 9 Recami E & Mignani R, *Phys Lett B (Netherlands)*, **62** (1976) 41.

Thermal Expansion of Lead-Tin Alloys

S REKHA DEVI†

P CHANDRASEKHARAM & B KRISHNAMMA*

Department of Physics, S V University, Tirupati 517 502

Received 22 September 1981; revised received 9 February 1983

The coefficients of thermal expansion (α) of three lead-tin alloys (10, 15 and 18 at. % Sn in Pb) have been determined in the temperature range 90-250 K using a two-terminal capacitance dilatometer which can detect expansion by about 5×10^{-8} , and are reported for the first time.

Voluminous data on the thermal expansion of metals at low temperatures are available in the literature. However, data on metallic alloys are meagre. No data at low temperatures on the thermal expansion of Pb-Sn alloys (known as solders) are available in the literature. Balasundaram and Sinha¹ have reported the values of the coefficient of thermal expansion (α) between room temperature and 125°C as a function of volume fraction of Pb-Sn system. In the present study, three lead-tin alloys (10, 15 and 18 at. % Sn in Pb) are prepared and their α values measured in the temperature range 90-250 K. These values are reported in this note.

The appropriate weighed amounts of lead and tin (spectroscopically pure materials, supplied by M/s Johnson Matthey Ltd, London) are taken in a Pyrex glass tube and heated in a furnace to a temperature a little above the melting point of tin. The molten mixture is poured into the cylindrical hole of 1 cm diameter and 4 cm depth drilled into a graphite block, kept at room temperature. Since the alloy is prepared under atmospheric pressure, the oxidized surface layers are removed. The solidified alloys are homogenized at a temperature 50°C below the eutectic temperature. A cylindrical rod of length 2.88 cm and diameter 0.68 cm is made out of the alloy and is used as the dilatometric sample. These samples are annealed for a day at 50°C below the eutectic temperature in order to remove the effect of cold work.

The two-terminal dilatometer technique² has been used to measure α of these alloys. A two-terminal capacitance dilatometer having a detection limit of 5×10^{-8} has been fabricated in these laboratories³⁻⁵, standardized with aluminium and used for the study of α of these alloys in the temperature range 90-250 K.

The dilatometer is basically a condenser whose capacity is determined by the gap between the

specimen carrying an earthed plate and a suitably shaped piece of iron which forms the other plate. This condenser is placed in the tank circuit of a radio frequency oscillator and a change in the temperature of the dilatometer results in a change in the length of the specimen which produces a change in the width of the air gap between the plates. This causes a change in the frequency of the oscillator which is measured using a frequency meter. The relative change in length between the specimen and the iron piece can be calculated from the change in oscillator frequency after calibration. The measurements can be made virtually absolute by taking into account the cell contribution.

The expansion cell constructed in the present study is shown schematically in Fig. 1. The upper plate P_1 is made of iron and is rigidly fixed in a hylam tube (HT) using araldite. The hylam tube is fixed to a hylam plate (H). The connecting lead (CL) of plate P_1 passes through the hylam plate (H). The specimen (S) is in the form of a cylinder. It carries the other earthed condenser plate P_2 made of iron. The specimen is screwed to the iron piece (M). The distance between the two plates P_1 and P_2 is adjusted to be about 1/3 mm at room temperature with the help of the radial screw

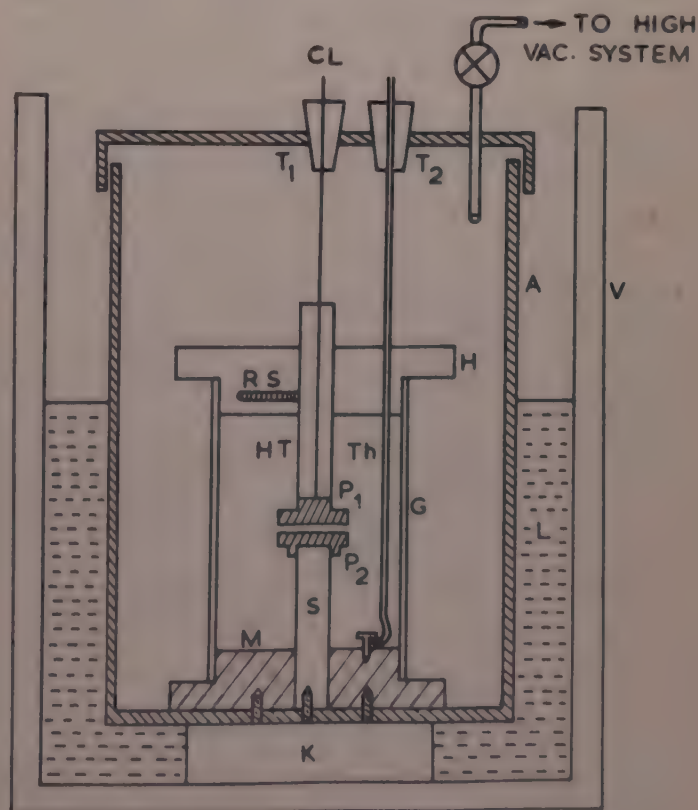


Fig. 1—Expansion cell [A: stainless steel vessel; G: pyrex glass tube; M: iron plate; P_1 : upper plate (iron) of dilatometer condenser; P_2 : lower plate (earthed) of the condenser (iron); CL: connecting lead; S: specimen; H: hylam plate; HT: hylam tube; Th: copper-constantan thermocouple; RS: radial screw; T_1 , T_2 : teflon bushes; K: conducting (brass) stand; V: metaplast vessel and L: liquid air]

† Present address: Department of Physics, S P W College, Tirupati

(RS). There is a pyrex glass tube (G) between the upper hylam plate (H) and the lower iron plate (M). The entire assembly is placed in a stainless steel vessel (A) which can be evacuated. The connecting lead (CL) from the plate P_1 and the thermo-couple wires (Th) pass through teflon bushes (T_1 and T_2) which insulate them electrically from the stainless steel can.

The change of length Δl of the specimen is given by²

$$\Delta l = \frac{A}{4\pi c^2} \left(\frac{dc}{df} \right) \Delta f \quad \dots (1)$$

where A is the area of the plates (P_1 and P_2) and C is the cell capacitance. In the present work, $A = 3.142 \text{ cm}^2$, $C = 18.88 \text{ cm}$. (converted from pF to cm), f = frequency of the oscillator and $(dc/df) = 1.988 \times 10^{-5} \text{ cm/Hz}$.

The Eq. (1) gives

$$\Delta l = 13.95 \times 10^{-9} \Delta f \quad \dots (2)$$

The length of the sample used was 2.88 cm.

$$\text{Hence } \frac{\Delta l}{l} \simeq 5 \times 10^{-9} \Delta f$$

The frequency f could be measured correct to 10 Hz using a Beckman frequency counter 6155.

Hence, the accuracy for the present measurements of $(\Delta l/l)$ was about 5×10^{-8} , which is comparable to that attained by optical interference methods.

The values of α for the three Pb-Sn alloys are presented in Table 1. It is evident that there is a regular increase in the value of α with the increase of temperature for all the three alloys. The thermal expansion is found to increase with increasing concentration of Sn in Pb. Pure lead and pure tin have higher thermal expansion coefficients than all the three alloys. Addition of Sn in Pb causes a drop in α .

An attempt has been made to compare the present values of α at 250 K with those of Balasundaram and Sinha¹ obtained between room temperature and 125 °C (the mean temperature $\sim 350 \text{ K}$). The densities of the three alloy specimens have been measured at room temperature and the volume fractions corresponding to these are evaluated. From the plot of Balasundaram and Sinha¹, the values of α corresponding to these volume fractions are read off and are given in Table 2 for comparison. The agreement is quite good.

Table 1—Values of α for the Three Pb-Sn Alloys in the Temperature Range 90-250 K

Temperature K	$\alpha \times 10^{-7} (\text{K}^{-1})$ for		
	Pb + 10 at. % Sn	Pb + 15 at. % Sn	Pb + 18 at. % Sn
90	1.25	1.39	1.55
110	1.32	1.56	1.74
130	1.54	1.71	1.91
150	1.68	1.90	2.10
170	1.89	2.09	2.28
190	1.95	2.15	2.36
210	2.25	2.32	2.44
230	2.31	2.44	2.51
250	2.40	2.53	2.66

Table 2—Comparison of the Values of α (in 10^{-7} K^{-1}) for Pb-Sn Alloys of the Present Study with Those of Ref. 1

At. % of Sn in Pb	Present study (250 K)	Ref. 1 (350 K)
10	2.40	2.76
15	2.53	2.80
18	2.66	2.82

The authors wish to thank Prof P Jayarama Reddy for his interest in the work. One of the authors (PCS) is grateful to the University Grants Commission, New Delhi, for the award of a Teacher Fellowship under the Faculty Improvement Programme.

References

- 1 Balasundaram L J & Sinha A N. *J Appl Phys (USA)*, **42** (1971) 5207.
- 2 White G K. *Thermal expansion symposium Program and Summary Proceedings*. Corning N Y (USA), 27 Sep.-9 Oct. 1971 (Corning Glass Works, New York) 1971, 7.
- 3 Nagi Reddy B P. *Studies in low temperature Elastic and thermal properties of some ferrites*. Ph D thesis, S V University, Tirupati, 1973.
- 4 Chandrasekharam P. *Fabrication and standardisation of a two-terminal dilatometer and measurement of thermal expansion of copper at low temperatures*. M Phil dissertation, S V University, Tirupati, 1978.
- 5 Rekha Devi S. *Thermal expansion studies on lead and tin alloys at low temperatures*. M Phil dissertation, S V University, Tirupati, 1979.

Fluorescence of MgO:Ce

M N BAPAT & S SIVRAMAN*

Department of Physics, University of Saugar, Saugar 470 003

Received 3 July 1982; Revised Received 1 September 1982

Fluorescence of MgO:Ce is reported. Dependence of emission intensity on cerium concentration, temperature and atmosphere of firing has been investigated. Lithium coactivation is found to improve the intensity of luminescence emission.

Fluorescence of trivalent cerium in different hosts has been widely studied¹⁻⁴. The region of emitted wavelength depends on the choice of the host and extends from ultraviolet to red¹⁻³. Here we report results of our study on the luminescence emission from MgO:Ce.

We observed one intense peak in MgO:Ce at 530 nm (F_2 in Fig. 1) and two weaker ones, one at 490 nm (peak F_1) and another at 600 nm (peak F_3). The intensity of the short wavelength side peak F_1 decreased with increasing cerium concentration while that of F_2 increased⁴. The intensity of F_3 remained appreciably unaffected. The relative emission intensity values for 530 nm peak are listed in Table 1 for cerium concentration and various conditions of phosphor preparation when excited by 30 kV, 10 mA, X-rays. For a CeO concentration of 10^{-3} g/g of MgO, the intensity of luminescence had the following relative values when the samples were fired at different temperatures:

Firing Temperature	800°C	900°C	1000°C
Intensity (in arb. units)	70	130	180

When lower concentration of cerium was used in this study, it was found that it can efficiently transfer energy to europium while higher concentrations quenched the europium emission. A similar effect for Tb has been observed by Khare and Ranade².

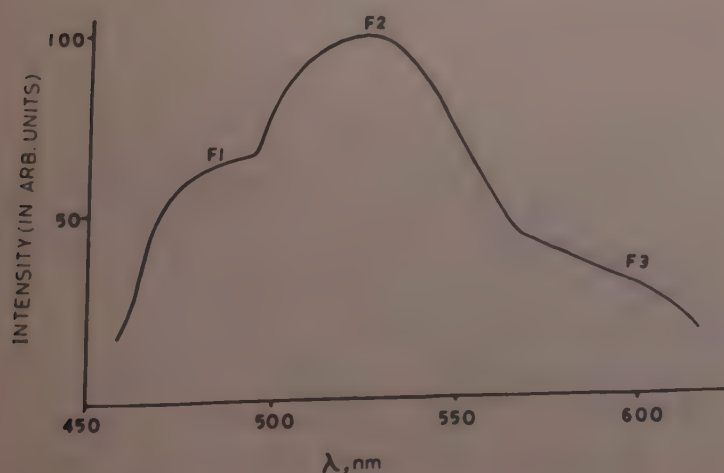


Fig. 1—Spectral distribution curve of MgO:Ce

Table 1—Effect of Atmosphere of Firing, and Concentration of Cerium on Intensity (I) of 530 nm Peak of MgO:Ce

(values of emission intensity are in arbitrary units)

conc. of CeO in g/g of MgO	I atmosphere air (with Li)	I atmosphere reducing (with Li)	I atmosphere oxidizing (with Li)	I atmosphere air (without Li)
5×10^{-5}	150	60	180	20
10^{-4}	160	65	190	25
5×10^{-4}	170	74	215	27
10^{-3}	180	80	230	30
10^{-2}	250	115	320	35
5×10^{-2}	320	65	390	38
10^{-1}	470	70	500	42

Temperature of firing was 100°C.

For higher concentration of Ce, concentration quenching begins. The optimum value for concentration is lower when samples are fired in reducing atmosphere. For a concentration, ten times the optimum value, again a rise in emission intensity is observed which may be due to the dipole-quadrupole transfers⁵ becoming effective.

It is observed that lithium coactivation increased the emission intensity when possibly two Mg^{2+} ions are replaced by one Ce^{3+} and one Li^+ .

Dependence of emission intensity on temperature and atmosphere of firing may be due to the change in the number of trivalent cerium ions that enter the lattice site.

The band structure suggests that the observed emission is due to allowed dipole-dipole transitions². The intense peak F_2 is due to $^2D_{3/2} \rightarrow ^2F_{5/2}$ transition, F_1 due to $^2D_{5/2} \rightarrow ^2F_{5/2}$ transition and the weaker F_3 results from $^2D_{5/2} \rightarrow ^2F_{7/2}$ transition of cerium in MgO. The additional band F_3 in the red region is observed, since the activator substitutes for the cation of the host⁶.

The wide differences in the position of the observed emission peaks in various hosts from those due to the transitions in atomic levels of Ce may be due to the following facts: (i) cubic site distortions due to the additional component (Li), (ii) the activator occupying different sites in the lattice⁷ and (iii) different concentrations of Ce resulting in different intensities of component peaks. Thus, the overall appearance of the emission spectra may also be different. Similar changes have already been reported by Urbach *et al.*⁸ for SrS:Ce, Sunta⁹ and Gobrecht¹⁰ for CaS:Ce and Okono *et al.*¹¹ for Y_2O_3 :Ce and Lu_2O_3 :Ce.

References

- 1 Handerson S T, Ranby P W, *J Electrochem Soc (USA)*, **104** (1957) 612.
- 2 Khare R P, Ranade J D, *Indian J Pure & Appl Phys*, **13** (1975) 664.
- 3 Fujitao H, Okamoto F, Kato K, *Jap J Appl Phys (Japan)*, **19** (1980) 1063.
- 4 Th P J Botdin, *Philips Res Rep (Netherlands)*, **7** (1952) 197.
- 5 Curie D, *Luminescence in Crystals*, translated by G F J Garlick (Matheun, London) 1963, 222.
- 6 Blasse G, Bril A, *Appl Phys Lett (USA)*, **11** (1967) 53.
- 7 Ronde H, Krol D M, Blasse G, *J Electrochem Soc (USA)*, **127** (1973) 1277.
- 8 Urbach F, Pearlman D & Hammendinger H, *J Opt Soc Am (USA)*, **36** (1946) 377.
- 9 Sunta C M, *Phys Stat Sol (Germany)*, **a53** (1979) 127.
- 10 Gobrecht H, *Ann Phys (Germany)*, **31** (1938) 181.
- 11 Okano S Y, Abe T, Hoshina T, *J Lumin (Netherlands)*, **24** (1981) 309.

Dielectric Relaxation Studies of Chloro-Substituted Phenoxyacetic Acids in *p*-Dioxane Solutions

S C SRIVASTAVA* & M S SINHA

Department of Physics, University of Allahabad, Allahabad 211 002

Received 23 August 1982; revised received 6 January 1983

The mean relaxation times (τ_0) and distribution parameters (α) of 4-chloro-, 2,4-dichloro- and 2,4,5-trichloro-phenoxyacetic acids in dilute *p*-dioxane solutions have been evaluated at 3 different temperatures using the Cole-Cole arc plot method. Measurements of permittivity and dielectric loss have been made at 5 concentrations and 4 frequencies (100 MHz, 150 MHz, 4.00 and ~ 10 GHz) apart from those at static and optical frequencies (Na-*D* line). The values of τ_0 and α are found to increase with increasing chain length of these acids and decrease with increasing temperature. Large values of τ_0 in these acids indicate complex formation in the solutions under present study.

Because of the importance of chloro-substituted phenoxyacetic acids regarding plant growth activity^{1,2}, it seemed desirable to determine their dielectric relaxation behaviour. The study of dielectric dispersion of polar molecules provides an important approach to an understanding of the molecular structure and interactions in liquids and solutions. The relaxation times (τ_0) of some fatty acids³ and phenylacetic acids^{4,5} have been reported by other workers. But, to our knowledge, no work has been reported so far on the study of relaxation times of chloro-substituted phenoxyacetic acids. In view of the relatively small amount of information available on these compounds of biological importance⁶, the present investigation has been undertaken.

The compounds 4-chlorophenoxyacetic acid (I), 2,4-dichlorophenoxyacetic acid (II) and 2,4,5-trichlorophenoxyacetic acid (III) were procured from Fluka (Switzerland), Merck (Germany) and BDH (England) respectively. The solvent *p*-dioxane (AnalaR) was procured from BDH (India) and was distilled and dried in a desiccator before use.

The permittivity (ϵ') and dielectric loss (ϵ'') of solutions of I, II and III in *p*-dioxane solvent were measured at 5 concentrations each in the mole fraction range 0.0108-0.1017 at two RX-meter frequencies (100 and 150 MHz) and at two microwave frequencies (4 GHz and ~ 10 GHz) at temperatures 30, 45 and 60°C. The temperature was maintained within $\pm 0.5^\circ\text{C}$ by a thermostat. At 4 GHz and ~ 10 GHz Smyth's method⁷ was used for taking measurements. The apparatus used was the same as that used earlier⁸ except for some minor changes. The accuracy of measurement for ϵ'

and ϵ'' was $\pm 1\%$ and $\pm 4\%$ respectively. The static permittivity of the solutions at 100 kHz was measured at 30, 45 and 60°C using a dipolemeter based on the principle of heterodyne beat method as described elsewhere⁹. The refractive index (n_D) of the solutions was measured at 30, 45 and 60°C for sodium-*D* line on an Abbe refractometer, and high-frequency limiting permittivity (ϵ_∞) was obtained by taking the square of the refractive index ($\epsilon_\infty = n_D^2$).

It has been found empirically by Heston *et al.*⁷ and shown theoretically by Higasi¹⁰ that for dilute solutions of polar solute in nonpolar solvent both ϵ' and ϵ'' are linear functions of the solute concentration, and, therefore, the measured values of ϵ' , ϵ'' , ϵ_0 and ϵ_∞ can be replaced by the slopes a' , a'' , a_0 and a_∞ of the plots of these quantities with respect to the solute concentration.

For these chloro-substituted phenoxyacetic acids (I)-(III) the complex plane plots (a'' against a') are Cole-Cole arcs¹¹. The values of mean relaxation time (τ_0) and distribution parameter (α) have been calculated from these plots (Table 1).

The values of τ_0 of the compounds (I)-(III) (Table 1) increase with increasing chain length. This is in agreement with the earlier work³ on fatty acids. It has also been observed that α increases with increasing chain length¹² and decreases with increasing temperature for each compound. The latter effect indicates that the orientation is becoming more uniform. It may be interpreted¹³ that the expansion of the liquid has reduced the effect of the arrangement of the neighbouring molecules in the orientation process.

The direction of dipole moments in carboxylic acid molecules is nearly perpendicular to the C—C bond which binds the carboxyl group with the rest of the molecule. As a result, hydrogen bond may not have any effect on the resultant carboxyl group moment² and independent orientation of carboxyl group is hindered. It is evident that the two oxygen atoms of the carboxyl group have larger interaction with the neighbouring

Table 1—Values of τ_0 and α for Chloro-substituted Phenoxyacetic Acids in *p*-Dioxane at Different Temperatures

Temperature °C	I		II		III	
	τ_0 psec	α	τ_0 psec	α	τ_0 psec	α
30	103.3	0.24	120.8	0.30	143.2	0.42
45	99.5	0.23	109.6	0.27	120.5	0.41
60	93.7	0.19	103.4	0.24	108.7	0.39

hydrogen atoms of the rest of the chain than does the hydrogen atom of the hydroxyl group with its neighbours. This difference in interaction may lead to the independent orientation of the OH—group from the rest of the molecule in alcohols and precluding independent orientation of —COOH group in acids.

The large values of τ_0 suggest that the orientation of the acid molecules is such that the dipole bearing groups, i.e. the carboxyl group, is firmly bound to the rest of the molecule. The partial proton transfer resulting in the coexistence of H-bonded and proton transfer complexes in acetic acid-dioxane mixtures has been reported by Sabesan *et al.*¹⁴ Such a behaviour of complex formation in the solutions of the acids under present study may also be responsible for the large values of τ_0 .

The value of τ_0 of compound I determined in the present work is larger than that of *p*-fluorophenoxyacetic acid⁵ in *p*-dioxane solution determined at Lakehead University, Ontario, Canada ($\tau_0 = 94.2 \times 10^{-12}$ s at 25°C). The value of τ_0 in chloro-substituted acid molecules is found to be larger than in the fluoro-substituted acid molecules by other workers⁴ also. It may be due to the fact that the former is larger in size as compared to the latter. This check renders a good support in favour of our results on these chloro-substituted phenoxyacetic acids.

The authors are grateful to Prof. Krishnaji, Dr Pradeep Kumar and Dr Vinod Prakash for their constant interest, valuable help and discussions in the present work.

References

- 1 Wain R L *Plant growth substances*, (Royan Institute of Chemistry, London) Monograph No. 2, 1953.
- 2 Srivastava S C & Sinha M S, *Indian J Phys Part B*, **55** (1981) 61.
- 3 Potapenko G & Wheeler (Jr) D, *Rev Mod Phys (USA)*, **20** (1948) 143.
- 4 Saxena Meena, Singh B K P N & Gupta R C, *Indian J Pure & Appl Phys*, **11** (1973) 468.
- 5 Srivastava S C, *Dielectric relaxation of some substituted phenylacetic acids and p-fluorophenoxyacetic acid*, unpublished work.
- 6 Curtiss R F, *Nature (GB)*, **232** (1971) 396.
- 7 Heston (Jr) W M, Franklin A D, Henelly E J & Smyth C P, *J Am Chem Soc (USA)*, **72** (1950) 3443.
- 8 Krishnaji & Man Singh A, *J Chem Phys (USA)*, **41** (1964) 827.
- 9 Crossley J & Srivastava S C, *Adv Mol Relax Processes (Netherlands)*, **8** (1976) 111.
- 10 Higasi K, *Bull Chem Soc Jpn (Japan)*, **39** (1966) 2157.
- 11 Cole K S & Cole R H, *J Chem Phys (USA)*, **9** (1941) 341.
- 12 Laquer H L & Smyth C P, *J Am Chem Soc (USA)*, **70** (1948) 4102.
- 13 McGeer P L, Curtiss A J, Rathmann G B & Smyth C P, *J Am Chem Soc (USA)*, **74** (1952) 3541.
- 14 Sabesan R, Varadarajan R & Sargurumoorthy K, *Indian J Pure & Appl Phys*, **15** (1977) 538.

Design & Fabrication of a 250l Liquid Nitrogen Storage Vessel

M M KRISHNA & R G SHARMA*

National Physical Laboratory, New Delhi 110012

Received 28 January 1982; revised received 16 December 1982

A liquid nitrogen storage container of cylindrical vertical type with a total capacity of 250l has been fabricated using indigenous materials for laboratory use. The inner vessel has been designed for an internal pressure of 55 psi using stainless steel sheet of 1.5 mm thickness with two stiffening rings to take care of liquid pressure. The outer vessel has been fabricated out of MS sheet of 3 mm thickness and has three stiffening rings which enable it to withstand 200 psi collapsing pressure. The inner vessel hangs from the top of the MS vessel through 30 cm long thin-walled SS neck. Three symmetrical bottom supports of low conductivity-to-strength ratio have been provided to protect the container against accidental jerks during movement. Evacuated perlite of density 50 kg/m³ has been used as insulation. Preliminary trials show that the vessel with perlite at 10⁻¹ torr has an evaporation rate of liquid nitrogen 6.5% per day which is close to the theoretically estimated value.

The note describes the design and fabrication of a 250l liquid nitrogen storage vessel for laboratory use.

Insulation—The heat transfer in double walled vacuum insulated dewar vessels from the outer warm surface to the inner cold surface is largely caused by radiation across the evacuated space. This radiation heat leak W_R is governed by Stefan-Boltzmann law:

$$W_R = \sigma (A_2 T_2^4 - A_1 T_1^4) \epsilon$$

where the various symbols have their usual meaning. W_R can be minimized by choosing a container material of low emissivity ϵ such as stainless steel. The emissivity of a material, however, has a minimum value below which it cannot be reduced by any surface treatment¹. The value of W_R can be drastically reduced by using floating multiple radiation shields of low emissivity material between the two surfaces but this is extremely difficult from the fabrication point of view. Evacuated perlite filled in the interspace on the other hand provides the benefits of multiple radiation shields and is very convenient to use. Perlite has a minimum in the apparent thermal conductivity \bar{k} curve, at a pressure $\sim 10^{-3}$ torr. Since perlite adsorbs moisture, vacuum in the interspace can be maintained for very long periods. In view of these advantages we decided to use perlite as insulation in our vessel.

Inner and outer vessels—The wall thicknesses of the cylindrical inner vessel and the hemispherical dish heads have been calculated in accordance with the ASME Boiler and Pressure Code². The 1.5 mm thick 304 SS sheet used for the inner vessel can withstand an internal pressure of over 55 psi. Two SS stiffening rings

have been provided outside this vessel to maintain the roundness against the liquid pressure. A perforated jacket filled with activated charcoal is welded to the bottom of the vessel which acts as a cryopump when evacuated and cooled to 77 K. All the joints of the inner vessel were argon-arc-welded and the vessel surface was polished.

To keep the cost of the container low, the outer vessel was made out of mild steel of thickness 3 mm. In order to have about 15 cm thick perlite insulation, the diameter of the outer vessel was kept 900 mm and length 1100 mm. Three stiffening rings used inside the outer vessel cut the length into four segments and enabled it to withstand a collapsing pressure of 200 psi against a minimum requirement of 75 psi by ASME Code² for the cylinder and the hemispherical dish heads. The design of the container is shown schematically in Fig. 1.

Neck and bottom support—The inner vessel has a SS pipe neck of 2 mm wall thickness, 38 mm inner diameter and 300 mm length. The outer vessel top dish head has a SS neck pipe of 5 mm wall thickness, 140 mm outer diameter and 200 mm length, argon-arc-welded to it. The two neck pipes were argon-arc-welded together through a 5 mm thick SS flange. This flange thus supports the entire weight of the inner

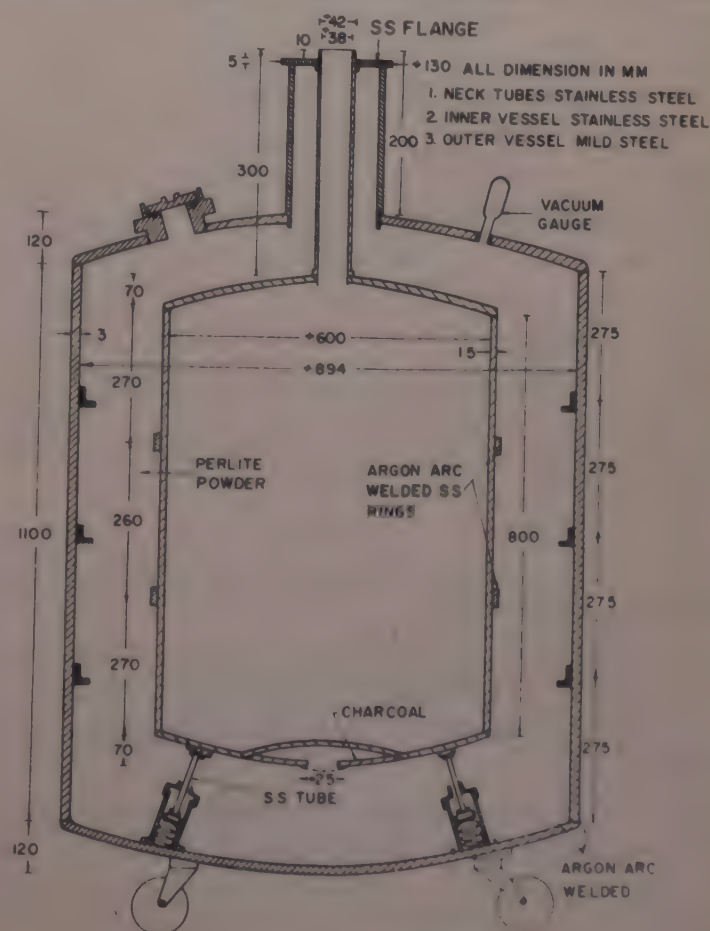


Fig. 1—Design details of the inner and outer vessels of the container

liquid nitrogen-filled vessel. The stresses at the inner and outer edges of the flange S_i and S_o due to the inner vessel and its contents have been worked out from the equations given by Roark³ and found to be 5920 psi and 6503 psi respectively. These values are well below the allowable stress of 18750 psi.

To take care of the thermal contraction and any accidental movement of the inner vessel during transport, three spring loaded symmetrical supports are provided at the bottom. The design of these supports is schematically shown in Fig. 2(b). The inner vessel is held under compression from the bottom through three SS tubes each 100 mm in length, ID 9.5 mm and OD 10 mm. Each tube is push-fitted into a SS disc arc-welded to the bottom of the inner vessel at one end and into a MS piston at the other. As shown in Fig. 2(b), the piston rests on a spring and moves in a cylindrical guide. The piston has an insulating FRP lining to avoid direct thermal contact with the outer vessel and minimize solid heat transfer to the inner vessel. Even though the bottom supports are not expected to hold the weight of the inner vessel, our calculations show that these SS support tubes can safely hold a weight of 1500 kg in the worst situation.

Assembly and testing—The inner vessel was fabricated according to the dimensions shown in Fig. 1. All the welded joints were recycled to liquid nitrogen temperature by pouring liquid nitrogen on to them. For safety reasons, the inner vessel was pressure tested up to 20 psi only. No fall in pressure was observed over a period of one week. The outer vessel was fabricated without bottom and the inner vessel was assembled into the outer one by welding together the neck pipes through the SS flange. Bottom supports were fixed in position on to the lower dish head of the outer vessel pressed against the inner vessel bottom and welded to the outer vessel. The interspace was pumped through a port in the top dish head and sealed. This vacuum sealing arrangement is shown in Fig. 2(a). The outer vessel was degassed by pumping the interspace and heating the container for a few weeks. Required quantity of perlite was filled into the interspace and pumped for several days.

Heat transfer and performance—The total heat transfer to the inner liquid vessel consists of the following components:

(1) Solid conduction through the inner vessel neck and the bottom supports is equal to 1.74 W.

(2) Gas conduction through the nitrogen vapours is equal to 0.02 W.

(3) Heat influx through the perlite insulation has been calculated from the expression⁴

$$Q = k \frac{(T_2 - T_1)}{l} \sqrt{A_1 A_2}$$

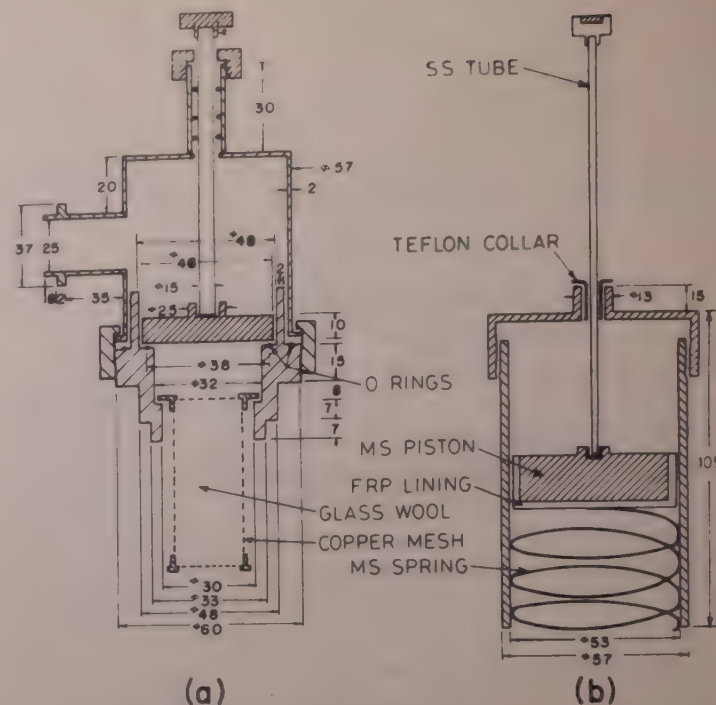


Fig. 2—(a) The drawing of the arrangement made for the evacuation of the interspace and the vacuum sealing, (b) schematic drawing of one of the three symmetrical bottom supports used in the container

where \bar{k} is the mean effective thermal conductivity of the insulation between the boundary temperatures T_1 and T_2 . A_1 and A_2 are the surface areas of the inner and outer vessels respectively. Though this expression is exact for concentric spherical vessels, it is equally applicable to cylindrical vessels within 5% error, if the insulation thickness is not more than 50% of the radius of the cylinder. We have filled perlite at an average density of 50 kg/m³ and pumped to around 10⁻¹ torr. The heat transfer through perlite at this pressure, boundary temperatures and packing density comes out to be about 23 W taking a reasonable value of $\bar{k} = 60 \mu\text{Wcm}^{-1}\text{K}^{-1}$. The total heat influx to the liquid in the inner container is about 25 W which will evaporate about 13.5 litre of liquid nitrogen per day. This is close to our experimentally observed rate of evaporation. It is hoped that the evaporation rate will be brought down considerably by improving the vacuum in the interspace. The inner vessel needs about 11 litre of liquid nitrogen for initial cooling on the basis of latent heat calculation.

We thank Mr Y S Reddy for many useful discussions and Mr J R Anand for providing all workshop help. We also thank Drs V G Bhide and A R Verma, (National Physical Laboratory) for their interest in this work and permission to communicate the paper.

References

- 1 Fulk M M & Reynolds M M. *J Appl Phys (USA)*. **28** (1957) 1464.
- 2 ASME boiler and pressure vessel code, unfired pressure vessels (American Society of Mechanical Engineers, New York). 1965.
- 3 Roark R J. *Formulas for stress and strain* (McGraw Hill, New York) 1954.
- 4 Scott R B. *J Res Natl Bur Stand (USA)*. **58** (1957) 317.

Preamplifiers for Charged-Particle Detectors in High-Resolution Spectroscopy

M B CHATTERJEE† & R BHATTACHARYA*

Saha Institute of Nuclear Physics, Calcutta 700 064

Received 20 August 1981; accepted 28 January 1983

Charge-sensitive preamplifiers have been designed and fabricated in the laboratory in view of the need for achieving optimum resolution and size for their operation inside the scattering chamber. The performance of these preamplifiers has been tested with the silicon surface-barrier detectors. These preamplifiers have shown excellent energy resolution and stability for the operation in conjunction with the surface-barrier detectors for high-resolution, charged-particle spectroscopy.

Energy resolution is one of the most important characteristics of the semiconductor detectors that sets the limit of ability to resolve the peaks of two energetic radiations having minimum energy difference. Resolution of the semiconductor detectors used to detect nuclear radiation depends on several factors of which electronic system resolution plays an important role. In order to minimize the deteriorating influence of the associated electronic system in achieving good energy resolution, low-noise high-stability electronics is being used in recent years¹⁻⁵. The availability of the low-noise electronic components indigenously has made it possible to fabricate the charge-sensitive FET preamplifiers for silicon surface-barrier detectors.

The aim of the present work is to develop a suitable charge-sensitive preamplifier for experiments with a cyclotron beam and having as high a resolution as is commensurate with the noise limit of the detector, using indigenous components. The preamplifier must also drive about a 100 m coaxial cable at 50 ohm leading to the data acquisition room.

The Preamplifier: Circuit details and proper bias maintenance—The circuit diagram of the preamplifier is shown in Fig. 1. The preamplifier consists of the standard stages, viz. a charge-sensitive stage having a high loop-gain followed by a cable driver. No voltage gain stage has been introduced here in order to make its size as small as possible, so that it can be placed very close to the detector within the vacuum of the scattering chamber. The components including the nichrome-chip resistors chosen for their small size and tantalum capacitors are of indigenous manufacture.

The FET which yielded best resolution is selected from CIL 973 type. The feedback capacitor of 1.5 pF is made from a 1.5-cm long piece of RG62/U cable whose two conductors serve as the two electrodes of the capacitor. This has been found to work very well. The input biasing network, though not essential for operation of the preamplifier, has been introduced to reduce the deleterious effect of external leakage between the gate and source leads of the FET. It has been shown by many workers⁴⁻⁶ that the noise characteristics of this type of a preamplifier depend critically on the quiescent biasing condition and its stability. Thus selection of a proper biasing condition and maintenance of it to a stable level need be given as much care as possible. It has been noticed during the progress of this work that excessive humidity along with deposition of atmospheric pollutants cause a small leakage current to flow in the external gate-source path. This leakage current, being fluctuating in nature, causes a fluctuation in the input biasing condition which could be avoided as far as possible. Partial suppression of this source of disturbance has been made possible by introducing the present biasing scheme (Fig. 1). The gate voltage determined by the voltage at the junction of the two 10 M resistors is held nearly at zero volt by the dc current flowing through them. The two other ends of these resistors are connected to suitable voltage points as indicated in Fig. 1. The leakage current between the gate and source leads, being usually much less than this dc current, cannot substantially disturb the quiescent gate voltage. For circuits built with either a 10 M resistor directly grounded from the gate or the 50 M resistor only to determine the quiescent gate voltage, it has been found that to attain the best possible energy resolution with a given preamplifier circuit assembly, it is necessary to avoid moisture and pollutant deposition therewith by warming the circuit suitably. With the biasing network incorporated in the

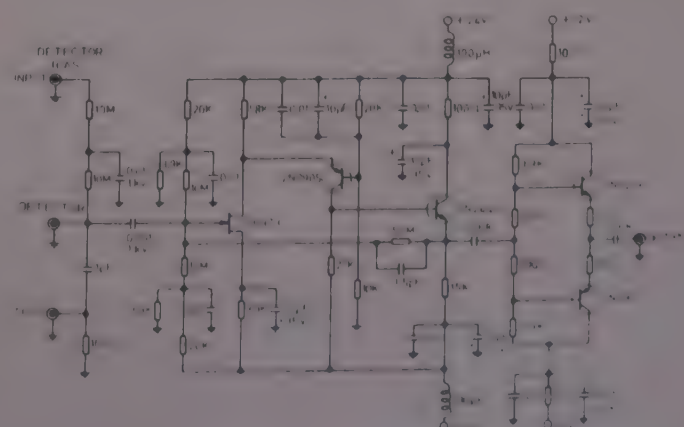


Fig. 1 Circuit diagram of the preamplifier

†Present Address: Van de Graaff Laboratory, Department de Physique, Universite Laval, Quebec, Canada G1K 7P4

circuit, the necessity of warming the circuit is eliminated without deterioration of performance shown in Fig. 2. However, operating the circuit in vacuum after through cleaning does not essentially require this biasing network.

The whole preamplifier circuit is needed to be placed in an evacuated scattering chamber (pressure of 10^{-5} torr). The components have, therefore, to be so chosen that they do not get degassed too much to destroy the vacuum and have good low-noise property at the same time. Large number of disc capacitors, nichrome-chip resistors, transistors, etc. were previously placed in a vacuum of 10^{-5} torr and tested for degassing.

Performance of the preamplifier—The performance of the preamplifier depends on the various noise contributions which have been discussed by Goulding⁴. The circuit noise has been measured as a function of the input capacitance by applying a suitable pulse to the test-input of the preamplifier. Noise versus input capacitance curve has been plotted in Fig. 3(a). The preamplifier shows 2.5 keV noise at zero input capacitance. The variation of the preamplifier noise with input capacitance is seen to be 0.10 keV per pF for 1 μ sec shaping time-constant in the main active-filter amplifier that follows the preamplifier. The signal-to-noise ratio is found to be the highest with 1 μ sec time-constant. It is found to be less than this maximum for lower and higher values. The linearity of the preamplifier system has been tested with the input pulse from a precision pulse generator. The output from the amplifier is measured with an oscilloscope. A good linearity is observed for the system [Fig. 3(b)].

Performance of the preamplifier has been tested by using it with an ORTEC silicon surface-barrier

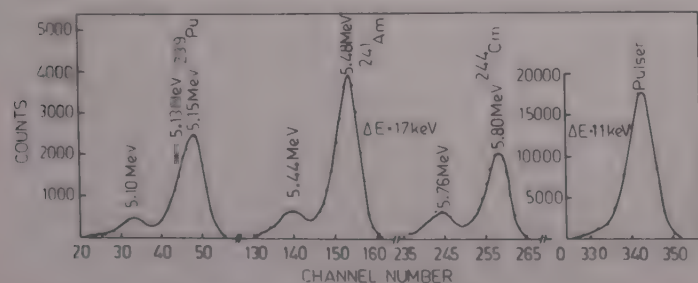


Fig. 2—Alpha spectrum of ORTEC SB-detector using the preamplifier [The pulser peak is at the extreme right]

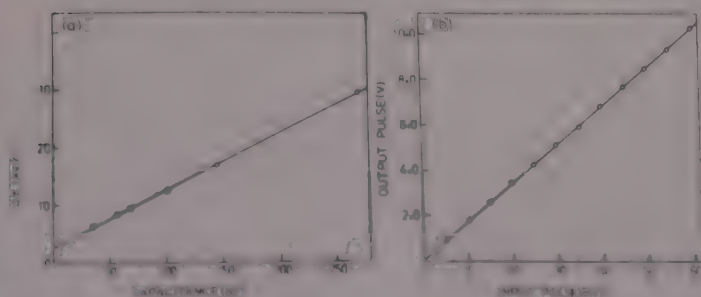


Fig. 3—(a). Variation of resolution with input capacitance and (b) system linearity curve

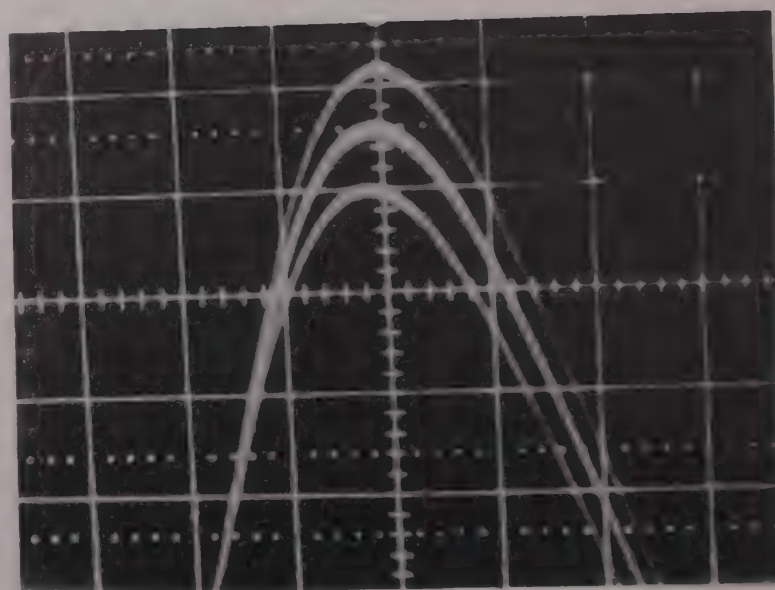
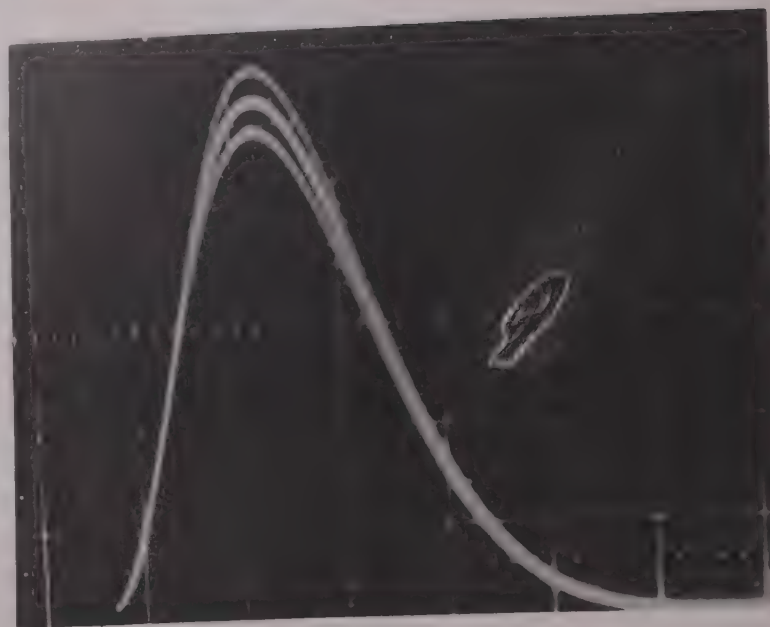


Fig. 4—Oscillograms of output pulses [(a), Direct (horizontal: 1 μ s/cm, vertical: 1 V/cm), (b), Through biased amplifier (horizontal: 0.5 μ s/cm, vertical: 0.5 V/cm)]

detector (model BA-10-1000, Ser. No. 14-892D). This detector was operated at room temperature under 100 V bias in a vacuum of 10^{-3} torr. The detector operated in conjunction with this preamplifier and an active-filter amplifier gives excellent performance. The output pulses, corresponding to the alpha-groups of a mixed source (AMR 33 from Radio Chemical Centre, Amersham, UK) containing ^{239}Pu , ^{241}Am , ^{244}Cm from this assembly, are seen direct and through a biased amplifier after being carried through a 100 m cable and these are shown in the enlarged oscillogram of Figs 4(a) and (b). The three distinct groups of pulses correspond to the three major alpha groups present in the mixed source.

The output pulses from the detector assembly are fed to the multichannel analyzer. To measure the electronic system noise, test pulses from the pulser are also simultaneously fed to the test input of the preamplifier. The alpha spectrum recorded is shown in

Fig. 2. The energy resolution of 17 keV has been achieved for ^{241}Am alphas for the room temperature operation of the surface-barrier detector under a vacuum of 10^{-3} torr. The total electronic system noise contribution has been observed to be 11 keV under this condition.

The preamplifier designed with the indigenous components has shown excellent performance for the silicon surface-barrier detectors. The optimization in the size of the preamplifier assembly ($6\text{ cm} \times 4\text{ cm} \times 1.2\text{ cm}$) has made it possible to use these preamplifiers inside the scattering chamber, which is necessary for high-resolution, charged-particle spectroscopy.

The authors wish to express their gratitude to the Director of the Institute and Prof. B B Baliga for their interest. They are also grateful to Shri M K Karmokar for his help in the experiments.

References

- 1 Blalock T V, *IEEE Trans Nucl Sci (USA)*, **13** (1966) 457
- 2 Smith K F & Clive J E, *IEEE Trans Nucl Sci (USA)*, **13** (1966) 469
- 3 Radeka V, *IEEE Trans Nucl Sci (USA)*, **20** (1973) 182.
- 4 Goulding F S, *Nucleonics (USA)*, **22** (1964) 54.
- 5 Goulding F S, Walton J & Malone D F, *Nucl Instrum & Methods (Netherlands)*, **71** (1969) 273.
- 6 Young D C & Hardie D, *Nucl Instrum & Methods (Netherlands)*, **100** (1972) 553.

Electron-Electron Interaction in the X-ray Emission Spectra of Rare-Earth Elements & Their Oxides

K S SRIVASTAVA*, A K SRIVASTAVA, KIRTI SINHA
M HUSAIN & SHIV SINGH†

Theoretical Physics Division, Physics Department, University of
Lucknow, Lucknow 226 007

Received 28 July 1982; revised received 31 December 1982

A possible explanation for the origin of $L\gamma'_1$ satellites of $L\gamma_1$ X-ray emission lines of rare-earth elements ($59 \leq Z \leq 69$) and their oxides is given. The satellite-parent energy separations and the relative intensities of the satellites have been calculated using the theory of plasmon oscillations in solids. Our calculated results are in good agreement with the experimental values of S I Salem and B L Scott [*Phys Rev A (USA)*, 9 (1974) 690].

Recently X-ray emission satellite lines at the low energy side of $L\gamma_1$ ($L_2 \rightarrow N_4$) were observed by Salem and Scott¹ in the elements $59 \leq Z \leq 69$ and their oxides. According to them¹, the structure $L\gamma'_1$ arises because of the exchange interaction between the $4f$ and $4d$ electrons, which splits both the levels. The transition from the splitted levels gives rise to the $L\gamma'_1$ structure. They have calculated the energy separations and relative intensities of the $L\gamma'_1$ structure with respect to the main $L\gamma_1$ peak with the help of the exchange interaction theory². But their calculated values are far from their own experimentally observed values. Moreover, on the basis of exchange interaction theory they could not calculate the energy separation ΔE and the relative intensity i for oxides of above mentioned elements. Therefore, it was thought of great interest to explain the origin of the low energy $L\gamma'_1$ X-ray satellite on the basis of some other alternative theory like that of plasmon oscillations in solids.

The authors³ have recently used the theory of plasmon oscillations in solids to explain the low energy $K\beta'$ satellites of transition elements and their oxides. The same theory is being extended here to explain the low energy $L\gamma'_1$ X-ray satellites of rare-earth elements and their oxides. Using the theory of plasmon oscillations in solids, we have calculated the satellite-parent energy separations and the relative intensities for rare-earth elements and their oxides. A good agreement between the experimentally observed values of Salem and Scott¹ and our calculated values has been obtained as compared to their calculated values on the

basis of exchange interaction theory. This permits us to assign the low energy $L\gamma'_1$ satellite line in the rare-earth elements ($59 \leq Z \leq 69$) and their oxides as due to excitation of plasma oscillations during X-ray emission process.

Plasmon theory—In the X-ray emission process, the initial state consists of a core vacancy which is subsequently filled up by an outer electron with the emission of an X-ray photon. If the valence electron, before filling the core vacancy, excites a plasmon in the valence band, the energy $\hbar\omega_p$ needed for the excitation of these collective modes of oscillations is taken from the transiting valence electron. Hence the emitted radiation quanta will be deprived of an energy $\hbar\omega_p$ giving rise to a low energy plasmon satellite whose energy separation from the main diagram X-ray line will be $\hbar\omega_p$, which is given by³

$$\hbar\omega_p = 28.8 \left(\frac{Z'\sigma}{W} \right)^{1/2} \quad (\text{eV}) \quad \dots (1)$$

where Z' is the effective number of free electrons taking part in plasma oscillations, σ is the specific gravity and W is the molecular weight.

Results and discussion—Eq. (1) is valid for the free electron model but to a fairly good approximation it can also be used for semiconductors and insulators³. Tsutsumi *et al.*⁴ have recently shown that it is the number of unpaired electrons in the valence band that determines the emission process of low energy X-ray satellites. Thus, taking account of the overlapping⁵ of energy levels, the effective number of free electrons Z'

Table 1—Plasmon Energy of Rare-Earth Elements & Their Oxides

Element/ compound	Z'	σ	W	$\hbar\omega_p$ eV	r_s
⁵⁹ Pr	13	6.78	140.92	22.78	1.6234
⁶⁰ Nd	12	7.00	144.27	21.98	1.6626
⁶² Sm	10	7.54	150.35	20.40	1.7474
⁶³ Eu	9	5.25	152.00	16.06	2.0494
⁶⁴ Gd	10	7.89	157.26	20.40	1.7471
⁶⁵ Tb	9	8.27	158.93	19.71	1.7878
⁶⁶ Dy	8	8.53	162.51	18.66	1.8539
⁶⁷ Ho	5	8.80	164.94	14.88	2.1566
⁶⁸ Er	4	9.04	167.20	13.39	2.3129
⁶⁹ Tm	3	9.32	168.94	11.72	2.5286
Pr ₂ O ₃	32	6.88	329.84	23.53	1.5886
Nd ₂ O ₃	30	7.24	336.54	23.14	1.6065
Sm ₂ O ₃	26	7.43	348.86	21.43	1.6906
Eu ₂ O ₃	24	7.42	352.00	20.48	1.7423
Gd ₂ O ₃	26	7.407	361.80	21.01	1.7130
Dy ₂ O ₃	22	7.81	372.92	19.55	1.7975
Er ₂ O ₃	14	8.64	382.40	16.40	2.0375

*On leave from Physics Department, Hindu College, Moradabad 244 001

Table 2—Energy Separation ΔE of the $L\gamma'_1$ Satellite of Rare-Earth Elements & Their Oxides

Element/ compound	$\hbar\omega_p$ eV	Salem & Scott's values for ΔE	
		Obs eV	Calc eV
Pr	22.78	25.5 ± 2.4	8.2
Nd	21.98	23.2 ± 0.7	10.7
Sm	20.40	19.2 ± 3.0	16.1
Eu	16.06	21.5 ± 0.3	18.9
Gd	20.40	23.7 ± 0.6	20.2
Tb	19.71	21.0 ± 0.8	15.6
Dy	18.66	18.4 ± 0.1	12.9
Ho	14.88	16.1 ± 0.3	10.5
Er	13.39	12.8 ± 4.8	8.1
Tm	11.72	13.3 ± 0.9	5.5
Pr ₂ O ₃	23.53	24.3 ± 2.7	—
Nd ₂ O ₃	21.43	20.1 ± 0.3	—
Sm ₂ O ₃	21.43	21.5	—
Eu ₂ O ₃	20.48	21.8	—
Gd ₂ O ₃	21.01	21.5 ± 0.4	—
Dy ₂ O ₃	19.55	17.4 ± 0.6	—
Er ₂ O ₃	16.20	18.9 ± 2.0	—

Table 3—Relative Intensity (i) of the $L\gamma'_1$ Satellite of Lanthanides & Their Oxides

Element compound	Present calculated i values	Salem & Scott's values for i	
		Obs.	Calc.
Pr	0.24	0.15 ± 0.10	0.60
Nd	0.25	0.33 ± 0.07	0.67
Sm	0.26	0.35 ± 0.05	0.75
Eu	0.31	0.36 ± 0.01	0.78
Gd	0.26	0.30 ± 0.04	0.78
Tb	0.27	0.36 ± 0.07	0.71
Dy	0.28	0.36 ± 0.01	0.67
Ho	0.33	0.26 ± 0.03	0.60
Er	0.35	0.10 ± 0.02	0.50
Tm	0.38	0.05 ± 0.01	0.33
Pr ₂ O ₃	0.23	0.09 ± 0.03	—
Nd ₂ O ₃	0.24	0.19 ± 0.05	—
Sm ₂ O ₃	0.25	0.48	—
Eu ₂ O ₃	0.26	0.59	—
Gd ₂ O ₃	0.25	0.55 ± 0.03	—
Dy ₂ O ₃	0.27	0.56 ± 0.03	—
Er ₂ O ₃	0.31	0.16 ± 0.02	—

for Pr, Nd, Pm, Sm, Eu, Gd, Tb, Dy, Ho, Er and Tm comes out to be 13, 12, 11, 10, 9, 10, 9, 8, 5, 4 and 3 respectively (Table 1). In the case of oxygen, the number of unpaired electrons is two⁶. Thus for lanthanide oxides (R_2O_3), the value of Z' would be 32, 30, 28, 26, 24, 26, 24, 22, 16, 14 and 12 respectively (Table 1).

Taking the values of Z' , σ and W from Table 1 and using Eq. (1), the values of plasmon energy ($\hbar\omega_p$) have been calculated. They are found to be fairly close to the experimentally observed values of Salem and Scott¹ for the energy separation ΔE between the $L\gamma_1$ emission line and the $L\gamma'_1$ satellite (Table 2).

In order to confirm the plasmon hypothesis, we have calculated the relative intensity of the $L\gamma'_1$ satellite with respect to the $L\gamma_1$ line. Srivastava *et al.*³ have used the following expression for the relative intensity of plasmon satellites:

$$i = \frac{I_1}{I_0} = \alpha' = 0.16 r_s - 0.02 \quad \dots (2)$$

where r_s is a dimensionless parameter given by⁷

$$r_s = \left(\frac{47.11}{\hbar\omega_p} \right)^{2/3} \quad \dots (3)$$

We have calculated the values of i for rare-earth elements and their oxides which are given in Table 3. The results have also been compared with the experimental and calculated values of Salem and Scott¹. From Table 3, it can be seen that the relative intensities observed by Salem and Scott¹ of the $L\gamma'_1$ satellites are in better agreement with the calculated values of the authors than those calculated on the basis of exchange interaction theory of Salem and Scott¹.

Thanks are due to the CSIR, the University Grants Commission, New Delhi, and the UP State Council of Science and Technology, Lucknow, for financial assistances.

References

- 1 Salem S I & Scott B L, *Phys Rev A (USA)*, **9** (1974) 690.
- 2 Tsutsumi K & Nakamori H, *J Phys Soc Jpn (Japan)*, **25** (1968) 1418.
- 3 Srivastava K S, Singh S, Srivastava A K, Nayal R S, Chaubey A & Gupta P, *Phys Rev A (USA)*, **25** (1982) 2838.
- 4 Tsutsumi K, Nakamori H & Ichikawa K, *Phys Rev B (USA)*, **13** (1976) 929.
- 5 Nadler Y & Kittel G, in *Structure of matter*, translated from original Russian by M Karapetyants and S Drakin (Mir Publishers, Moscow), 1974, 82.
- 6 Glasstone S, *Theoretical chemistry* (Affiliated East-West Press Pvt. Ltd., New Delhi) 1973, 97.
- 7 Rooke G A, *Phys Lett (Netherlands)*, **3** (1963) 234.

Electronic & Vibrational Spectra of 2,5-Dimethyl Pyrazine

S L SRIVASTAVA

Department of Physics, University of Gorakhpur, Gorakhpur
273 001

&

ROHITASHAVA*

Department of Physics, D N College, Meerut 250 002
and

A N PANDEY

Department of Physics, Meerut College, Meerut 250 001

Received 3 October 1980; accepted 2 March 1983

Investigations on the electronic and vibrational spectra of 2,5-dimethyl pyrazine are reported. The electronic spectrum of the molecule shows two (one broad and one discrete) absorption systems in the ultraviolet region but the vibrational analysis of only the discrete system was possible. The vibrational spectra of the molecule recorded on Grubb Parsons MK II spectrophotometer in the region 2.5 to 24 μm have been analyzed in terms of fundamentals, their combinations and overtones. The tentative modes of vibration are also discussed.

The electronic spectrum of pyrazine has been studied by many workers¹⁻⁴ with special reference to $n\text{-}\pi^*$ transition. Systematic investigations by Innes and coworkers⁵⁻⁹ have established that the $n\text{-}\pi^*$ transition located around 3200 Å and also having a well resolved structure is due to ${}^1B_{3u} \leftarrow {}^1A_g$, an allowed transition, with the transition moment lying in the plane of the molecule. Further, this system also involves forbidden vibronic bands whose intensities are enhanced by vibronic interaction between the ${}^1B_{3u}$ and ${}^1B_{2u}$ states through the out-of-plane hydrogen bending vibration. As regards the spectra of substituted pyrazines, the electronic spectra of 2-chloro-pyrazine¹⁰ and 2-methyl pyrazine¹¹ have been studied. Simmons *et al.*¹² have also reported the vibrational spectra of some deuterated pyrazines. In the case of 2-methyl pyrazine it has been reported by one of the authors¹¹ that the coupling between ${}^1B_{3u}$ and ${}^1B_{2u}$ states still exists although the symmetry of the molecule has reduced to C_s and the band system appears due to ${}^1A'' \leftarrow {}^1A'$ transition. Hence, it was considered necessary to investigate the spectrum by attaching one more methyl group at position 5 in 2-methyl pyrazine to understand fully the transitions involved together with the possible coupling between ${}^1B_{3u}$ and ${}^1B_{2u}$ states. In addition to this, the infrared absorption spectra have also been obtained for investigating the role of the substituent on the vibrations of pyrazine in the ground state.

Experimental procedure and results—2,5-Dimethyl pyrazine obtained from M/s A G Fluka, Switzerland has been used without further purification. The near ultraviolet absorption spectrum has been photographed on Hilger medium quartz spectrograph in the vapour phase. Two absorption systems have been photographed under two different conditions. The shorter wavelength system appears at room temperature with a path length of 75 cm having small amount of vapours in it, whereas the longer wavelength system has been obtained only at a path length of 150 cm maintained at a temperature of 40°C. In the longer wavelength system, nearly 20 violet degraded bands in the region (2990-3250 Å) have been measured. The bands, in general, are sharp and the accuracy for such bands is up to $\pm 5\text{ cm}^{-1}$ whereas this deteriorates to $\pm 10\text{ cm}^{-1}$ in the case of broad, diffuse and weak bands. The system has been analyzed in terms of two excited state fundamentals 305 and 579 cm^{-1} with the 0,0 band at 31038 cm^{-1} . The position of the bands, their separation from the 0,0 band and their assignments are presented in Table 1. The shorter wavelength system in the region 2600-2800 Å shows two broad absorptions at 2740 and 2669 Å.

The infrared absorption spectra have been recorded on Grubb Parsons MK II spectrophotometer in the region 2.5-24 μm in the liquid state. The order of accuracy is $\pm 10\text{ cm}^{-1}$ up to 2000 cm^{-1} and beyond this it worsens to $\pm 20\text{ cm}^{-1}$. The position of the bands and their assignments are presented in Table 2.

Discussion—In view of the conventional structure of pyrazine, D_{2h} point group has been ascribed by Simmons *et al.*¹² On substituting CH_3 group at 2 and 5 positions around the ring, the symmetry of the molecule reduces to C_s . From the broad nature of the bands of the shorter wavelength system, it has been deciphered that it is due to a $\pi\text{-}\pi^*$ transition analogous to ${}^1A_g \rightarrow {}^1B_{2u}$ transition of pyrazine. In view of the C_s point group it is expected that the 0,0 band of the $n\text{-}\pi$ system will appear strongly, but due to vibronic coupling a perturbation is caused by ${}^1B_{2u}$ state, and the upper state becomes ${}^1A''$ rather than ${}^1A'$ and the transition thus becomes ${}^1A'' \leftarrow {}^1A'$. Due to this, the 0,0 band will not appear strongly. In view of the general pattern this has been assigned at 31038 cm^{-1} , whereas for the $\pi\text{-}\pi$ system the band at 36486 cm^{-1} has been chosen.

The strong band at 31617 cm^{-1} involves an excited state fundamental of 579 cm^{-1} . This vibration has been found to be progression forming. The corresponding ground state frequency could not be observed because

Table 1 Analysis of the $n-\pi$ Transition of 2,5-Dimethyl Pyrazine in the Near Ultraviolet Region

Intensity	Position of the bands cm^{-1}	Separation from the 0,0 band, cm^{-1}	Assignment
m	30914	0-124	0-124
w	30948	0-90	0-90
ms	31038	0,0	0,0 band
ms	31087	0+49	0+49
w	31150	0+112	0+112
mw	31343	0+305	0+305
w	31393	0+355	0+305+49
ms	31493	0+455	0+579-124
m	31529	0+491	0+579-90
vs	31617	0+579	0+579
vs	31668	0+630	0+579+49
md	31733	0+695	0+579+112
w	31922	0+885	0+305+579
w	31973	0+935	0+305+579+49
md	32077	0+1039	0+2 \times 579-124
md	32108	0+1070	0+2 \times 579-90
vs	32198	0+1160	0+2 \times 579
vs	32246	0+1208	0+2 \times 579+49
w	32312	0+1274	0+2 \times 579+112
mb	32778	0+1740	0+3 \times 579
mb	32828	0+1790	0+3 \times 579+49
wb	33358	0+2320	0+4 \times 579
wb	33410	0+2372	0+4 \times 579+49

vs, very strong; ms = medium strong; m, medium; mb, medium broad; w, weak and wb, weak and broad

the absorption system contains only limited number of bands towards the longer wavelength. In view of the role of the progressions of this vibration in constituting the overall pattern of the system, along with the data available for pyrazine h_4 and pyrazine d_4 by Suzuka *et al.*¹³, this vibration has been assigned as the $\nu_{6a'}$ mode of pyrazine.

The medium weak band 31343 cm^{-1} involves an excited state fundamental of magnitude 305 cm^{-1} . The progressions of this vibration could not be traced. Its combination only with 579 mode has been observed. Combinations of the type $2 \times 579 + 305$ or $3 \times 579 + 305$ could not be observed because of their weak intensity. The appearance of the fundamental 305 cm^{-1} suggests that the situation in the present case is not different from that observed in 2-methyl pyrazine¹¹. Due to this it can be said that the absence of the integral multiples of 305 cm^{-1} might be due to the fact that the overtones of this fundamental are not the exact integral multiples. This, therefore, gives a reasonable possibility of a large anharmonicity of the potential of the excited state. Further, with respect to the 0,0 band of pyrazine at 30875 cm^{-1} the present system shows a blue shift of 163 cm^{-1} which is not large in magnitude. In view of this small shift, it has been inferred that the substitution of both the methyl

Table 2 Vibrational Spectra of 2,5-Dimethyl Pyrazine and Its Correlation with Pyrazine d_4 and Pyrazine h_4 (all values are in cm^{-1})

Position of the bands in pyrazine d_4 (Ref. 12)	Position of the bands in pyrazine h_4 (Ref. 12)	Position of the bands in 2,5-dimethyl pyrazine†	Assignment
399	416	430(vw)	ν_{16b}
—	—	440(vw)	—
—	—	450(w)	—
—	516	515(wb)	ν_{6b}
586	596	555(wb)	ν_{6a}
—	—	575(vw)	—
—	—	585(vw)	—
—	—	610(vw)	—
678	703	705(wb)	ν_4
—	757	760(s)	$\gamma(\text{C—H})$
—	950	925(s)	$\gamma(\text{C—H})$
882	1015	1010(s)	$\nu_1(\text{ring})$
840	1110	1100(vs)	ν_{12}
1005	1230	1245(vs)	$\beta(\text{C—H})$
—	—	1335(sh)	$\beta(\text{C—H})$
—	—	1360(ms)	sym. CH_3 bending
—	—	1450(vs)	asym. CH_3 bending
1175	1418	1490(vs)	ν_{19b}
1370	1484	1535(vs)	ν_{19a}
1370	1524	1550(vs)	ν_{8b}
1536	1578	1615(sh)	ν_{11a}
		2055(m)	555 + 1490
		2295(w)	925 + 1360
		2350(w)	1245 + 1100
		2440(w)	1100 + 1335
		2485(w)	2 \times 1245
		2660(w)	1100 + 1550
		2850(vs)	1245 + 1615
		2875(vs)	sym. CH_3 stretching
		2915(sh)	asym. (CH_3 stretching
		2985(sh)	1360 + 1615
		3060(sh)	(C—H) stretching
		3295(vs)	2875 + 430
		3790(w)	2875 + 925
		3915(vw)	2915 + 1010
		4170(mb)	1100 + 3060

† Terms under this column represent the estimated intensities

β = in-plane bending, γ = out-of-plane bending, s = strong, vs = very strong, w = weak, ms = medium strong, wb = weak and broad and vw = very weak

groups does not exert much influence on the upper excited state. It has been pointed out earlier that in the electronic spectrum of pyrazine the presence of the $\nu_{10a}(h_{1q})$ mode shows the presence of strong vibronic coupling between $^1B_{3u}$ and $^1B_{2u}$ states. In the present case it appears that the coupling still exists. The 305 cm^{-1} mode in all probability represents the $\nu_{10a}(h_{1q})$ nontotally symmetric mode of pyrazine.

In the electronic spectrum, no band towards the longer wavelength side could be located, which corresponds to ν''_{6a} mode, under the best experimental conditions. However, a weak infrared band at 555 cm^{-1} has been assigned to ν''_{6a} mode. This selection is in accordance to the 550 cm^{-1} weak infrared band of 2-methyl pyrazine. The ν'_{6a} and ν''_{6a} modes are assigned at 579 and 555 cm^{-1} respectively. It is remarkable that $\nu'_{6a} > \nu''_{6a}$. Further it is clear from the spectrum that 0,0 band is not intense. It is, therefore, obvious that the geometry in both the states is not the same.

In the π - π system there are two broad bands. The approximate centres of gravity of the two bands have been located at 2740 and 2669 Å respectively. Out of the two, the first band has been chosen as the 0,0 band at 2740 Å (36486 cm^{-1}). The second band at 2669 Å (37456 cm^{-1}) has been found to involve an excited state fundamental 970 cm^{-1} . This has been assigned as ν'_1 stretching mode vibration.

The appearance of the strong and diffuse absorption in the π - π transition at $0,0 + 970\text{ cm}^{-1}$ necessitates to investigate the ring ν_1 mode in the ground state. On the basis of the data available for 2-methyl pyrazine, this vibration has been assigned at 1010 cm^{-1} in the infrared spectrum which is the same as that observed at 1015 cm^{-1} in pyrazine. Besides the ν_1 vibration, there are other ring vibrations also (Table 2) which do not show any appreciable change. This observation shows that the two methyl groups do not exert any dominant influence on the vibrational frequencies of pyrazine in the ground state. Other vibrations like C—H vibrations and vibrations associated with the CH_3 group are assigned in the infrared spectrum on the basis of the data available in the literature.

The gross structure of the pattern is explained at the cost of only two excited state fundamentals (305 and

579 cm^{-1}). In the spectrum we have two difference frequencies 90 and 124 cm^{-1} . The exact origin of these frequencies could not be located due to two reasons; first, we have only two excited state vibrations and secondly, we have no information about the fundamental vibrations below 400 cm^{-1} . However, with the help of one IR band at 430 cm^{-1} , the 124 cm^{-1} can be explained as $0 + 305 - 430$.

The authors are thankful to Prof Nitish K Sanyal, Head, Department of Physics, Gorakhpur University, Gorakhpur for providing necessary experimental facilities. Two of the authors (R and A N P) are thankful to the University Grants Commission, New Delhi for financial assistance.

References

- 1 Narva D L & McClure D S, *Chem Phys (Netherlands)*, **11** (1975) 151.
- 2 Zalewski E F, McClure D S & Narva D L, *J Chem Phys (USA)*, **61** (1974) 2964.
- 3 Moomaw W R, Decamp M R & Podove P C, *Chem Phys Lett (Netherlands)*, **14** (1972) 255.
- 4 Califano S, Adembri G & Sbrana G, *Spectrochim Acta (GB)*, **20** (1964) 385.
- 5 Thakur S N & Innes K K, *J Mol Spectrosc (USA)*, **52** (1974) 130.
- 6 Innes K K, Merritt J A, Tincher W C & Tilford S G, *Nature (GB)*, **187** (1960) 500.
- 7 Innes K K, Simmons J D & Tilford S G, *J Mol Spectrosc (USA)*, **11** (1963) 257.
- 8 Innes K K & Parkin J E, *J Mol Spectrosc (USA)*, **21** (1966) 66.
- 9 Innes K K, Byrne J P & Rose I G, *J Mol Spectrosc (USA)*, **22** (1967) 125.
- 10 Upadhy P C, Rai D K, Upadhy K N & Mishra P C, *Indian J Phys*, **46** (1972) 306.
- 11 Sanyal N K, Srivastava S L, Devi Ananda & Nath T, *J Mol Spectrosc (USA)*, **78** (1979) 335.
- 12 Simmons J D, Innes K K & Begun G M, *J Mol Spectrosc (USA)*, **14** (1964) 190.
- 13 Suzuka I, Mikami N & Ito M, *J Mol Spectrosc (USA)*, **52** (1974) 21.

INSTRUCTIONS TO AUTHORS

SCOPE

The journal welcomes, for publication, full papers and short notes, reporting significant new results of research, in all areas of physics except space physics. The applied fields covered are electronics, electrical engineering, instrumentation and applied mathematics. However, papers in applied mathematics with emphasis on only derivation and proofs and having no direct physical significance, will not be considered. Review articles are not published normally.

SUBMISSION OF MANUSCRIPT

Manuscripts for consideration should be submitted, *in duplicate*, to Editor, Indian Journal of Pure & Applied Physics, Publications & Information Directorate, Hillside Road, New Delhi 110012. They should neither have been already published nor be under consideration elsewhere.

Manuscripts should be in English and typewritten on only one side of good quality paper, in double space, with adequate margin on all four sides. One original and one carbon or photo-copy, each complete in all respects including abstract, illustrations, appendixes, etc. are to be submitted.

PREPARATION OF MANUSCRIPT

Authors may consult recent issues of the Journal to familiarize themselves with the general style and practices adopted in regard to the various elements of a paper.

General

Manuscript should be presented in as concise a form as possible. Good attention should be given to spelling and grammar. In giving names of chemical compounds and structures, abbreviations of units of measurements, symbols and notations, the style and practices recommended by the IUPAP and IUPAC, should be followed.

Frequently repeating combinations of words, e.g. electric field gradient (EFG), junction field effect transistor (JFET), stimulated Raman emission (SRE), should be abbreviated subsequently, indicating the abbreviated form in parenthesis, as shown, at the place of their first occurrence.

Pages should be numbered consecutively and arranged in the following order: Title, authors' names with their institutional affiliations and abstract, along with relevant footnotes whenever necessary (on a separate sheet); introduction; experimental details/theory/method/analysis; results; discussion; conclusion(s); acknowledgement; references and appendixes. Tables, captions for figures (with legends) and appendixes should be typed *on separate sheets* and attached at the end of the manuscript.

Title

The title should be neither too brief/general nor unnecessarily long. It should reflect the content of the paper so as to derive the maximum advantage in indexing. If a paper forms part of a general series, a specific subtitle, indicating the particular aspect of the work covered in the paper, should be provided.

A short running title for the paper, the broad subject heading under which it should be classified in the contents page (authors may consult recent numbers of the journal for this purpose), and the author (indicated by an asterisk on the relevant author's name) and address for correspondence, should also be provided on the title page.

Abstract

The abstract, usually not exceeding 200 words, should indicate the scope and significant content of the paper,

highlighting the principal findings and conclusion. It should be in such a form that abstracting periodicals can use it without modification.

Introduction

Long and elaborate introduction should be avoided. It should be brief and state the exact scope of the study in relation to the present status of knowledge in the field. Literature review should be limited strictly to what is necessary to indicate the essential background and the justification for undertaking the study.

Materials, methods, apparatus, etc.

The sources of materials and their purity, methods of preparation, procedure for measurements and their accuracies, etc. should be clearly stated to enable any other worker to repeat the work if necessary. New methods, techniques, theories, etc. should be described in adequate detail; but if they are well known, a mere literature reference to them will do; differences from standard ones, improvements or innovations should, however, be clearly mentioned.

Results

Only such primary data as are essential for understanding the discussion and main conclusions emerging from the study should be included. All secondary data as are of interest to a specific category of readership *should not be included* in the paper. Such data should be retained by the authors for supply, on request, to any interested research worker. A footnote to this effect may be inserted at the relevant place in the paper.

The results must be presented in a coherent sequence in a unified logical structure, avoiding repetition or confusion. Limitations of the results should be clearly stated.

The same data should not be presented in both tabular and graphic forms. Only such tables and figures as are essential should be included. Simple linear plots that can easily be discussed in the text, should not be included. Infrared, ultraviolet, NMR and other spectra, DTA curves, etc. should be included only if they pertain to new compounds and/or are essential to the discussion; otherwise only significant numerical data should be given in the text or in a table.

Discussion

Long rambling discussion should be avoided. The discussion should deal with the interpretation of results without repeating information already presented under results. It should relate new findings to the known and include logical deductions. A separate section on 'conclusions' can be given only when they are well established and of outstanding significance. Mere observation of qualitative trends of results should be distinguished from firm conclusions. Also, limitations, if any, to the conclusions should be clearly pointed out.

Mathematical portions

Special attention should be given to the mathematical portions of the paper. Equations must be well separated from the text and written clearly with good separation between the successive lines. The usual norms of breaking long mathematical expressions should be adhered to. Equations should be numbered consecutively in Arabic numerals with the number in parenthesis near the right hand margin. Superscripts and subscripts should be clearly indicated in pencil by V and \wedge sign respectively. Capital and small letters,

particularly of the same letter when both occur, as well as letters or symbols likely to be confused one for the other, should be clearly distinguished. Special characters (e.g. Greek, script, vector, tensor, etc.) required must be indicated by marginal notes. Letters and symbols which should appear in bold face must be clearly indicated. To simplify typesetting: (i) long and complicated mathematical expressions which are frequently repeated should be replaced with single letter/symbol, without clashing with the others used in the paper; (ii) the 'exp' form of complex exponential functions should be used; and (iii) to simplify fractions, the solidus (/) is to be used and fractional exponents are to be used instead of root signs, e.g.

write $\exp\{-i\omega_0(t_1 - t_2)/2\}$ and not $e^{-i\omega_0(t_1 - t_2)/2}$

write $(4\omega_{pl} K_{3\lambda}^2/\tilde{\omega} K_D^2)^{1/2}$ and not $\sqrt{\frac{4\omega_{pl} K_{3\lambda}^2}{\tilde{\omega} K_D^2}}$

Tables

Tables should be numbered consecutively in Arabic numerals and should bear brief titles. Column headings should be brief. Units of measurement should be abbreviated and placed below the headings. Nil results should be indicated and distinguished clearly from absence of data. Inclusion of structural formulae inside the tables should be avoided as far as possible. Tables should be referred to in the text by numbers and not by terms like 'above', 'below', 'preceding' or 'following'. Results should not be presented to a greater accuracy than that of the method employed.

Illustrations

The number of illustrations should be kept to the minimum. Wherever possible, e.g. a number of individual analogous figures referring to different variables, substances, molecules, etc. may be combined into one composite figure. All illustrations should be numbered consecutively in Arabic numerals. Captions and legends to the figures should be self-explanatory. Line drawings should be made with Indian ink on white drawing paper/cellophane sheet/tracing cloth, and drawn to approximately twice the printed size.

The lettering should be uniform, preferably in stencil, so as to be not less than 1.5 mm after reduction widthwise to full page size (165 mm) or column size (80 mm). The size of geometrical shapes (used to distinguish different graphs), dots, lines, etc. should be sufficiently large to permit the necessary reduction without loss of detail. In the case of photographs, prints must be on glossy paper and contrasty. If an illustration is taken from another publication, reference to the source should be given and prior permission secured. Illustrations should be referred to in the text by numbers and not by terms like 'above', 'following' etc.

Acknowledgement

Acknowledgements should not be exuberant and must be made only to real assistance rendered in connection with the work reported in the paper.

References

References cited should be limited to the absolute minimum (particularly in the case of short notes) based on their essential relevance. In the text, references to literature should be numbered consecutively, in the order of their first occurrence, and should be indicated by superscript Arabic numbers at the relevant places; as far as possible the placement of references on numerals or other symbols should be avoided; in such cases the reference may be given in parenthesis in running text, e.g. "this yielded for n a value of 2.3 (Ref. 5)". Full bibliographic details for all the references mentioned in the text should be listed in serial order at the end of the paper.

In citing references to research papers, names and initials of authors should be followed, in order, by the title of the periodical in the abbreviated form (underlined), the volume number (two lines underneath), the year within circular brackets and the page number [e.g. Chandra B P & Shrivastava KK, *J Phys & Chem Solids (GB)*, 39 (1978) 939]. For names of periodicals, the abbreviations followed by the *Physics Abstracts* should be used. For periodicals not covered by *Physics Abstracts*, the title abbreviations should be according to the *Bibliographic Guide for Editors and Authors*, 1974, published by the American Chemical Society, Washington DC, USA; additionally the country from which the journal is published should be given in parenthesis immediately after the title abbreviation. If a paper has been accepted for publication, the names of the authors and the journal (with volume number and year, if known) should be given followed by the words "in press" [e.g. Wahi P K & Patel N D, *Can J Spectrosc (Canada)*, in press.].

In references containing up to four authors, the names of all the authors with their respective initials should be given. The abbreviations *et al.*, *idem* and *ibid* should be avoided. When there are more than four authors, only the names of the first three authors with their respective initials should be given, followed by the words 'et al.'

Reference to a book should include details in the following order: name and initials of authors, the title of the book (underlined), name of publisher and place of publication within circular brackets and year and page (s) [e.g. Clayton G B, *Operational amplifiers* (Newnes-Butterworths, London), 4th Edn, 1977, 26]. If the reference is to the work of an author published in a book by a different person, the fact that it is cited from the source book should be clearly indicated [e.g. Turnhout Van J, 'Thermally stimulated discharge of electrets' in *Topics in applied physics: Vol. 33—Electrets*, edited by C M Sessler (Springer Verlag, Berlin), 1980, 130].

Proceedings of conferences and symposia should be treated in the same manner as books. Reference to a paper presented at a conference, the proceedings of which are not published, should include, in the following order, names and initials of authors, title of the paper (underlined), name of the conference, and where and when it was held (e.g. Herczeg P, *Symmetry-violating kaon decays*, paper presented to the International Conference on High Energy Physics and Nuclear Structure, Vancouver, Canada, 13-17 August 1979).

Reference to a thesis should include the name of the author, title of the thesis (underlined), university or institution to which it was submitted and year of submission (e.g. Mehrotra S N, *Many-body techniques and their applications to interacting bosons*, Ph D thesis, Ranchi University, 1976).

Reference to a patent should include names of patentees, country of origin (underlined) and patent number, the organization to which the patent has been assigned (within circular brackets), date of acceptance of the patent and reference to an abstracting periodical where available [e.g. Labes M M, *US Pat.* 4,066,567 (to Temple University), 3 January 1978; *Chem. Abstr.*, 88 (No. 20) (1978), 138350 n].

PROOFS & REPRINTS

Authors will receive galley proofs and a reprint order form. The galley proofs, indicating the essential corrections, should be returned to the Editor without delay, enclosing the reprint order form. Authors are given 25 free reprints for each paper. Extra reprints can be had at cost. If the reprint order is not received with the corrected proofs, it will be presumed that the author needs no extra reprints. Later requests for more reprints cannot be complied with. Covers for reprints cannot be provided.

THE WEALTH OF INDIA

An Encyclopaedia of Indian Raw Materials and Industrial Products, published in two series:

(i) **Raw Materials**, and (ii) **Industrial Products**.

RAW MATERIALS

The articles deal with Animal Products, Dyes & Tans, Essential Oils, Fats & Oils, Fibres & Pulps, Foods & Fodders, Drugs, Minerals, Spices & Flavourings, and Timbers and other Forest products. Names in Indian languages, and trade names are provided.

For important crops, their origin, distribution, evolution of cultivated types, and methods of cultivation, harvesting and storage are mentioned in detail. Data regarding area and yield and import and export are provided. Regarding minerals, their occurrence and distribution in the country and modes of exploitation and utilization are given. The articles are well illustrated. Adequate literature references are provided.

Eleven volumes of the series covering letters A – Z have been published.

Vol. I(A-B) Rs. 80.00; Vol. II (C) Rs. 95.00; Vol. III (D-E) Rs. 40.00; Vol. IV (F-G) Rs. 65.00; Vol. IV: Suppl. Fish & Fisheries Rs. 40.00; Vol. V (H-K) Rs. 75.00; Vol. VI (L-M) Rs. 90.00; Vol. VI: Suppl. Livestock Rs. 60.00; Vol. VII (N-Pc) Rs. 30.00; Vol. VIII (Ph-Re) Rs. 86.00; Vol. IX (Rh-So) Rs. 104.00; Vol. X (Sp-W) Rs. 152.00; Vol. XI (X-Z) Rs. 102.00.

INDUSTRIAL PRODUCTS

Includes articles giving a comprehensive account of various large, medium and small scale industries. Some of the major industries included are: Acids, Carriages, Diesel Engines, Fertilizers, Insecticides & Pesticides, Iron & Steel, Paints & Varnishes, Petroleum Refining, Pharmaceuticals, Plastics, Ship & Boat-building, Rubber, Silk, etc.

The articles include an account of the raw materials and their availability, manufacturing processes, and uses of products, and industrial potentialities. Specifications of raw materials as well as finished products and statistical data regarding production, demand, exports, imports, prices, etc., are provided. The articles are suitably illustrated. References to the sources of information are provided.

Nine volumes of the series covering letters A – Z have been published.

Part I (A-B) Rs. 54.00; Part II (C) Rs. 64.00; Part III (D-E) Rs. 25.00; Part IV (F-H) Rs. 25.00; Part V (I-L) Rs. 30.00; Part VI (M-Pi) Rs. 28.00; Part VII (Pl-Sh) Rs. 60.00; Part VIII (Si-Ti) Rs. 66.00; Part IX (To-Z) Rs. 80.00.

HINDI EDITION: BHARAT KI SAMPADA—PRAKRITIK PADARTH

Vols. I to VI and two supplements of Wealth of India—Raw Materials series in Hindi already published.

Published Volumes:

Vol. I (अ-औ) Rs. 38; Vol. II (क) Rs. 36; Vol. III (ख-न) Rs. 36; Vol. IV (प) Rs. 83; Vol. V (फ-मेरे) Rs. 60; Vol. VI (मेल-रु) Rs. 80.

Supplements:

Fish & Fisheries (Matsya & Matsyaki) Rs. 49; Livestock (Pashudhan aur Kukkut Palan) Rs. 34.

Vols. VII to XI under publication.

Please contact:

Manager (Sales & Advertisement)

PUBLICATIONS & INFORMATION DIRECTORATE, CSIR

Hillside Road, New Delhi 110012

CSIR PUBLICATIONS

WEALTH OF INDIA

An encyclopaedia of the economic products and industrial resources of India issued in two series

RAW MATERIALS SERIES—contains articles on plant, animal and mineral resources

	Rs	\$	£
Vol. I (A-B)	80.00	30.00	13.00
Vol. II (C)	95.00	33.00	17.00
Vol. III (D-E)	105.00	32.00	20.00
Vol. IV (F-G)	65.00	27.00	12.00
Supplement (Fish & Fisheries)	40.00	16.00	7.00
Vol. V (H-K)	75.00	28.00	12.50
Vol. VI (L-M)	90.00	34.00	15.00
Supplement (Livestock)	60.00	18.00	6.00
Vol. VII (N-Pe)	30.00	9.00	3.00
Vol. VIII (Ph-Re)	86.00	32.00	14.00
Vol. IX (Rh-So)	104.00	35.00	19.00
Vol. X (Sp-W)	152.00	65.00	23.00
Vol. XI (X-Z)	102.00	42.00	20.00

INDUSTRIAL PRODUCTS SERIES—deals with major, small-scale and cottage industries

Part I (A-B)	54.00	20.00	9.00
Part II (C)	64.00	24.00	11.00
Part III (D-E)	25.00	7.50	2.50
Part IV (F-H)	25.00	7.50	2.50
Part V (I-L)	30.00	9.00	3.00
Part VI (M-Pi)	28.00	8.00	2.80
Part VII (Pl-Sh)	60.00	18.00	6.00
Part VIII (Si-Ti)	66.00	27.00	10.00
Part IX (To-Z)	80.00	34.00	12.00

BHARAT KI SAMPADA (Hindi Edition of Wealth of India. Raw Materials)

Vol. I (अ-औ)	38.00	16.00	6.50
Vol. II (क)	36.00	15.00	6.00
Vol. III (ख-न)	36.00	15.00	6.00
Vol. IV (प)	83.00	34.00	16.00
Vol. V (फ-मेरे)	60.00	22.00	10.00
Vol. VI (मेल-ह)	80.00	27.00	13.00
Livestock (Kukkut Palan)	34.00	15.00	6.00
Fish & Fisheries (Matsya aur Matsyaki)	49.00	21.00	8.00
A Dictionary of Generic & Specific Names of Plants and Animals Useful to Man with their English and Latin pronunciation in Devanagari.	30.00	11.00	5.00

OTHER PUBLICATIONS

	Rs	\$	£
Proceedings: seminar on primary communications in Science & Technology in India by Sh. R.N. Sharma & S. Seetharama	52.00	17.50	9.00
Flora of Delhi by J.K. Maheshwari	28.00	8.00	2.80
Indian Fossil Pteridophytes by K.R. Surange	23.00	8.00	2.30
Indian Thysanoptera by T.N. Ananthakrishnan	26.00	8.00	2.60
The Millipede Thyropygus by G. Krishnan	12.00	3.50	1.20
Drug Addiction with special reference to India by R.N. Chopra & I.C. Chopra	12.00	3.50	1.20
Glossary of Indian Medicinal Plants by R.N. Chopra & I.C. Chopra	35.00	13.00	6.00
Fluidization & Related Processes	12.00	4.00	1.20
Evolution of Life by M.S. Randhawa, A.K. Dey, Jagjit Singh & Vishnu Mitre	22.50	7.00	2.25
Collected Scientific Papers of Meghnad Saha	30.00	9.00	3.00
Proteaceae by C. Venkata Rao	34.00	11.00	3.40
Pinus by P. Maheshwari & R.N. Konar	30.00	11.00	5.00
Cellulose Research I	3.00	0.90	0.30
Cellulose Research II	6.00	1.75	0.60
Chemical Process Design	9.00	2.50	0.90
Low Temperature Carbonization of Non-coking Coals & Lignites & Briquetting Coal Fines:			
Vol. I	17.50	5.50	1.75
Vol. II	17.50	5.50	1.75
Nucleic Acids	10.00	3.00	1.00
IGY Symposium: Vol. I	9.00	2.50	0.90
IGY Symposium: Vol. II	9.00	2.50	0.90
CNS Drugs	16.50	5.00	1.65
Kinetics of Electrode Processes & Null Points of Metals	2.50	0.75	0.25
Indian Sardines by R.V. Nair	22.00	7.00	2.20
Termite Problems in India	9.00	3.00	0.90
Loranthaceae by B.M. Johri & S.P. Bhatnagar	32.00	11.00	3.20
Abies and Picea by K.A. Chowdhury	14.00	6.00	2.10
Gnetum by P. Maheshwari and Vimla Vasil	20.00	6.00	2.00
Aquatic Angiosperms by K. Subramanyam	20.00	6.00	2.00
Supplement to Glossary of Indian Medicinal Plants by R.N. Chopra, I.C. Chopra & B.S. Varma	18.00	7.00	3.00
Herbaceous Flora of Dehra Dun by C.R. Babu	144.00	60.00	22.00
Diosgenin and Other Steroid Drug Precursors by Y.R. Chadha & Miss L.V. Asolkar	36.00	13.00	6.00
Research & Development Management by Inder Dev	25.00	10.00	—
Rural Development and Technology—A Status Report-cum-Bibliography by P.R. Bose & V.N. Vashist	100.00	38.00	17.00

Packing and Postage extra.

Please contact:

Manager (Sales & Advertisement)

PUBLICATIONS & INFORMATION DIRECTORATE, CSIR
Hillside Road, New Delhi 110012

Printed & Published by D.S. Sastry, Editor, Publications & Information Directorate (PID)
Hillside Road, New Delhi 110012, at PID Photocomposition Unit